STABILIZATION OF AN IMAGE BASED TRACKING SYSTEM

A THESIS SUBMITTED TO
THE GRADUATE SCHOOL OF NATURAL AND APPLIED SCIENCES
OF
MIDDLE EAST TECHNICAL UNIVERSITY

BY

IRMAK ECE ŞENER

IN PARTIAL FULFILLMENT OF THE REQUIREMENTS
FOR
THE DEGREE OF MASTER OF SCIENCE
IN
ELECTRICAL AND ELECTRONICS ENGINEERING

DECEMBER 2015

Approval of thesis:

STABILIZATION OF AN IMAGE BASED TRACKING SYSTEM

submitted by **IRMAK ECE ŞENER** in partial fulfillment of the requirements for the degree of **Master of Science in Electrical and Electronics Engineering Department, Middle East Technical University** by,

Prof. Dr. M. Gülbin Dural Ünver
Dean, Graduate School of **Natural and Applied Sciences** ____________

Prof. Dr. Gönül Turhan Sayan
Head of Department, **Electrical and Electronics Engineering** ____________

Prof. Dr. M. Kemal Leblebicioğlu
Supervisor, **Electrical and Electronics Eng. Dept., METU** ____________

Examining Committee Members:

Prof. Dr. Mustafa Kuzuoğlu
Electrical and Electronics Engineering Dept., METU ____________________

Prof. Dr. M. Kemal Leblebicioğlu
Electrical and Electronics Engineering Dept., METU ____________________

Prof. Dr. Mehmet Önder Efe
Computer Engineering Dept., Hacettepe University ____________________

Assoc. Prof. Dr. Afşar Saranlı
Electrical and Electronics Engineering Dept., METU ____________________

Assoc. Prof. Dr. Umut Orguner
Electrical and Electronics Engineering Dept., METU ____________________

Date: ____________________

I hereby declare that all information in this document has been obtained and presented in accordance with academic rules and ethical conduct. I also declare that, as required by these rules and conduct, I have fully cited and referenced all material and results that are not original to this work.

Name, Last name	: Irmak Ece Şener
Signature	:

ABSTRACT

STABILIZATION OF AN IMAGE BASED TRACKING SYSTEM

Şener, Irmak Ece
M.S., Department of Electrical and Electronics Engineering
Supervisor: Prof. Dr. M. Kemal Leblebicioğlu

June 2015, 104 pages

Vision based tracking systems require high resolution images of the targets. In addition, tracking system will try to hold the tracked objects at the center of field of view of the camera to achieve robust and successful tracking. Such systems are usually placed on a platform which is to be controlled by a gimbal. The main job of the gimbal is to get rid of jitters and/or undesirable vibrations of the image platform. In this thesis, such an image platform together with its gimbal, and its controller will be modeled and simulated. The design of the controller will be done to yield the resultant system with the optimum performance. The study will be concluded with hardware-in-the-loop simulation studies and theoretical performances will be compared with the practical system's performance.

Keywords: Stabilization, Target Tracking System, Gimbal, Image Platform, Disturbance Rejection

ÖZ

GÖRÜNTÜ TABANLI BİR HEDEF TAKİP SİSTEMİNİN KARARLILAŞTIRILMASI

Şener, Irmak Ece
Yüksek Lisans, Elektrik ve Elektronik Mühendisliği Bölümü
Tez Yöneticisi: Prof. Dr. M. Kemal Leblebicioğlu

Aralık 2015, 104 sayfa

Görüntü tabanlı hedef takip sistemleri hedeflerin yüksek çözünülürlüklü görüntülerine ihtiyaç duyarlar. İlaveten, başarılı bir izleme işi yapmanın yolu, hedefleri kameranın görüş açısının merkezinde tutmaktan geçer. Böyle sistemlerde, kameralar genellikle, bir gimbal tarafından kontrol edilen bir platformun üzerine konulur. Gimbalin ana görevi, kameranın konulduğu platformun titreşimlerini ve gereksiz hareketlerinin kamerayı etkilemesini engellemektir. Bu tezde, bu işi yapan bir görüntü platformu, onun gimbali ve kontrolcüsü modellenecek ve benzetimi yapılacaktır. Kontrolcü, elde edilecek sistemin performansının optimum olmasını sağlayacak şekilde tasarlanacaktır. Çalışma, döngüde donanım içeren benzetim çalışmaları ile sonlandırılacak ve teorik performanslar ile pratik sistemin performansı karşılaştırılacaktır.

Anahtar Kelimeler: Kararlılaştırma, Hedef Takip Sistemi, Gimbal, Görüntü Platformu, Bozucu Etken Baskılama

To my family and my friends…

ACKNOWLEDGEMENTS

It is a pleasure for me to express my sincere gratitude to my thesis supervisor Prof. Dr. Kemal Leblebicioğlu for his belief, patience, encouragement and guidance throughout the study.

I would like to thank my company ASELSAN Inc. for supporting this thesis work and providing me the test setups for the scientific purposes.

I am also grateful to my parents, Hülya and Adnan, my sister, Zinya Elif and my brother Muzaffer Tarık for their love, faith and help throughout my life. Moreover, I would like to thank my dear friends, Eda Uz Loğoğlu, Hakan Uysal, and Tuğçe Erkılıç for their endless motivational supports and fellowships.

TABLE OF CONTENTS

LIST OF FIGURES

FIGURES

LIST OF TABLES

TABLES

LIST OF ABBREVIATIONS

LOS : Line of Sight
IMU : Inertial Measurement Unit
COG : Center of Gravity
DOF : Degree of Freedom
FOV : Field of View
3-D : Three Dimensional
KF : Kalman Filter
MIMO : Multi Input Multi Output
SISO : Single Input Single Output
LS : Least Squares
PID : Proportional-Integral-Derivative
SMC : Sliding Mode Control
GM : Gain Margin
PM : Phase Margin
CAD : Computer Aided Design
(e) : Inertial Frame
(m), (n): Intermediate Coordinate Frames Used in Describing the Base Motion
(B) : Coordinate Frame Fixed to the Gimbal Base
(OA) : Coordinate Frame Fixed to the Outer Azimuth Gimbal
(OE) : Coordinate Frame Fixed to the Outer Elevation Gimbal
(IE) : Coordinate Frame Fixed to the Inner Elevation Gimbal
(IA) : Coordinate Frame Fixed to the Inner Azimuth Gimbal

LIST OF SYMBOLS

Parts of these notations are obtained from [3].

$\hat{C}^{(a,b)}$: Transformation matrix from coordinate frame F_b to coordinate frame F_a

$\vec{r}_{P/O}$: Position vector of point P with respect to point O

$\vec{v}_{P/O}$: Velocity of point P with respect to point O

$\vec{a}_{P/O}$: Acceleration of point P with respect to point O

$\vec{w}_{b/a}$: Relative angular velocity of coordinate frame F_b to coordinate frame F_a

$\vec{\alpha}_{b/a}$: Relative angular acceleration of coordinate frame F_b to coordinate frame F_a

$\vec{\alpha}_{b/a}$: Relative angular acceleration of coordinate frame F_b to coordinate frame F_a

$\vec{u}_1{}^{(a/b)}$: First unit vector of coordinate frame F_a represented in coordinate frame F_b

$\vec{u}_2{}^{(a/b)}$: First unit vector of coordinate frame F_a represented in coordinate frame F_b

$\vec{u}_3{}^{(a/b)}$: First unit vector of coordinate frame F_a represented in coordinate frame F_b

m_{OA} : Mass of the outer azimuth gimbal

m_{OE} : Mass of the outer elevation gimbal

m_{IE} : Mass of the inner elevation gimbal

m_{IA} : Mass of the inner azimuth gimbal

$\vec{g}$: Gravity vector

$\vec{F}_{B,OA}$: Force vector applied by base on the outer azimuth gimbal

$\vec{F}_{IA,OA}$: Force vector applied by the inner azimuth gimbal on the outer azimuth gimbal

$\vec{F}_{OE,OA}$: Force vector applied by the outer elevation gimbal on the outer azimuth gimbal

$\vec{F}_{B,OE}$: Force vector applied by base on the outer elevation gimbal

$\vec{F}_{OA,OE}$: Force vector applied by the outer azimuth gimbal on the outer elevation gimbal

$\vec{F}_{IE,OE}$: Force vector applied by the inner elevation gimbal on the outer elevation gimbal

$\vec{F}_{OE,IE}$: Force vector applied by the outer elevation gimbal on the inner elevation gimbal

$\vec{F}_{IA,IE}$: Force vector applied by the inner azimuth gimbal on the inner elevation gimbal

$\vec{F}_{OA,IA}$: Force vector applied by the outer azimuth gimbal on the inner azimuth gimbal

$\vec{F}_{IE,IA}$: Force vector applied by the inner elevation gimbal on the inner azimuth gimbal

J_{OA} : Inertia tensor of the outer azimuth gimbal

J_{OE} : Inertia tensor of the outer elevation gimbal

J_{IE} : Inertia tensor of the inner elevation gimbal

J_{IA} : Inertia tensor of the inner azimuth gimbal

$\vec{M}_{IA,OA}$: Moment applied by the inner azimuth gimbal on the outer azimuth gimbal

$\vec{M}_{B,OA}$: Moment applied by gimbal base on the outer azimuth gimbal

$\vec{M}_{OE,OA}$: Moment applied by the outer elevation gimbal on the outer azimuth gimbal

$\vec{M}_{B,OE}$: Moment applied by gimbal base on the outer elevation gimbal

$\vec{M}_{OA,OE}$: Moment applied by the outer azimuth gimbal on the outer elevation gimbal

$\vec{M}_{IE,OE}$: Moment applied by the inner elevation gimbal on the outer elevation gimbal

$\vec{M}_{OE,IE}$: Moment applied by the outer elevation gimbal on the inner elevation gimbal

$\vec{M}_{IA,IE}$: Moment applied by the inner azimuth gimbal on the inner elevation gimbal

$\vec{M}_{OA,IA}$: Moment applied by the outer azimuth gimbal on the inner azimuth gimbal

$\vec{M}_{IE,IA}$: Moment applied by the inner elevation gimbal on the inner azimuth gimbal

$\vec{D}_{OA}$: Disturbance moments affecting the outer azimuth gimbal (friction etc.)

$\vec{D}_{OE}$: Disturbance moments affecting the outer elevation gimbal (friction etc.)

$\vec{D}_{IE}$: Disturbance moments affecting the inner elevation gimbal (friction etc.)

$\vec{D}_{IA}$: Disturbance moments affecting the inner azimuth gimbal (friction etc.)

$T_{m,B,OA}$: Motor torque applied on the outer azimuth gimbal

$T_{fr,B,OA}$: Friction torque between gimbal base and the outer azimuth gimbal

$T_{m,OA,OE}$: Motor torque applied on the outer elevation gimbal

$T_{fr,OA,OE}$: Friction torque between the outer azimuth and the outer elevation gimbals

$T_{m,OE,IE}$: Motor torque applied on the inner elevation gimbal

$T_{fr,OE,IE}$: Friction torque between the outer elevation and the inner elevation gimbals

$T_{fr,IE,OE}$: Friction torque between the inner elevation and the outer elevation gimbals

$T_{m,IE,IA}$: Motor torque applied on the inner azimuth gimbal

$T_{fr,IE,IA}$: Friction torque between the inner elevation and the inner azimuth gimbals

x_k : Kalman state vector at time k

y_k : Kalman output vector at time k

w_k : Process noise at time k

v_k : Measurement noise at time k

P_k : Covariance matrix of x_k

Q_k : Covariance matrix of w_k

R_k : Covariance matrix of v_k

Ψ : Platform yaw angle

Θ : Platform pitch angle

Φ : Platform roll angle

ψ_1 : The outer azimuth axis angle

θ_1 : The outer elevation axis angle

θ_2 : The outer elevation axis angle

ψ_2 : The outer azimuth axis angle

Φ : Parameter vector of the output-error system identification method

F_f : Friction force

F_c : Coulomb friction force

F_v : Viscous friction force

F_s : Stribeck function of velocity

CHAPTER 1

INTRODUCTION

1.1 Line-of-Sight Stabilization Systems

Stabilized platforms are gaining more and more importance every day for line of sight (LOS) systems, since images with higher resolution have become essential in defense industries, in order to keep tracking of targets far away. These platforms are also used for line of fire systems that must accurately point a device at a distant object [2]. The device to be pointed or controlled is described as the payload. Stabilization refers to stabilizing the angular position of the payload with respect to the inertial frame, i.e., earth, by utilizing a moving platform [3]. Line of sight (LOS) stabilization includes optics, radars, laser beam, etc., while line of fire stabilization considers the position of a pointed weapon [3].

In order not to have blur or jitter on the image of the target tracking system, only very small stabilization errors can be tolerated. To achieve this, the components of the stabilizing platforms such as high-bandwidth inertial measurement units (IMU), actuators avoiding saturation, low friction bearings and gimbals with balanced mass center must be selected carefully. For reducing the cost of high-quality sensors, the performance can be improved by using some algorithms such as Kalman and noise rejecting filters. In this thesis work, a stabilized platform, developed and manufactured by ASELSAN, which requires very accurate stabilization on the orders of micro radians and carrying out target tracking tasks, is investigated. This electro-optic platform produced to be assembled on avionic vehicles, is shown in Figure 1.1

Figure 1.1: CATS: A Stabilized Electro-Optic Platform Developed and Manufactured by ASELSAN [4]

Two control problems are handled in this LOS stabilization platform, are the problem of positioning and the problem of stabilization [3]. The stabilization problem is a regulator problem, whereas the positioning problem is a servo problem. The stabilization problem requires a disturbance rejection algorithm which eliminates disturbances due to vibrations coming from the avionic vehicle, friction of the bearings which provides rotational motion of gimbal axes, unbalanced mass center of the platform, external torques and forces such as drag force of the air.

The bandwidth of the control loop is determined by the bandwidth of the IMU, which is the gyroscope on the CATS system, in the stabilization loop, and the bandwidth of the hardware for the embedded software of control algorithms. Most of the time, the integration time of the sensors specify the bandwidth of the stabilization loop.

1.2 Literature Survey,

“For beam- and weapon-pointing applications, the LOS is the aim-point, whereas, for radars and electro-optical sensors, the LOS is defined by the field-of-view (FOV) of the sensor, where the motion of the target in the FOV is of interest” [5]. Besides the basics of rate loop of LOS stabilizatiıon system, the effect of bandwidth, structural dynamics of the tracking system such as bending and torsional motor interaction, mounting and compliance interaction on LOS stabilization is investigated in [5]. [6] presents strapdown stabilization method on high-resolution imaging systems which is implemented through the linear state space model of the tracking system. The impacts of mass properties of the stabilization platforms on static and dynamical unbalance and methods of balancing the gimbal masses are investigated in [7]. The RMS pointing jitter criterion is presented as an important statistic of any stationary random pointing process which completely characterizes the control performance, and it is evaluated in [8]. Kinematics and dynamics of a double-gimbal control moment gyroscope is presented in [9], which is an inspiration source of the dynamical model of the 4-DOF platform model in this thesis. Stability of a MEMs gyroscope via sliding mode control through a dynamical model is considered in [10], which resembles this thesis work in such a way that sliding mode control will be implemented on the dynamical model of the platform gimbals for the stabilization. Similar to our work, [3] has investigated the modeling and stabilization of a 2-DOF stabilization platform by utilization of linear accelerometers, a Linear Quadratic Regulator and a load torque estimator.

1.3 Objectives and Contributions of Thesis

In this thesis work, a 4-DOF stabilization platform is modeled through dynamic relationships belonging to each gimbal. Different types of system identification procedures are carried out for each gimbal and IMU. The positioning and stabilization problems are handled with sliding mode control. The immunity to disturbances and accuracy of stabilization will be evaluated.

1.4 Publication

Within the scope of this thesis, a conference article [1] was written and has been presented at the 17^{th} of National Conference (TOK'15) of Turkish National Committee of Automatic Control (TOK) on September 10^{th}, 2015 in Denizli.

1.5 Outline of Thesis

In Chapter 2, theoretical background of thesis which will be utilized in the system modeling and simulation, system identification and control loop of the target tracking system, is presented. Mathematical model of the 4-DOF platform and a brief summary of Kalman filtering are explained.

Chapter 3 presents the system identification solution employing the constrained optimization toolbox of MATLAB. Also, the system identification of the fiber-optic gyroscopes which are used in the system with the aim of velocity feedback in the control loop is carried out using ARMAX system identification model.

In Chapter 4, construction of the simulation model in MATLAB Simulink/SimMechanics is explained including the rigid body block models which are imported from SolidWorks CAD model into the MATLAB environment, the 6-DOF Stewart platform model, the Karnopp friction model, the model of actuator and the modeling of sensor noise and delay. The model parameters and transfer functions come from the system identification process in Chapter 3.

In Chapter 5, control and disturbance rejection algorithms are presented. Sliding mode control method is used for the stabilization.

Finally, Chapter 6 summarizes the overall studies of the thesis. Future work beyond the scope of thesis is given.

CHAPTER 2

THEORETICAL BACKGROUND

In this chapter, theoretical background which is to be used in the system modeling, system identification and construction of the control loop of the target tracking system will be presented. In the next section, a mathematical model of the 4-DOF platform which is composed of transformations of coordinate frames and dynamical equations of motion based on Newton-Euler approach is derived. In the second section, the simplification of the mathematical model is carried out in order to construct the position and rate loops of the platform. In the third section, Karnopp friction model is introduced. In the fourth section, Kalman filtering is given as a brief summary, which is to be used to eliminate the errors in the sensor measurement data.

2.1 Mathematical Model of the 4-DOF Gimbal Platform Including Base Disturbances

This model will include 2-DOF gimbal platform with the outer azimuth, the outer elevation, the inner elevation and the inner azimuth gimbals, respectively, and the base motion. The base motion model consists of a yaw-pitch-roll sequence. For the analysis of motion, frame transformations with the following reference frames are used.

(e) : Inertial Frame
(m),(n) : Intermediate coordinate frames used in describing the base motion
(B) : Coordinate frame fixed to the gimbal base

(OA) : Coordinate frame fixed to the outer azimuth gimbal

(OE) : Coordinate frame fixed to the outer elevation gimbal

(IE) : Coordinate frame fixed to the inner elevation gimbal

(IA) : Coordinate frame fixed to the inner azimuth gimbal

Relations between these frames can be shown in Figure 2.1:

$$F_e \xRightarrow[\text{Yaw }(\psi)]{\hat{C}^{(e,m)}} F_m \xRightarrow[\text{Pitch}(\theta)]{\hat{C}^{(m,n)}} F_n \xRightarrow[\text{Roll}(\varphi)]{\hat{C}^{(n,B)}} F_B \xRightarrow[\text{Yaw }(\psi_1)]{\hat{C}^{(B,OA)}} F_{OA} \xRightarrow[\text{Pitch}(\theta_1)]{\hat{C}^{(OA,OE)}} F_{OE} \xRightarrow[\text{Pitch}(\theta_2)]{\hat{C}^{(OE,IE)}} F_{IE} \xRightarrow[\text{Yaw }(\psi_2)]{\hat{C}^{(IE,IA)}} F_{IA}$$

Figure 2.1: Coordinate Frames and Rotational Relations between Frames [3]

Coordinate frame transformations matrices relating these coordinate frames are as follows, theory of which is mentioned in [11]:

$$\hat{C}^{(e,m)} = \begin{bmatrix} \cos(\psi) & -\sin(\psi) & 0 \\ \sin(\psi) & \cos(\psi) & 0 \\ 0 & 0 & 1 \end{bmatrix} = \hat{C}^{(m,e)T} \tag{2.1}$$

$$\hat{C}^{(m,n)} = \begin{bmatrix} \cos(\theta) & 0 & \sin(\theta) \\ 0 & 1 & 0 \\ -\sin(\theta) & 0 & \cos(\theta) \end{bmatrix} = \hat{C}^{(n,m)T} \tag{2.2}$$

$$\hat{C}^{(n,B)} = \begin{bmatrix} 1 & 0 & 0 \\ 0 & \cos(\varphi) & -\sin(\varphi) \\ 0 & \sin(\varphi) & \cos(\theta) \end{bmatrix} = \hat{C}^{(B,n)T} \tag{2.3}$$

$$\hat{C}^{(B,OA)} = \begin{bmatrix} \cos(\psi_1) & -\sin(\psi_1) & 0 \\ \sin(\psi_1) & \cos(\psi_1) & 0 \\ 0 & 0 & 1 \end{bmatrix} = \hat{C}^{(OA,B)T} \tag{2.4}$$

$$\hat{C}^{(OA,OE)} = \begin{bmatrix} \cos(\theta_1) & 0 & \sin(\theta_1) \\ 0 & 1 & 0 \\ -\sin(\theta_1) & 0 & \cos(\theta_1) \end{bmatrix} = \hat{C}^{(OE,OA)T} \tag{2.5}$$

$$\hat{C}^{(OE,IE)} = \begin{bmatrix} \cos(\theta_2) & 0 & \sin(\theta_2) \\ 0 & 1 & 0 \\ -\sin(\theta_2) & 0 & \cos(\theta_2) \end{bmatrix} = \hat{C}^{(IE,OE)T} \tag{2.6}$$

$$\hat{C}^{(IE,IA)} = \begin{bmatrix} \cos(\psi_2) & -\sin(\psi_2) & 0 \\ \sin(\psi_2) & \cos(\psi_2) & 0 \\ 0 & 0 & 1 \end{bmatrix} = \hat{C}^{(IA,IE)T} \tag{2.7}$$

Figure 2.2 shows some unit vectors of these coordinate frames on the gimbal.

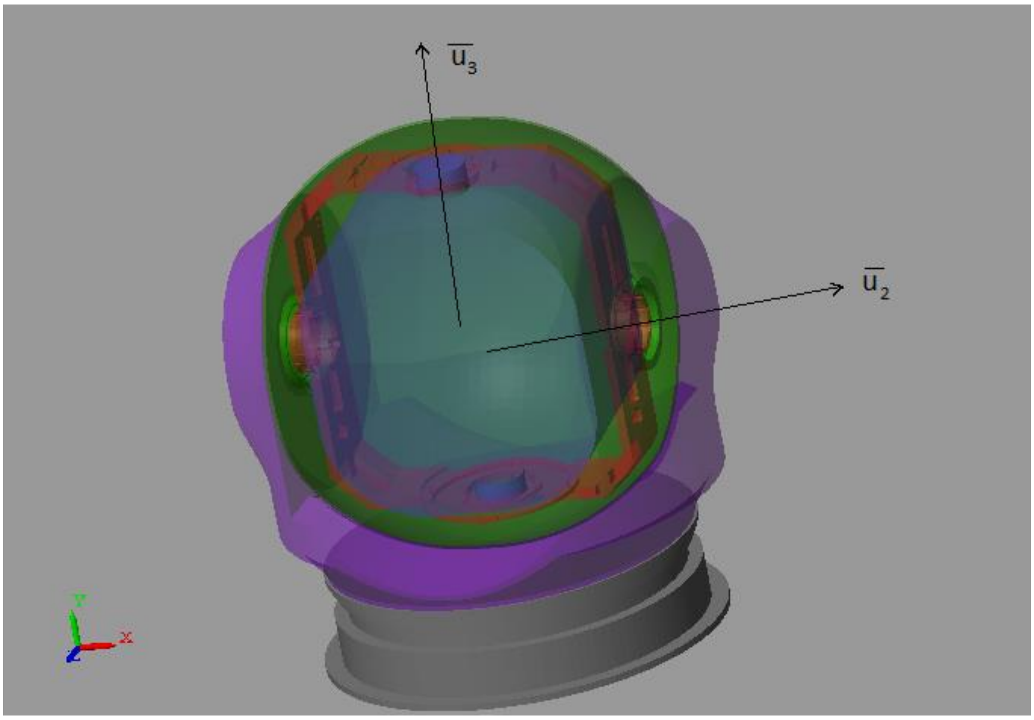

Figure 2.2: Unit Directions on the 4-DOF Gimbal

Newton – Euler equations of motion for each 4 gimbal is derived and frame transformations are applied on the vectors in these equations.

Newton's equation for the outer azimuth gimbal:

$$m_{OA}\vec{a}_{OA} = \vec{F}_{B,OA} + \vec{F}_{IA,OA} + \vec{F}_{OE,OA} + m_{OA}\,\vec{g} \tag{2.8}$$

where;

m_{OA} : mass of the outer azimuth gimbal

$\vec{a}_{OA}$: acceleration of the outer azimuth gimbal (about center of gravity)

$\vec{F}_{B,OA}$: force applied by gimbal base on the outer azimuth gimbal

$\vec{F}_{IA,OA}$: force applied by the inner azimuth gimbal on the outer azimuth gimbal

$\vec{F}_{OE,OA}$: force applied by the outer elevation gimbal on the outer azimuth gimbal

$\vec{g}$: gravity vector

Euler's equation for the outer azimuth gimbal about point "O" which is the intersection of the rotation axes:

$$J_{OA}\vec{\alpha}_{OA} + \vec{w}_{OA} \times J_{OA}\vec{w}_{OA} = \vec{M}_{B,OA} + \vec{M}_{IA,OA} + \vec{M}_{OE,OA} + \vec{r}_{OA} \times (m_{OA}\vec{g}) + \vec{D}_{OA} \qquad (2.9)$$

where;

J_{OA} : inertia of the outer azimuth gimbal

$\vec{\alpha}_{OA}$: angular acceleration of the outer azimuth gimbal

$\vec{w}_{OA}$: angular velocity of the outer azimuth gimbal

$\vec{M}_{IA,OA}$: moment applied by the inner azimuth gimbal on the outer azimuth gimbal

$\vec{M}_{B,OA}$: moment applied by gimbal base on the outer azimuth gimbal

$\vec{M}_{OE,OA}$: moment applied by the outer elevation gimbal on the outer azimuth gimbal

$\vec{r}_{OA}$: the offset between center of gravity and intersection of the rotation axes

$\vec{D}_{OA}$: disturbance moments effecting the outer azimuth gimbal (friction etc.)

Newton's equation for the outer elevation gimbal:

$$m_{OE}\vec{a}_{OE} = \vec{F}_{B,OE} + \vec{F}_{OA,OE} + \vec{F}_{IE,OE} + m_{OE}\,\vec{g} \tag{2.10}$$

where;

m_{OE} : mass of the outer elevation gimbal

$\vec{a}_{OE}$: acceleration of the outer elevation gimbal (about center of gravity)

$\vec{F}_{B,OE}$: force applied by gimbal base on the outer elevation gimbal

$\vec{F}_{OA,OE}$: force applied by the outer azimuth gimbal on the outer elevation gimbal

$\vec{F}_{IE,OE}$: force applied by the inner elevation gimbal on the outer elevation gimbal

$\vec{g}$: gravity vector

Euler's equation for the outer elevation gimbal about point "O" which is the intersection of the rotation axes:

$$J_{OE}\vec{\alpha}_{OE} + \vec{w}_{OE} \times J_{OE}\vec{w}_{OE} = \vec{M}_{B,OE} + \vec{M}_{OA,OE} + \vec{M}_{IE,OE} + \vec{r}_{OE} \times (m_{OE}\vec{g}) + \vec{D}_{OE} \tag{2.11}$$

where;

J_{OE} : inertia tensor of the outer elevation gimbal

$\vec{\alpha}_{OE}$: angular acceleration of the outer elevation gimbal

$\vec{w}_{OE}$: angular velocity of the outer elevation gimbal

$\vec{M}_{B,OE}$: moment applied by gimbal base on the outer elevation gimbal

$\vec{M}_{OA,OE}$:moment applied by the outer azimuth gimbal on the outer elevation gimbal

$\vec{M}_{IE,OE}$:moment applied by the inner elevation gimbal on the outer elevation gimbal

$\vec{r}_{OE}$:the offset between center of gravity and intersection of the rotation axes

$\vec{D}_{OE}$:disturbance moments effecting the outer elevation gimbal (friction etc.)

Newton's equation for the inner elevation gimbal:

$$m_{IE}\vec{a}_{IE} = \vec{F}_{OE,IE} + \vec{F}_{IA,IE} + m_{IE}\,\vec{g} \qquad (2.12)$$

where;

m_{IE} : mass of the inner elevation gimbal

$\vec{a}_{IE}$: acceleration of the inner elevation gimbal (about center of gravity)

$\vec{F}_{OE,IE}$: force applied by the outer elevation gimbal on the inner elevation gimbal

$\vec{F}_{IA,IE}$: force applied by the inner azimuth gimbal on the inner elevation gimbal

$\vec{g}$: gravity vector

Euler's equation for the inner elevation gimbal about point "O" which is the intersection of the rotation axes:

$$J_{IE}\vec{\alpha}_{IE} + \vec{w}_{IE} \times J_{IE}\vec{w}_{IE} = \vec{M}_{OE,IE} + \vec{M}_{IA,IE} + \vec{r}_{IE} \times (m_{IE}\vec{g}) + \vec{D}_{IE} \qquad (2.13)$$

where;

J_{IE} : inertia of the inner elevation gimbal

$\vec{\alpha}_{IE}$: angular acceleration of the inner elevation gimbal

$\vec{w}_{IE}$: angular velocity of the inner elevation gimbal

$\vec{M}_{OE,IE}$: moment applied the outer elevation gimbal on the inner elevation gimbal

$\vec{M}_{IA,IE}$: moment applied the inner azimuth gimbal on the inner elevation gimbal

$\vec{r}_{IE}$: the offset between center of gravity and intersection of the rotation axes

$\vec{D}_{IE}$: disturbance moments effecting the inner elevation gimbal (friction etc.)

Newton’s equation for the inner azimuth gimbal:

$$m_{IA}\vec{a}_{IA} = \vec{F}_{OA,IA} + \vec{F}_{IE,IA} + m_{IA}\vec{g} \tag{2.14}$$

where;

m_{IA} : mass of the inner azimuth gimbal

$\vec{a}_{IA}$: acceleration of the inner azimuth gimbal (about center of gravity)

$\vec{F}_{OA,IA}$: force applied by the outer azimuth gimbal on the inner azimuth gimbal

$\vec{F}_{IE,IA}$: force applied by the inner elevation gimbal on the inner azimuth gimbal

$\vec{g}$: gravity vector

Euler’s equation for the inner azimuth gimbal about point “O” which is the intersection of the rotation axes:

$$J_{IA}\vec{\alpha}_{IA} + \vec{w}_{IA} \text{ x } J_{IA}\vec{w}_{IA} = \vec{M}_{OA,IA} + \vec{M}_{IE,IA} + \vec{r}_{IA} \text{ x } (m_{IA}\vec{g}) + \vec{D}_{IA} \tag{2.15}$$

where;

J_{IA} : inertia of the inner azimuth gimbal

$\vec{\alpha}_{IA}$: angular acceleration of the inner azimuth gimbal

$\vec{w}_{IA}$: angular velocity of the inner azimuth gimbal

$\vec{M}_{OA,IA}$: moment applied by the outer azimuth gimbal on the inner azimuth gimbal

$\vec{M}_{IE,IA}$: moment applied the inner elevation gimbal on the inner azimuth gimbal

$\vec{r}_{IA}$: the offset between center of gravity and intersection of the rotation axes

$\vec{D}_{IA}$: disturbance moments effecting the inner azimuth gimbal (friction etc.)

Due to the fact that linear forces do not create any net torque on none of the 4 gimbals, since they are acting on the center of rotations, we are specifically interested in Euler’s equations.

The angular velocity of the outer azimuth gimbal coordinate frame relative to inertial frame $\vec{w}_{OA/e}$ is represented as:

$$\vec{w}_{OA/e} = \vec{w}_{OA/B} + \vec{w}_{B/n} + \vec{w}_{n/m} + \vec{w}_{m/e} \quad (2.16)$$

$$= \dot{\psi}_1 \vec{u}_3^{(OA/OA)} + \dot{\varphi}\vec{u}_1^{(B/OA)} + \dot{\theta}\vec{u}_2^{(n/OA)} + \dot{\psi}\vec{u}_3^{(m/OA)}$$

$$= \dot{\psi}_1 \vec{u}_3^{(OA/OA)} + \dot{\varphi}\hat{C}^{(OA,B)}\vec{u}_1^{(B/B)} + \dot{\theta}\hat{C}^{(OA,n)}\vec{u}_2^{(n/n)}$$

$$+ \dot{\psi}\hat{C}^{(OA,m)}\vec{u}_3^{(m/m)}$$

$$= \dot{\psi}_1 \vec{u}_3^{(OA/OA)} + \dot{\varphi}\hat{C}^{(OA,B)}\vec{u}_1^{(B/B)}$$

$$+ \dot{\theta}\hat{C}^{(OA,B)}\hat{C}^{(B,n)}\vec{u}_2^{(n/n)}$$

$$+ \dot{\psi}\hat{C}^{(OA,B)}\hat{C}^{(B,n)}\hat{C}^{(n,m)}\vec{u}_3^{(m/m)}$$

where;

$$\hat{C}^{(OA,B)} = \begin{bmatrix} \cos(\psi_1) & \sin(\psi_1) & 0 \\ -\sin(\psi_1) & \cos(\psi_1) & 0 \\ 0 & 0 & 1 \end{bmatrix} = \hat{C}^{(B,OA)T}$$

$$\hat{C}^{(B,n)} = \begin{bmatrix} 1 & 0 & 0 \\ 0 & \cos(\varphi) & \sin(\varphi) \\ 0 & -\sin(\varphi) & \cos(\theta) \end{bmatrix} = \hat{C}^{(n.B)T}$$

$$\hat{C}^{(n,m)} = \begin{bmatrix} \cos(\theta) & 0 & -\sin(\theta) \\ 0 & 1 & 0 \\ \sin(\theta) & 0 & \cos(\theta) \end{bmatrix} = \hat{C}^{(m,n)T}$$

Secondly, the angular velocity of the outer elevation gimbal coordinate frame relative to inertial frame $\vec{w}_{OE/e}$ is represented as:

$$\vec{w}_{OE/e} = \vec{w}_{OE/OA} + \vec{w}_{OA/e} \quad (2.17)$$

$$= \dot{\theta}_1 \vec{u}_3^{(OE/OE)} + \dot{\psi}_1 \hat{C}^{(OE,OA)}\vec{u}_3^{(OA/OE)}$$

$$+ \dot{\varphi}\hat{C}^{(OE,OA)}\vec{u}_1^{(B/OE)} + \dot{\theta}\hat{C}^{(OE,OA)}\vec{u}_2^{(n/OE)}$$

$$+ \dot{\psi}\hat{C}^{(OE,OA)}\vec{u}_3^{(m/OE)}$$

$$=\dot{\theta}_1\vec{u}_3^{\,(OE/OE)} + \dot{\psi}_1\hat{C}^{(OE,OA)}\vec{u}_3^{\,(OA/OA)}$$
$$+\dot{\varphi}\hat{C}^{(OE,OA)}\hat{C}^{(OA,B)}\vec{u}_1^{\,(B/B)}$$
$$+\dot{\theta}\hat{C}^{(OE,OA)}\hat{C}^{(OA,B)}\hat{C}^{(B,n)}\vec{u}_2^{\,(n/n)}$$
$$+\dot{\psi}\hat{C}^{(OE,OA)}\hat{C}^{(OA,B)}\hat{C}^{(B,n)}\hat{C}^{(n,m)}\vec{u}_3^{\,(m/m)}$$

where;

$$\hat{C}^{(OE,OA)} = \begin{bmatrix} \cos(\theta_1) & 0 & -\sin(\theta_1) \\ 0 & 1 & 0 \\ \sin(\theta_1) & 0 & \cos(\theta_1) \end{bmatrix} = \hat{C}^{(OA,OE)T}$$

Thirdly, the angular velocity of the inner elevation gimbal coordinate frame relative to inertial frame $\vec{w}_{IE/e}$ is represented as:

$$\vec{w}_{IE/e} = \vec{w}_{IE/OE} + \vec{w}_{OE/e} \tag{2.18}$$
$$=\dot{\theta}_2\vec{u}_2^{\,(IE/IE)} + \dot{\theta}_1\hat{C}^{(IE,OE)}\vec{u}_3^{\,(OE/IE)}$$
$$+\dot{\psi}_1\hat{C}^{(IE,OE)}\vec{u}_3^{\,(OA/IE)}$$
$$+\dot{\varphi}\hat{C}^{(IE,OE)}\vec{u}_1^{\,(B/IE)} + \dot{\theta}\hat{C}^{(IE,OE)}\vec{u}_2^{\,(n/IE)}$$
$$+\dot{\psi}\hat{C}^{(IE,OE)}\vec{u}_3^{\,(m/IE)}$$
$$=\dot{\theta}_2\vec{u}_2^{\,(IE/IE)} + \dot{\theta}_1\hat{C}^{(IE,OE)}\vec{u}_3^{\,(OE/OE)}$$
$$+\dot{\psi}_1\hat{C}^{(IE,OE)}\hat{C}^{(OE,OA)}\vec{u}_3^{\,(OA/OA)}$$
$$+\dot{\varphi}\hat{C}^{(IE,OE)}\hat{C}^{(OE,OA)}\hat{C}^{(OA,B)}\vec{u}_1^{\,(B/B)}$$
$$+\dot{\theta}\hat{C}^{(IE,OE)}\hat{C}^{(OE,OA)}\hat{C}^{(OA,B)}\hat{C}^{(B,n)}\vec{u}_2^{\,(n/n)}$$
$$+\dot{\psi}\hat{C}^{(IE,OE)}\hat{C}^{(OE,OA)}\hat{C}^{(OA,B)}\hat{C}^{(B,n)}\hat{C}^{(n,m)}\vec{u}_3^{\,(m/m)}$$

where;

$$\hat{C}^{(IE,OE)} = \begin{bmatrix} \cos(\theta_2) & 0 & -\sin(\theta_2) \\ 0 & 1 & 0 \\ \sin(\theta_2) & 0 & \cos(\theta_2) \end{bmatrix} = \hat{C}^{(OE,IE)T}$$

Fourthly, the angular velocity of the inner azimuth gimbal coordinate frame relative to inertial frame $\vec{w}_{IA/e}$ is represented as:

$$
\begin{aligned}
\vec{w}_{IA/e} &= \vec{w}_{IA/IE} + \vec{w}_{IE/e} \qquad (2.19)\\
&= \dot{\psi}_2 \vec{u}_3{}^{(IA/IA)} + \dot{\theta}_2 \hat{C}^{(IA,IE)} \vec{u}_2{}^{(IE/IA)}\\
&+\dot{\theta}_1 \hat{C}^{(IA,IE)} \vec{u}_2{}^{(OE/IA)}\\
&+\dot{\psi}_1 \hat{C}^{(IA,IE)} \vec{u}_3{}^{(OA/IA)} + \dot{\varphi}\, \hat{C}^{(IA,IE)} \vec{u}_1{}^{(B/IA)}\\
&+\dot{\theta}\, \hat{C}^{(IA,IE)} \vec{u}_2{}^{(n/IA)} + \dot{\psi} \hat{C}^{(IA,IE)} \vec{u}_3{}^{(m/IA)}\\
&= \dot{\psi}_2 \vec{u}_3{}^{(IA/IA)} + \dot{\theta}_2 \hat{C}^{(IA,IE)} \vec{u}_2{}^{(IE/IE)}\\
&+\dot{\theta}_1 \hat{C}^{(IA,IE)} \hat{C}^{(IE,OE)} \vec{u}_2{}^{(OE/OE)}\\
&+\dot{\psi}_1 \hat{C}^{(IA,IE)} \hat{C}^{(IE,OE)} \hat{C}^{(OE,OA)} \vec{u}_3{}^{(OA/OA)}\\
&+\dot{\varphi}\, \hat{C}^{(IA,IE)} \hat{C}^{(IE,OE)} \hat{C}^{(OE,OA)} \hat{C}^{(OA,B)} \vec{u}_1{}^{(B/B)}\\
&+\dot{\theta} \hat{C}^{(IA,IE)} \hat{C}^{(IE,OE)} \hat{C}^{(OE,OA)} \hat{C}^{(OA,B)} \hat{C}^{(B,n)} \vec{u}_2{}^{(n/n)}\\
&+\dot{\psi} \hat{C}^{(IA,IE)} \hat{C}^{(IE,OE)} \hat{C}^{(OE,OA)} \hat{C}^{(OA,B)} \hat{C}^{(B,n)} \hat{C}^{(n,m)} \vec{u}_3{}^{(m/m)}
\end{aligned}
$$

where;

$$
\hat{C}^{(IA,IE)} = \begin{bmatrix} \cos(\psi_2) & \sin(\psi_2) & 0 \\ -\sin(\psi_2) & \cos(\psi_2) & 0 \\ 0 & 0 & 1 \end{bmatrix} = \hat{C}^{(IE,IA)T}
$$

Now we can derive the angular acceleration terms belonging to each of the 4 gimbals. The angular acceleration of the outer azimuth gimbal coordinate frame relative to inertial frame $\vec{\alpha}_{OA/e}$ is represented as:

$$
\begin{aligned}
\vec{\alpha}_{OA/e} &= \ddot{\psi}_1 \vec{u}_3 + \ddot{\varphi} \hat{C}^{(OA,B)} \vec{u}_1 + \dot{\varphi} \dot{\hat{C}}^{(OA,B)} \vec{u}_1 \qquad (2.20)\\
&+\ddot{\theta} \hat{C}^{(OA,B)} \hat{C}^{(B,n)} \vec{u}_2 + \dot{\theta} \dot{\hat{C}}^{(OA,B)} \hat{C}^{(B,n)} \vec{u}_2\\
&+\dot{\theta} \hat{C}^{(OA,B)} \dot{\hat{C}}^{(B,n)} \vec{u}_2
\end{aligned}
$$

$$
\begin{aligned}
&+\ddot{\psi}\hat{C}^{(OA,B)}\hat{C}^{(B,n)}\hat{C}^{(n,m)}\vec{u}_3 \\
&+\dot{\psi}\hat{\dot{C}}^{(OA,B)}\hat{C}^{(B,n)}\hat{C}^{(n,m)}\vec{u}_3 \\
&+\dot{\psi}\hat{C}^{(OA,B)}\hat{\dot{C}}^{(B,n)}\hat{C}^{(n,m)}\vec{u}_3 \\
&+\dot{\psi}\hat{C}^{(OA,B)}\hat{C}^{(B,n)}\hat{\dot{C}}^{(n,m)}\vec{u}_3
\end{aligned}
$$

Secondly, the angular acceleration of the outer elevation gimbal coordinate frame relative to inertial frame $\vec{\alpha}_{OE/e}$ is represented as:

$$
\begin{aligned}
\vec{\alpha}_{OE/e} = {} & \ddot{\theta}_1\vec{u}_3+\ddot{\psi}_1\hat{C}^{(OE,OA)}\vec{u}_3 \\
&+\dot{\psi}_1\hat{\ddot{C}}^{(OE,OA)}\vec{u}_3+\ddot{\varphi}\hat{C}^{(OE,OA)}\hat{C}^{(OA,B)}\vec{u}_1 \\
&+\dot{\varphi}\hat{\dot{C}}^{(OE,OA)}\hat{C}^{(OA,B)}\vec{u}_1 + \dot{\varphi}\hat{C}^{(OE,OA)}\hat{\dot{C}}^{(OA,B)}\vec{u}_1 \\
&+\ddot{\theta}\hat{C}^{(OE,OA)}\hat{C}^{(OA,B)}\hat{C}^{(B,n)}\vec{u}_2 \\
&+\dot{\theta}\hat{\dot{C}}^{(OE,OA)}\hat{C}^{(OA,B)}\hat{C}^{(B,n)}\vec{u}_2 \\
&+\dot{\theta}\hat{C}^{(OE,OA)}\hat{\dot{C}}^{(OA,B)}\hat{C}^{(B,n)}\vec{u}_2 \\
&+\dot{\theta}\hat{C}^{(OE,OA)}\hat{C}^{(OA,B)}\hat{\dot{C}}^{(B,n)}\vec{u}_2 \\
&+\ddot{\psi}\hat{C}^{(OE,OA)}\hat{C}^{(OA,B)}\hat{C}^{(B,n)}\hat{C}^{(n,m)}\vec{u}_3 \\
&+\dot{\psi}\hat{\dot{C}}^{(OE,OA)}\hat{C}^{(OA,B)}\hat{C}^{(B,n)}\hat{C}^{(n,m)}\vec{u}_3 \\
&+\dot{\psi}\hat{C}^{(OE,OA)}\hat{\dot{C}}^{(OA,B)}\hat{C}^{(B,n)}\hat{C}^{(n,m)}\vec{u}_3 \\
&+\dot{\psi}\hat{C}^{(OE,OA)}\hat{C}^{(OA,B)}\hat{\dot{C}}^{(B,n)}\hat{C}^{(n,m)}\vec{u}_3 \\
&+\dot{\psi}\hat{C}^{(OE,OA)}\hat{C}^{(OA,B)}\hat{C}^{(B,n)}\hat{\dot{C}}^{(n,m)}\vec{u}_3
\end{aligned}
\tag{2.21}
$$

Thirdly, the angular acceleration of the inner elevation gimbal coordinate frame relative to inertial frame $\vec{\alpha}_{IE/e}$ is represented as:

$$
\begin{aligned}
\vec{\alpha}_{IE/e} = {} & \ddot{\theta}_2\vec{u}_2 +\ddot{\theta}_1\hat{C}^{(IE,OE)}\vec{u}_3+\dot{\theta}_1\hat{\dot{C}}^{(IE,OE)}\vec{u}_3+\ddot{\psi}_1\hat{C}^{(IE,OE)}\hat{C}^{(OE,OA)}\vec{u}_3 \\
&+\dot{\psi}_1\hat{\dot{C}}^{(IE,OE)}\hat{C}^{(OE,OA)}\vec{u}_3 +\dot{\psi}_1\hat{C}^{(IE,OE)}\hat{\dot{C}}^{(OE,OA)}\vec{u}_3 \\
&+\ddot{\varphi}\hat{C}^{(IE,OE)}\hat{C}^{(OE,OA)}\hat{C}^{(OA,B)}\vec{u}_1+\dot{\varphi}\hat{\dot{C}}^{(IE,OE)}\hat{C}^{(OE,OA)}\hat{C}^{(OA,B)}\vec{u}_1 \\
&+\dot{\varphi}\hat{C}^{(IE,OE)}\hat{\dot{C}}^{(OE,OA)}\hat{C}^{(OA,B)}\vec{u}_1
\end{aligned}
\tag{2.22}
$$

$$+\dot{\varphi}\hat{C}^{(IE,OE)}\hat{C}^{(OE,OA)}\dot{\hat{C}}^{(OA,B)}\vec{u}_1$$

$$+\ddot{\theta}\hat{C}^{(IE,OE)}\hat{C}^{(OE,OA)}\hat{C}^{(OA,B)}\hat{C}^{(B,n)}\vec{u}_2+$$

$$+\dot{\theta}\dot{\hat{C}}^{(IE,OE)}\hat{C}^{(OE,OA)}\hat{C}^{(OA,B)}\hat{C}^{(B,n)}\vec{u}_2$$

$$+\dot{\theta}\hat{C}^{(IE,OE)}\dot{\hat{C}}^{(OE,OA)}\hat{C}^{(OA,B)}\hat{C}^{(B,n)}\vec{u}_2$$

$$+\dot{\theta}\hat{C}^{(IE,OE)}\hat{C}^{(OE,OA)}\dot{\hat{C}}^{(OA,B)}\hat{C}^{(B,n)}\vec{u}_2$$

$$+\dot{\theta}\hat{C}^{(IE,OE)}\hat{C}^{(OE,OA)}\hat{C}^{(OA,B)}\dot{\hat{C}}^{(B,n)}\vec{u}_2$$

$$+\ddot{\psi}\hat{C}^{(IE,OE)}\hat{C}^{(OE,OA)}\hat{C}^{(OA,B)}\hat{C}^{(B,n)}\hat{C}^{(n,m)}\vec{u}_3$$

$$+\dot{\psi}\dot{\hat{C}}^{(IE,OE)}\hat{C}^{(OE,OA)}\hat{C}^{(OA,B)}\hat{C}^{(B,n)}\hat{C}^{(n,m)}\vec{u}_3$$

$$+\dot{\psi}\hat{C}^{(IE,OE)}\dot{\hat{C}}^{(OE,OA)}\hat{C}^{(OA,B)}\hat{C}^{(B,n)}\hat{C}^{(n,m)}\vec{u}_3$$

$$+\dot{\psi}\hat{C}^{(IE,OE)}\hat{C}^{(OE,OA)}\dot{\hat{C}}^{(OA,B)}\hat{C}^{(B,n)}\hat{C}^{(n,m)}\vec{u}_3$$

$$+\dot{\psi}\hat{C}^{(IE,OE)}\hat{C}^{(OE,OA)}\hat{C}^{(OA,B)}\dot{\hat{C}}^{(B,n)}\hat{C}^{(n,m)}\vec{u}_3$$

$$+\dot{\psi}\hat{C}^{(IE,OE)}\hat{C}^{(OE,OA)}\hat{C}^{(OA,B)}\hat{C}^{(B,n)}\dot{\hat{C}}^{(n,m)}\vec{u}_3$$

Fourthly, the angular acceleration of the inner azimuth gimbal coordinate frame relative to inertial frame $\vec{\alpha}_{IA/e}$ is represented as

$$\vec{\alpha}_{IA/e} = \ddot{\psi}_2\vec{u}_3+\ddot{\theta}_2\hat{C}^{(IA,IE)}\vec{u}_2+\dot{\theta}_2\dot{\hat{C}}^{(IA,IE)}\vec{u}_2 \tag{2.23}$$

$$+\ddot{\theta}_1\hat{C}^{(IA,IE)}\hat{C}^{(IE,OE)}\vec{u}_2$$

$$+\dot{\theta}_1\dot{\hat{C}}^{(IA,IE)}\hat{C}^{(IE,OE)}\vec{u}_2$$

$$+\dot{\theta}_1\hat{C}^{(IA,IE)}\dot{\hat{C}}^{(IE,OE)}\vec{u}_2$$

$$+\ddot{\psi}_1\hat{C}^{(IA,IE)}\hat{C}^{(IE,OE)}\hat{C}^{(OE,OA)}\vec{u}_3$$

$$+\dot{\psi}_1\dot{\hat{C}}^{(IA,IE)}\hat{C}^{(IE,OE)}\hat{C}^{(OE,OA)}\vec{u}_3$$

$$+\dot{\psi}_1\hat{C}^{(IA,IE)}\dot{\hat{C}}^{(IE,OE)}\hat{C}^{(OE,OA)}\vec{u}_3$$

$$+\dot{\psi}_1\hat{C}^{(IA,IE)}\hat{C}^{(IE,OE)}\dot{\hat{C}}^{(OE,OA)}\vec{u}_3$$

$$+\ddot{\varphi}\,\hat{C}^{(IA,IE)}\hat{C}^{(IE,OE)}\hat{C}^{(OE,OA)}\hat{C}^{(OA,B)}\vec{u}_1$$

$$+\dot{\varphi}\,\dot{\hat{C}}^{(IA,IE)}\hat{C}^{(IE,OE)}\hat{C}^{(OE,OA)}\hat{C}^{(OA,B)}\vec{u}_1$$

$$+\dot{\varphi}\,\hat{C}^{(IA,IE)}\dot{\hat{C}}^{(IE,OE)}\hat{C}^{(OE,OA)}\hat{C}^{(OA,B)}\vec{u}_1$$

$$+\dot{\varphi}\,\hat{C}^{(IA,IE)}\hat{C}^{(IE,OE)}\dot{\hat{C}}^{(OE,OA)}\hat{C}^{(OA,B)}\vec{u}_1$$

$$+\dot{\varphi}\,\hat{C}^{(IA,IE)}\hat{C}^{(IE,OE)}\hat{C}^{(OE,OA)}\dot{\hat{C}}^{(OA,B)}\vec{u}_1$$

$$+\ddot{\theta}\hat{C}^{(IA,IE)}\hat{C}^{(IE,OE)}\hat{C}^{(OE,OA)}\hat{C}^{(OA,B)}\hat{C}^{(B,n)}\vec{u}_2$$

$$+\dot{\theta}\dot{\hat{C}}^{(IA,IE)}\hat{C}^{(IE,OE)}\hat{C}^{(OE,OA)}\hat{C}^{(OA,B)}\hat{C}^{(B,n)}\vec{u}_2$$

$$+\dot{\theta}\hat{C}^{(IA,IE)}\dot{\hat{C}}^{(IE,OE)}\hat{C}^{(OE,OA)}\hat{C}^{(OA,B)}\hat{C}^{(B,n)}\vec{u}_2$$

$$+\dot{\theta}\hat{C}^{(IA,IE)}\hat{C}^{(IE,OE)}\dot{\hat{C}}^{(OE,OA)}\hat{C}^{(OA,B)}\hat{C}^{(B,n)}\vec{u}_2$$

$$+\dot{\theta}\hat{C}^{(IA,IE)}\hat{C}^{(IE,OE)}\hat{C}^{(OE,OA)}\dot{\hat{C}}^{(OA,B)}\hat{C}^{(B,n)}\vec{u}_2$$

$$+\dot{\theta}\hat{C}^{(IA,IE)}\hat{C}^{(IE,OE)}\hat{C}^{(OE,OA)}\hat{C}^{(OA,B)}\dot{\hat{C}}^{(B,n)}\vec{u}_2$$

$$+\ddot{\psi}\hat{C}^{(IA,IE)}\hat{C}^{(IE,OE)}\hat{C}^{(OE,OA)}\hat{C}^{(OA,B)}\hat{C}^{(B,n)}\hat{C}^{(n,m)}\vec{u}_3$$

$$+\dot{\psi}\dot{\hat{C}}^{(IA,IE)}\hat{C}^{(IE,OE)}\hat{C}^{(OE,OA)}\hat{C}^{(OA,B)}\hat{C}^{(B,n)}\hat{C}^{(n,m)}\vec{u}_3$$

$$+\dot{\psi}\hat{C}^{(IA,IE)}\dot{\hat{C}}^{(IE,OE)}\hat{C}^{(OE,OA)}\hat{C}^{(OA,B)}\hat{C}^{(B,n)}\hat{C}^{(n,m)}\vec{u}_3$$

$$+\dot{\psi}\hat{C}^{(IA,IE)}\hat{C}^{(IE,OE)}\dot{\hat{C}}^{(OE,OA)}\hat{C}^{(OA,B)}\hat{C}^{(B,n)}\hat{C}^{(n,m)}\vec{u}_3$$

$$+\dot{\psi}\hat{C}^{(IA,IE)}\hat{C}^{(IE,OE)}\hat{C}^{(OE,OA)}\dot{\hat{C}}^{(OA,B)}\hat{C}^{(B,n)}\hat{C}^{(n,m)}\vec{u}_3$$

$$+\dot{\psi}\hat{C}^{(IA,IE)}\hat{C}^{(IE,OE)}\hat{C}^{(OE,OA)}\hat{C}^{(OA,B)}\dot{\hat{C}}^{(B,n)}\hat{C}^{(n,m)}\vec{u}_3$$

$$+\dot{\psi}\hat{C}^{(IA,IE)}\hat{C}^{(IE,OE)}\hat{C}^{(OE,OA)}\hat{C}^{(OA,B)}\hat{C}^{(B,n)}\dot{\hat{C}}^{(n,m)}\vec{u}_3$$

Gravity vector is defined with respect to inertial coordinate frame as:

$$\{\vec{g}\}^{(e)} = -g\vec{u}_3^{\,(e/e)} = -g\vec{u}_3 \qquad (2.24)$$

In the Newton-Euler equations, we use the transformed version of the gravity vector into the gimbal coordinate frames.

$$\vec{g}^{(OA)} = -g\vec{u}_3^{\,(e/OA)} = -g\hat{C}^{(OA,B)}\hat{C}^{(B,n)}\hat{C}^{(n,m)}\hat{C}^{(m,e)}\vec{u}_3 \qquad (2.25)$$

$$\vec{g}^{(OE)} = \hat{C}^{(OE,OA)}\vec{g}^{(OA)} \qquad (2.26)$$

$$= -g\hat{C}^{(OE,OA)}\hat{C}^{(OA,B)}\hat{C}^{(B,n)}\hat{C}^{(n,m)}\hat{C}^{(m,e)}\vec{u}_3$$

$$\vec{g}^{(IE)} = \hat{C}^{(IE,OE)}\vec{g}^{(OE)} \tag{2.27}$$
$$= -g\hat{C}^{(IE,OE)}\hat{C}^{(OE,OA)}\hat{C}^{(OA,B)}\hat{C}^{(B,n)}\hat{C}^{(n,m)}\hat{C}^{(m,e)}\vec{u}_3$$

$$\vec{g}^{(IA)} = \hat{C}^{(IA,IE)}\vec{g}^{(IE)} \tag{2.28}$$
$$=-g\hat{C}^{(IA,IE)}\hat{C}^{(IE,OE)}\hat{C}^{(OE,OA)}\hat{C}^{(OA,B)}\hat{C}^{(B,n)}\hat{C}^{(n,m)}\hat{C}^{(m,e)}\vec{u}_3$$

Disturbance terms are defined as:

$$\vec{D}_{OA} = D_{OA}\,\vec{u}_3 \tag{2.29}$$

$$\vec{D}_{OE} = D_{OE}\,\vec{u}_2 \tag{2.30}$$

$$\vec{D}_{IE} = D_{IE}\,\vec{u}_2 \tag{2.31}$$

$$\vec{D}_{IA} = D_{IA}\,\vec{u}_3 \tag{2.32}$$

The moment terms are represented as:

$$\vec{M}_{B,OA}{}^{(OA)} = \begin{bmatrix} M_{B,OA,1} \\ M_{B,OA,2} \\ T_{m,B,OA} + T_{fr,B,OA} \end{bmatrix} \tag{2.33}$$

$$\vec{M}_{B,OE}{}^{(OE)} = \begin{bmatrix} M_{B,OE1} \\ T_{m,B,OE} + T_{frB,OE} \\ M_{B,OE,3} \end{bmatrix} \tag{2.34}$$

$$\vec{M}_{OA,OE}{}^{(OE)} = \begin{bmatrix} M_{OA,OE1} \\ T_{m,OA,OE} + T_{fr,OA,OE} \\ M_{OA,OE,3} \end{bmatrix} \tag{2.35}$$

$$\vec{M}_{OE,OA}{}^{(OA)} = \begin{bmatrix} M_{OE,OA,1} \\ M_{OE,OA,2} \\ M_{OE,OA,3} \end{bmatrix} \tag{2.36}$$

$$\vec{M}_{OE,IE}{}^{(IE)} = \begin{bmatrix} M_{OE,IE1} \\ T_{m,OE,IE} + T_{fr,OE,IE} \\ M_{OE,IE,3} \end{bmatrix} \tag{2.37}$$

$$\vec{M}_{IE,OE}{}^{(IE)} = \begin{bmatrix} M_{IE,OE1} \\ T_{m,IE,OE} + T_{fr,IE,OE} \\ M_{IE,OE,3} \end{bmatrix} \tag{2.38}$$

$$\vec{M}_{IE,IA}{}^{(IA)} = \begin{bmatrix} M_{IE,IA,1} \\ M_{IE,IA,2} \\ T_{m,IE,IA} + T_{fr,IE,IA} \end{bmatrix} \tag{2.39}$$

$$\vec{M}_{IA,IE}{}^{(IE)} = \begin{bmatrix} M_{IA,IE,1} \\ M_{IA,IE,2} \\ M_{IA,IE,3} \end{bmatrix} \tag{2.40}$$

$$\vec{M}_{OA,IA}{}^{(IA)} = \begin{bmatrix} M_{OA,IA,1} \\ M_{OA,IA,2} \\ M_{OA,IA,3} \end{bmatrix} \tag{2.41}$$

$$\vec{M}_{IA,OA}{}^{(OA)} = \begin{bmatrix} M_{IA,OA,1} \\ M_{IA,OA,2} \\ M_{IA,OA,3} \end{bmatrix} \tag{2.42}$$

2.2 Simplification of the Mathematical Model

We assume that $\vec{r}_{OA}$, $\vec{r}_{OE,}$ $\vec{r}_{IE}$, $\vec{r}_{IA}$ lengths are zero, meaning that all 4 gimbal centers of rotation and centers of gravity are coincident. We also assume that $\psi(t) = 0, \theta(t) = 0, \varphi(t) = 0,$ meaning that there exists no base disturbance on the 4 gimbals.

$$J_{OA} = \begin{bmatrix} J_{OA1} & 0 & 0 \\ 0 & J_{OA2} & 0 \\ 0 & 0 & J_{OA3} \end{bmatrix} \tag{2.43}$$

$$J_{OE} = \begin{bmatrix} J_{OE1} & 0 & 0 \\ 0 & J_{OE2} & 0 \\ 0 & 0 & J_{OE3} \end{bmatrix} \quad (2.44)$$

$$J_{IE} = \begin{bmatrix} J_{IE1} & 0 & 0 \\ 0 & J_{IE2} & 0 \\ 0 & 0 & J_{IE3} \end{bmatrix} \quad (2.45)$$

$$J_{IA} = \begin{bmatrix} J_{IA1} & 0 & 0 \\ 0 & J_{IA2} & 0 \\ 0 & 0 & J_{IA3} \end{bmatrix} \quad (2.46)$$

$$\vec{D}_{OA} = \begin{bmatrix} 0 \\ 0 \\ D_{OA} \end{bmatrix} \quad (2.47)$$

$$\vec{D}_{OE} = \begin{bmatrix} 0 \\ D_{OE} \\ 0 \end{bmatrix} \quad (2.48)$$

$$\vec{D}_{IE} = \begin{bmatrix} 0 \\ D_{IE} \\ 0 \end{bmatrix} \quad (2.49)$$

$$\vec{D}_{IA} = \begin{bmatrix} 0 \\ 0 \\ D_{IA} \end{bmatrix} \quad (2.50)$$

With these assumptions, the angular velocity and acceleration terms of the 4 gimbals become

$$\vec{w}_{OA/e} = \dot{\psi}_1 \vec{u}_3 \quad (2.51)$$

$$\vec{\alpha}_{OA/e} = \ddot{\psi}_1 \vec{u}_3 \quad (2.52)$$

$$\vec{w}_{OE/e} = \dot{\theta}_1 \vec{u}_3 + \dot{\psi}_1 \hat{C}^{(OE,OA)} \vec{u}_3 \quad (2.53)$$

$$\vec{\alpha}_{OE/e} = \ddot{\theta}_1 \vec{u}_2 + \ddot{\psi}_1 \hat{C}^{(OE,OA)} \vec{u}_3 + \dot{\psi}_1 \hat{\dot{C}}^{(OE,OA)} \vec{u}_3 \quad (2.54)$$

$$\vec{w}_{IE/e} = \dot{\theta}_2 \vec{u}_2 + \dot{\theta}_1 \hat{C}^{(IE,OE)} \vec{u}_3 + \dot{\psi}_1 \hat{C}^{(IE,OE)} \hat{C}^{(OE,OA)} \vec{u}_3 \quad (2.55)$$

$$\vec{\alpha}_{IE/e}= \ddot{\theta}_2\vec{u}_2 + \ddot{\theta}_1\hat{C}^{(IE,OE)}\vec{u}_3+\dot{\theta}_1\hat{\dot{C}}^{(IE,OE)}\vec{u}_3 \tag{2.56}$$
$$+\ddot{\psi}_1\hat{C}^{(IE,OE)}\hat{C}^{(OE,OA)}\vec{u}_3+\dot{\psi}_1\hat{\dot{C}}^{(IE,OE)}\hat{C}^{(OE,OA)}\vec{u}_3$$
$$+\dot{\psi}_1\hat{C}^{(IE,OE)}\hat{\dot{C}}^{(OE,OA)}\vec{u}_3$$

$$\vec{w}_{IA/e} = \dot{\psi}_2\vec{u}_3 + \dot{\theta}_2\hat{C}^{(IA,IE)}\vec{u}_2 + \dot{\theta}_1\hat{C}^{(IA,IE)}\hat{C}^{(IE,OE)}\vec{u}_3 \tag{2.57}$$
$$+\dot{\psi}_1\hat{C}^{(IA,IE)}\hat{C}^{(IE,OE)}\hat{C}^{(OE,OA)}\vec{u}_3$$

$$\vec{\alpha}_{IA/e} = \ddot{\psi}_2\vec{u}_3+\ddot{\theta}_2\hat{C}^{(IA,IE)}\vec{u}_2+\dot{\theta}_2\hat{\dot{C}}^{(IA,IE)}\vec{u}_2 \tag{2.58}$$
$$+\ddot{\theta}_1\hat{C}^{(IA,IE)}\hat{C}^{(IE,OE)}\vec{u}_3+\dot{\theta}_1\hat{\dot{C}}^{(IA,IE)}\hat{C}^{(IE,OE)}\vec{u}_3$$
$$+\dot{\theta}_1\hat{C}^{(IA,IE)}\hat{\dot{C}}^{(IE,OE)}\vec{u}_3$$
$$+\ddot{\psi}_1\hat{C}^{(IA,IE)}\hat{C}^{(IE,OE)}\hat{C}^{(OE,OA)}\vec{u}_3$$
$$+\dot{\psi}_1\hat{\dot{C}}^{(IA,IE)}\hat{C}^{(IE,OE)}\hat{C}^{(OE,OA)}\vec{u}_3$$
$$+\dot{\psi}_1\hat{C}^{(IA,IE)}\hat{\dot{C}}^{(IE,OE)}\hat{C}^{(OE,OA)}\vec{u}_3$$
$$+\dot{\psi}_1\hat{C}^{(IA,IE)}\hat{C}^{(IE,OE)}\hat{\dot{C}}^{(OE,OA)}\vec{u}_3$$

With those simplifications, the Euler's equation for the outer azimuth axis becomes

$$\begin{bmatrix} J_{OA1} & 0 & 0 \\ 0 & J_{OA2} & 0 \\ 0 & 0 & J_{OA3} \end{bmatrix}\begin{bmatrix} 0 \\ 0 \\ \ddot{\psi}_1 \end{bmatrix} + \begin{bmatrix} 0 \\ 0 \\ \dot{\psi}_1 \end{bmatrix} \times \begin{bmatrix} J_{OA1} & 0 & 0 \\ 0 & J_{OA2} & 0 \\ 0 & 0 & J_{OA3} \end{bmatrix}\begin{bmatrix} 0 \\ 0 \\ \dot{\psi}_1 \end{bmatrix} \tag{2.59}$$
$$= \begin{bmatrix} M_{B,OA,1} \\ M_{B,OA,2} \\ T_{m,B,OA} + T_{fr,B,OA} \end{bmatrix} + \begin{bmatrix} M_{OE,OA,1} \\ M_{OE,OA,2} \\ M_{OE,OA,3} \end{bmatrix} + \begin{bmatrix} M_{IA,OA,1} \\ M_{IA,OA,2} \\ M_{IA,OA,3} \end{bmatrix} + \begin{bmatrix} 0 \\ 0 \\ D_{OA} \end{bmatrix}$$

The matrix equation can be decomposed into three scalar equations

$$M_{IA,OA,1} + M_{OE,OA,1} + M_{B,OA,1} = 0 \tag{2.60}$$
$$M_{IA,OA,2} + M_{OE,OA,2} + M_{B,OA,2} = 0 \tag{2.61}$$
$$J_{OA3}\,\ddot{\psi}_1 = M_{OE,OA,3} + M_{IA,OA,3} + T_{m,B,OA} + T_{fr,B,OA}+D_{OA} \tag{2.62}$$

The Euler's equation for the outer elevation axis becomes

$$\begin{bmatrix} J_{OE1} & 0 & 0 \\ 0 & J_{OE2} & 0 \\ 0 & 0 & J_{OE3} \end{bmatrix} \begin{bmatrix} -\dot{\theta}_1\dot{\psi}_1\cos(\theta_1) - \ddot{\psi}_1\sin(\theta_1) \\ \ddot{\theta}_1 \\ -\dot{\theta}_1\dot{\psi}_1\sin(\theta_1) + \ddot{\psi}_1\cos(\theta_1) \end{bmatrix} + \tag{2.63}$$

$$\begin{bmatrix} -\dot{\psi}_1\sin(\theta_1) \\ \ddot{\theta}_1 \\ \dot{\psi}_1\cos(\theta_1) \end{bmatrix} \times \begin{bmatrix} J_{OE1} & 0 & 0 \\ 0 & J_{OE2} & 0 \\ 0 & 0 & J_{OE3} \end{bmatrix} \begin{bmatrix} -\dot{\psi}_1\sin(\theta_1) \\ \ddot{\theta}_1 \\ \dot{\psi}_1\cos(\theta_1) \end{bmatrix} =$$

$$\begin{bmatrix} M_{B,OE1} \\ T_{m,B,OE} + T_{frB,OE} \\ M_{B,OE,3} \end{bmatrix} + \begin{bmatrix} M_{OA,OE1} \\ T_{m,OA,OE} + T_{fr,OA,OE} \\ M_{OA,OE,3} \end{bmatrix} +$$

$$\begin{bmatrix} M_{IE,OE1} \\ T_{m,IE,OE} + T_{fr,IE,OE} \\ M_{IE,OE,3} \end{bmatrix} + \begin{bmatrix} 0 \\ D_{OE} \\ 0 \end{bmatrix}$$

The matrix equation can be decomposed into three scalar equations

$$J_{OE1}\left[-\dot{\theta}_1\dot{\psi}_1\cos(\theta_1) - \ddot{\psi}_1\sin(\theta_1)\right] \tag{2.64}$$
$$+(J_{OE3} - J_{OE2})\,\dot{\theta}_1\dot{\psi}_1\cos(\theta_1)$$
$$= M_{B,OE1} + M_{OA,OE1} + M_{IE,OE1}$$

$$J_{OE2}\ddot{\theta}_1 + (J_{OE3} - J_{OE1})\,\dot{\psi}_1^{\,2}\sin(\theta_1)\cos(\theta_1) \tag{2.65}$$
$$= T_{m,B,OE} + T_{fr,B,OE} + T_{m,OA,OE} + T_{fr,OA,OE} + D_{OE}$$

$$J_{OE3}[-\dot{\theta}_1\dot{\psi}_1\sin(\theta_1) + \ddot{\psi}_1\cos(\theta_1)] \tag{2.66}$$
$$+(J_{OE1} - J_{OE2})\,\dot{\theta}_1\dot{\psi}_1\sin(\theta_1)$$
$$= M_{B,OE,3} + M_{OA,OE,3} + M_{IE,OE,3}$$

The Euler's equation for the inner elevation axis becomes

$$\begin{bmatrix} J_{IE1} & 0 & 0 \\ 0 & J_{IE2} & 0 \\ 0 & 0 & J_{IE3} \end{bmatrix} \begin{bmatrix} -\ddot{\psi}_1\cos(\theta_1+\theta_2) + (\dot{\theta}_1 - \dot{\theta}_2)\dot{\psi}_1\cos(\theta_1+\theta_2) \\ 2\ddot{\theta}_1 \\ \ddot{\psi}_1\cos(\theta_1+\theta_2) - (\dot{\theta}_2 + \dot{\theta}_1)\dot{\psi}_1\sin(\theta_1+\theta_2) \end{bmatrix} + \tag{2.67}$$

$$\begin{bmatrix} \dot{\psi}_1 \sin(\theta_1+\theta_2) \\ (\dot{\theta}_2+\dot{\theta}_1) \\ \dot{\psi}_1 \cos(\theta_1+\theta_2) \end{bmatrix} \text{x} \begin{bmatrix} J_{IE1} & 0 & 0 \\ 0 & J_{IE2} & 0 \\ 0 & 0 & J_{IE3} \end{bmatrix} \begin{bmatrix} \dot{\psi}_1 \sin(\theta_1+\theta_2) \\ (\dot{\theta}_2+\dot{\theta}_1) \\ \dot{\psi}_1 \cos(\theta_1+\theta_2) \end{bmatrix}$$

$$= \begin{bmatrix} M_{OE,IE1} \\ T_{m,OE,IE} + T_{fr,OE,IE} \\ M_{OE,IE,3} \end{bmatrix} + \begin{bmatrix} M_{IA,IE,1} \\ M_{IA,IE,2} \\ M_{IA,IE,3} \end{bmatrix} + \begin{bmatrix} 0 \\ D_{OE} \\ 0 \end{bmatrix}$$

The matrix equation can be decomposed into three scalar equations

$$J_{IE1}\left[-\ddot{\psi}_1 \cos(\theta_1+\theta_2) + \left(\dot{\theta}_1 - \dot{\theta}_2\right)\dot{\psi}_1 \cos(\theta_1+\theta_2)\right] + \dot{\psi}_1(\dot{\theta}_2+\dot{\theta}_1)\cos(\theta_1+\theta_2)(J_{IE3} - J_{IE2}) = M_{OE,IE1} + M_{IA,IE,1} \tag{2.68}$$

$$J_{IE2} 2\ddot{\theta}_1 + \dot{\psi}_1{}^2 \sin(\theta_1+\theta_2)\cos(\theta_1+\theta_2)\,(J_{IE3} - J_{IE1}) = T_{m,B,IE} + T_{fr,B,IE} + M_{IA,IE,2} + D_{OE} \tag{2.69}$$

$$J_{IE3}\left[\ddot{\psi}_1 \cos(\theta_1+\theta_2) + \left(\dot{\theta}_2 + \dot{\theta}_1\right)\dot{\psi}_1 \sin(\theta_1+\theta_2)\right] + \dot{\psi}_1(\dot{\theta}_2+\dot{\theta}_1)\sin(\theta_1+\theta_2)(J_{IE1} - J_{IE2}) = M_{OE,IE,3} + M_{IA,IE,3} \tag{2.70}$$

The Euler's equation for the inner azimuth axis becomes

$$
\begin{bmatrix} J_{IA1} & 0 & 0 \\ 0 & J_{IA2} & 0 \\ 0 & 0 & J_{IA3} \end{bmatrix}
\begin{bmatrix} \left(\ddot{\theta}_1+\ddot{\theta}_2\right)\sin\psi_2+\dot{\psi}_2\left(\dot{\theta}_1+\dot{\theta}_2\right)\cos\psi_2+\sin(\theta_1+\theta_2)[\dot{\psi}_1\dot{\psi}_2\sin\psi_2-\ddot{\psi}_1\cos\psi_2]-(\dot{\theta}_2+\dot{\theta}_1)\dot{\psi}_1\cos\psi_2\cos(\theta_1+\theta_2) \\ \left(\ddot{\theta}_1+\ddot{\theta}_2\right)\cos\psi_2+\dot{\psi}_2\left(\dot{\theta}_1+\dot{\theta}_2\right)\sin\psi_2+\sin(\theta_1+\theta_2)[\dot{\psi}_1\dot{\psi}_2\cos\psi_2-\ddot{\psi}_1\sin\psi_2]-(\dot{\theta}_2+\dot{\theta}_1)\dot{\psi}_1\sin\psi_2\cos(\theta_1+\theta_2) \\ \ddot{\psi}_2+\ddot{\psi}_1\cos(\theta_1+\theta_2)-(\dot{\theta}_2+\dot{\theta}_1)\dot{\psi}_1\sin(\theta_1+\theta_2) \end{bmatrix}
\tag{2.71}
$$

$$
+\begin{bmatrix} \left(\dot{\theta}_1+\dot{\theta}_2\right)\sin\psi_2-\dot{\psi}_1\cos\psi_2\sin(\theta_1+\theta_2) \\ \left(\dot{\theta}_1+\dot{\theta}_2\right)\cos\psi_2+\dot{\psi}_1\sin\psi_2\sin(\theta_1+\theta_2) \\ \dot{\psi}_2+\dot{\psi}_1\cos(\theta_1+\theta_2) \end{bmatrix}
\mathrm{x}
\begin{bmatrix} J_{IA1} & 0 & 0 \\ 0 & J_{IA2} & 0 \\ 0 & 0 & J_{IA3} \end{bmatrix}
\begin{bmatrix} \left(\dot{\theta}_1+\dot{\theta}_2\right)\sin\psi_2-\dot{\psi}_1\cos\psi_2\sin(\theta_1+\theta_2) \\ \left(\dot{\theta}_1+\dot{\theta}_2\right)\cos\psi_2+\dot{\psi}_1\sin\psi_2\sin(\theta_1+\theta_2) \\ \dot{\psi}_2+\dot{\psi}_1\cos(\theta_1+\theta_2) \end{bmatrix}
$$

$$
=\begin{bmatrix} M_{OA,IA,1} \\ M_{OA,IA,2} \\ M_{OA,IA,3} \end{bmatrix}+\begin{bmatrix} M_{IE,IA,1} \\ M_{IE,IA,2} \\ T_{m,IE,IA}+T_{fr,IE,IA} \end{bmatrix}+\begin{bmatrix} 0 \\ 0 \\ D_{IA} \end{bmatrix}
$$

The matrix equation can be decomposed into three scalar equations

$$J_{IA1}[(\ddot{\theta}_1+\ddot{\theta}_2)\sin\psi_2$$
$$+\dot{\psi}_2(\dot{\theta}_1+\dot{\theta}_2)\cos\psi_2 +$$
$$\sin(\theta_1+\theta_2)[\dot{\psi}_1\dot{\psi}_2\sin\psi_2-\ddot{\psi}_1\cos\psi_2] -$$
$$(\dot{\theta}_2+\dot{\theta}_1)\dot{\psi}_1\cos\psi_2\cos(\theta_1+\theta_2)]$$
$$+(J_{IA3}-J_{IA2})(\dot{\psi}_2+\dot{\psi}_1\cos(\theta_1+\theta_2))[(\dot{\theta}_1+\dot{\theta}_2)\cos\psi_2 +$$
$$\dot{\psi}_1\sin\psi_2\sin(\theta_1+\theta_2)]$$
$$= M_{OA,IA,1}+M_{IE,IA,1} \tag{2.72}$$

$$J_{IA2}\,[(\ddot{\theta}_1+\ddot{\theta}_2)\cos\psi_2 +$$
$$\dot{\psi}_2(\dot{\theta}_1+\dot{\theta}_2)\sin\psi_2+\sin(\theta_1+\theta_2)[\dot{\psi}_1\dot{\psi}_2\cos\psi_2-\ddot{\psi}_1\sin\psi_2] -$$
$$(\dot{\theta}_2+\dot{\theta}_1)\dot{\psi}_1\sin\psi_2\cos(\theta_1+\theta_2)] +(J_{IA1}-J_{IA3})(\dot{\psi}_2 +$$
$$\dot{\psi}_1\cos(\theta_1+\theta_2))\left[(\dot{\theta}_1+\dot{\theta}_2)\sin\psi_2-\dot{\psi}_1\cos\psi_2\sin(\theta_1+\theta_2)\right]$$
$$= M_{OA,IA,2}+M_{IE,IA,2} \tag{2.73}$$

$$J_{IA3}[\ddot{\psi}_2+\ddot{\psi}_1\cos(\theta_1+\theta_2)-(\dot{\theta}_2+\dot{\theta}_1)\dot{\psi}_1\sin(\theta_1+\theta_2)] +$$
$$+(J_{IA2}-J_{IA1})\,[(\ddot{\theta}_1+\ddot{\theta}_2)\sin\psi_2 +$$
$$\dot{\psi}_2(\dot{\theta}_1+\dot{\theta}_2)\cos\psi_2+\sin(\theta_1+\theta_2)[\dot{\psi}_1\dot{\psi}_2\sin\psi_2-\ddot{\psi}_1\cos\psi_2] -$$
$$(\dot{\theta}_2+\dot{\theta}_1)\dot{\psi}_1\cos\psi_2\cos(\theta_1+\theta_2)]$$
$$[(\ddot{\theta}_1+\ddot{\theta}_2)\cos\psi_2 +$$
$$\dot{\psi}_2(\dot{\theta}_1+\dot{\theta}_2)\sin\psi_2+\sin(\theta_1+\theta_2)[\dot{\psi}_1\dot{\psi}_2\cos\psi_2-\ddot{\psi}_1\sin\psi_2] -$$
$$(\dot{\theta}_2+\dot{\theta}_1)\dot{\psi}_1\sin\psi_2\cos(\theta_1+\theta_2)]$$
$$= D_{IA}+T_{m,IE,IA}+T_{fr,IE,IA}+M_{OA,IA,3} \tag{2.74}$$

2.3 Karnopp Friction Model

A basic friction model contains Coulomb friction and linear viscous damping. In a certain velocity region near the zero velocity, friction decreases with the increasing velocity [12]. This situation is called Stribeck effect, show in Figure 2.3. Friction force cannot be expressed as a function of velocity where the velocity equals to zero. The discontinuity of the friction function results in numerical difficulties in this velocity region. Therefore, a friction model containing a hysteresis loop is necessary. Coulomb, viscous and Stribeck friction model is

$$F_f = F_c \operatorname{sgn}(v) + F_v v + F_s(v) \tag{2.75}$$

where;

F_f : Friction force,

F_c : Coulomb friction force,

F_v : Viscous friction coefficient,

F_s : Stribeck function of velocity.

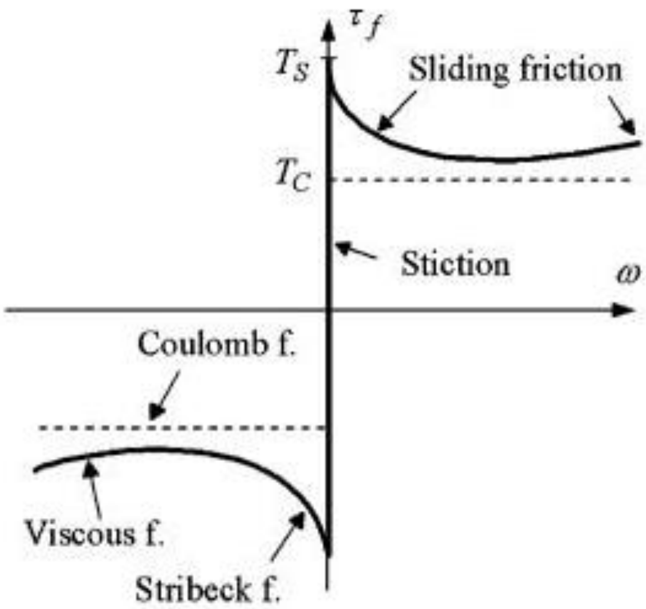

Figure 2.3: Coulomb, viscous and Stribeck Model of Friction [13]

Although the friction model shown in Figure 2.3 is useful for steady velocities, it causes numerical difficulties in the region where velocity crosses $v = 0$. Karnopp friction model, shown in Figure 2.4, is used in the simulations in order to get rid of these numerical difficulties. In Karnopp model, the friction force is equal to the force acting on the object around the neighborhood of $v = 0$. Outside the neighborhood of $v = 0$, friction force is a function of velocity [14].

$$F_f = \begin{cases} -F_c \mathrm{sgn}(v) - F_v v & \text{if } |v| >= DV \\ -F_{ext} - kv & if\ |\dot{v}| < DV\ and\ |F_{ext} - kv| < F_s \\ -F_s\ sgn(F_{ext} - kv) & \text{if } |\dot{v}| < DV\ and\ |F_{ext} - kv| < F_s \end{cases} \tag{2.76}$$

where;

$$\Delta\omega = 2\ DV \tag{2.77}$$

F_c : Coulomb friction coefficient,

F_v : Viscous friction coefficient,

F_s : Static friction coefficient,

DV : Limit velocity.

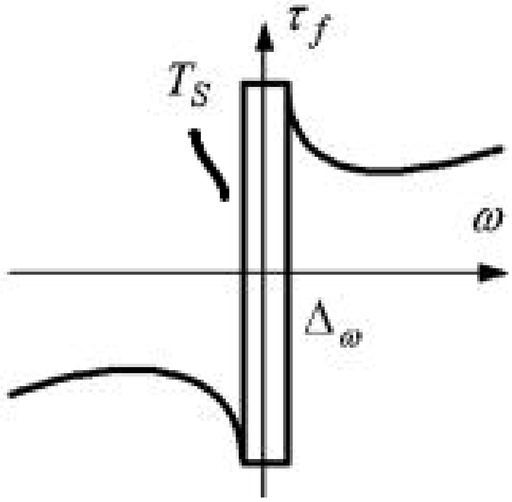

Figure 2.4: Karnopp Friction Model Containing Hysteresis Loop [13]

2.4 Kalman Filtering

In this section, Kalman filter, which will be used in order to filter out the gyroscope measurement noise, is explained. Basicaly, Kalman filter is a state estimator that makes use of the measured data and the system matrices. We have a linear discrete time system described as:

$$x_k = Ax_{k-1} + Bw_k \tag{2.78}$$

$$y_k^1 = Cx_k + v_k \tag{2.79}$$

where;

x_k : the state of the system at time k

y_k : the output of the system

w_k : the process noise

v_k : the measurement noise

The w_k and v_k are zero-mean, white and uncorrelated noise processes with covariance matrices Q_k and R_k, respectively [15].

Prediction Update:

$$\hat{x}^1_{k|k-1} = A\hat{x}^1_{k-1|k-1} \tag{2.80}$$

$$P^1_{k|k-1} = AP^1_{k-1|k-1}A + BQB^T \tag{2.81}$$

Measurement Update:

$$\hat{x}^1_{k|k} = \hat{x}^1_{k|k-1} + K^1_k\left(y^1_k - \hat{y}^1_{k|k-1}\right) \tag{2.82}$$

$$P^1_{k|k} = P^1_{k|k-1} - K^1_k S^1_{k|k-1}(K^1_k)^T \tag{2.83}$$

where

$$\hat{y}^1_{k|k-1} = C\hat{x}^1_{k|k-1} \tag{2.84}$$

$$S^1_{k|k-1} = CP^1_{k|k-1}C^T + R_1 \tag{2.85}$$

$$K^1_k = P^1_{k|k-1}C^T(S^1_{k|k-1})^{-1} \tag{2.86}$$

The aim of the Kalman filter is to estimate the state x_k with the presence of output measurements y_k with the noise process v_k, and with the information about the linear model of system. The Kalman filter has 2 parts; the prediction update and the measurement update. By the knowledge of system matrices, we can have a prediction of the next state $\hat{x}^1_{k|k-1}$ and covariance matrix $P^1_{k|k-1}$ belonging to time k, with the use of A and B matrices of equation (2.78). After obtaining the predicted state, we can correct it with the measurement update part. Measurement update basically minimizes the error between the measured output and the predicted output of the system. Kalman filter is the optimal filter minimizing the estimation error.

In this study, Kalman filter is used in order to fuse the encoder and gyroscope data. The system matrices, process and measurement noise covariance matrices are defined in (2.87), (2.88), (2.89), (2.90), (2.91) and (2.92).

$$A = \begin{bmatrix} 1 & \mathrm{T} & \frac{1}{2}T^2 \\ 0 & 1 & T \\ 0 & 0 & 1 \end{bmatrix} \quad (2.87)$$

$$B = \begin{bmatrix} \frac{1}{2}T^2 \\ T \\ 1 \end{bmatrix} \quad (2.88)$$

$$C = [1\ 1\ 0] \quad (2.89)$$

$$R = \begin{bmatrix} \frac{1}{12}(549 * 10^{-5})^2 & 0 \\ 0 & \frac{1}{12}(549 * 10^{-5})^2 \end{bmatrix} \quad (2.91)$$

$$Q = 100 \quad (2.92)$$

where T is the sampling time of the slowest sensor. This fusion Kalman filter algorithm evaluates position, velocity and acceleration and filters out the noises coming from the encoder and gyroscope.

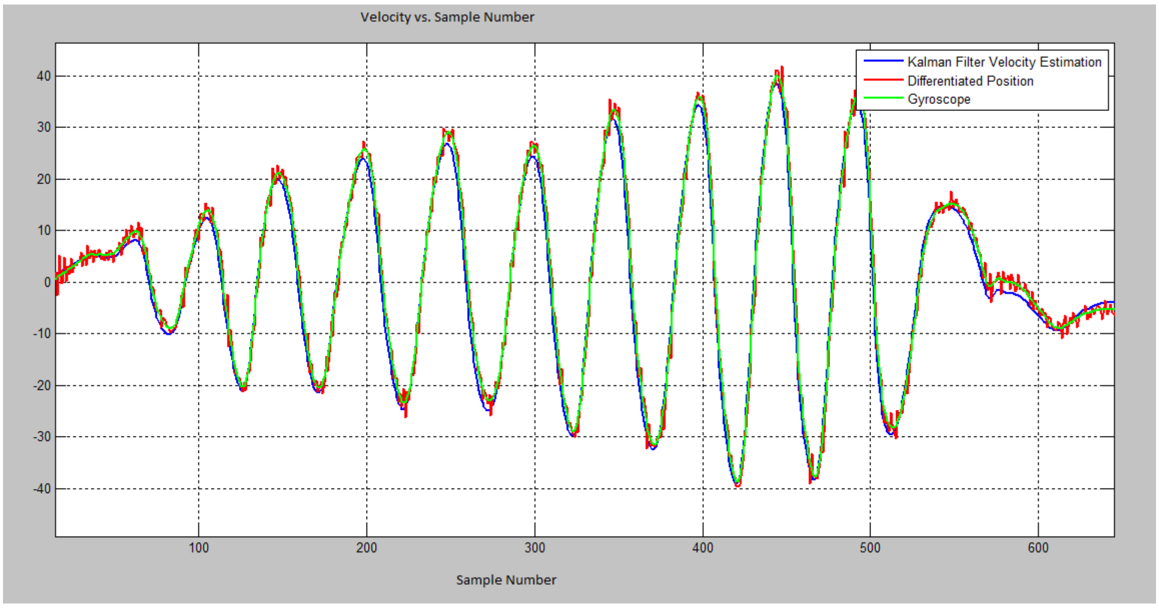

Figure 2.5: Velocity vs Sample Number

The comparison of velocity estimation throughout the encoder and gyroscope data taken from the real system with the gyroscope data and the encoder data with noise can be seen from Figure 2.5. Kalman filter estimates the velocity state using both the encoder and the gyroscope data. The fusion of the sensor data is crucial for the control to be done properly.

CHAPTER 3

MODELING AND SIMULATION USING GYROSCOPE FEEDBACK

In this chapter, simulation model is built in MATLAB Simulink environment according to the mathematical model given in Chapter 2. Simulation model is required for the control algorithm to be developed since it provides the opportunity to test the algorithms without running the actual system. Parameters of the simulation model of the 4-DOF platform are found by a system identification procedure, which is explained in the next section, utilizing the measured data gathered from the actual system. The transfer function of the fiber-optic gyroscope, which gives us the velocity measurements, is also found by a different system identification procedure, which is the ARMAX model, since the accurate relationship between the actual velocity and the measured one is required. In order to achieve this, gyroscope data are acquired from the rate table tests.

3.1 Identification of the Parameters of Each 4 Gimbal Platform

From the mathematical model of the 4-DOF platform, we deduce that the system parameters to be identified are the Newton-Euler equation parameters. In order for the parametric system identification to be done, command velocity input is given to each gimbal separately, and gyroscope velocity measurements are recorded. According to output-error parametric estimation method in [16], [17], looking at the difference between the actual system measurements and the simulation model output, we can judge the accuracy of the simulation model.

Let Φ be the parameter vector. The cost function to be minimized is:

$$\frac{1}{N}\sum_{k=1}^{N-1}||y(k)-\hat{y}(k,\Phi)||_{2}^{2} \tag{3.1}$$

where $y(k)$ is the measured velocity data by gyroscope and $\hat{y}(k,\Phi)$ is the output of the simulation model for a value of the parameter vector, Φ [16]. Let the optimal parameter vector $\widehat{\Phi}_N$ be the argument of (3.1) that minimizes this cost function:

$$\widehat{\Phi}_N = \text{arg min}\,\frac{1}{N}\sum_{k=1}^{N-1}||y(k)-\hat{y}(k,\Phi)||_2^2 \tag{3.2}$$

In other words, the parameters must be optimized in such a way that the difference between the model output with a selected parameter set Φ and the logged data from the real platform must be minimized.

The difference between model output and the logged data from the real system, when same inputs are given to the real system and simulation model, are minimized utilizing **fmincon** MATLAB function, which uses the gradient-descent optimization algorithm. The logged data and the simulation output plot is in Figure 3.1. The plots belonging to outer azimuth, outer elevation, inner elevation and inner azimuth gimbals are shown respectively in the Figure 3.1. The blue lines are the simulation outputs, whereas the gray lines are the real system output. The optimization algorithm makes these lines closer by adjusting the system parameters specified in the Newton-Euler equations.

In order to identify the Karnopp friction model parameters, outer azimuth and inner elevation axes are commanded by pulse waveform in 4 Hz frequency. No excitation is given to the outer elevation and inner azimuth gimbals.

After the iterations of the gradient-descent optimization algorithm has finished, the value of the minimized cost function in (3.1) becomes 217.93, which was 384.43 initially. This is because there are 52 parameters to be optimized in the simulation, which will be mentioned in the following sections. The parameters of the model imported from Solidworks to MATLAB and the identified parameters are given in Table 3.1.

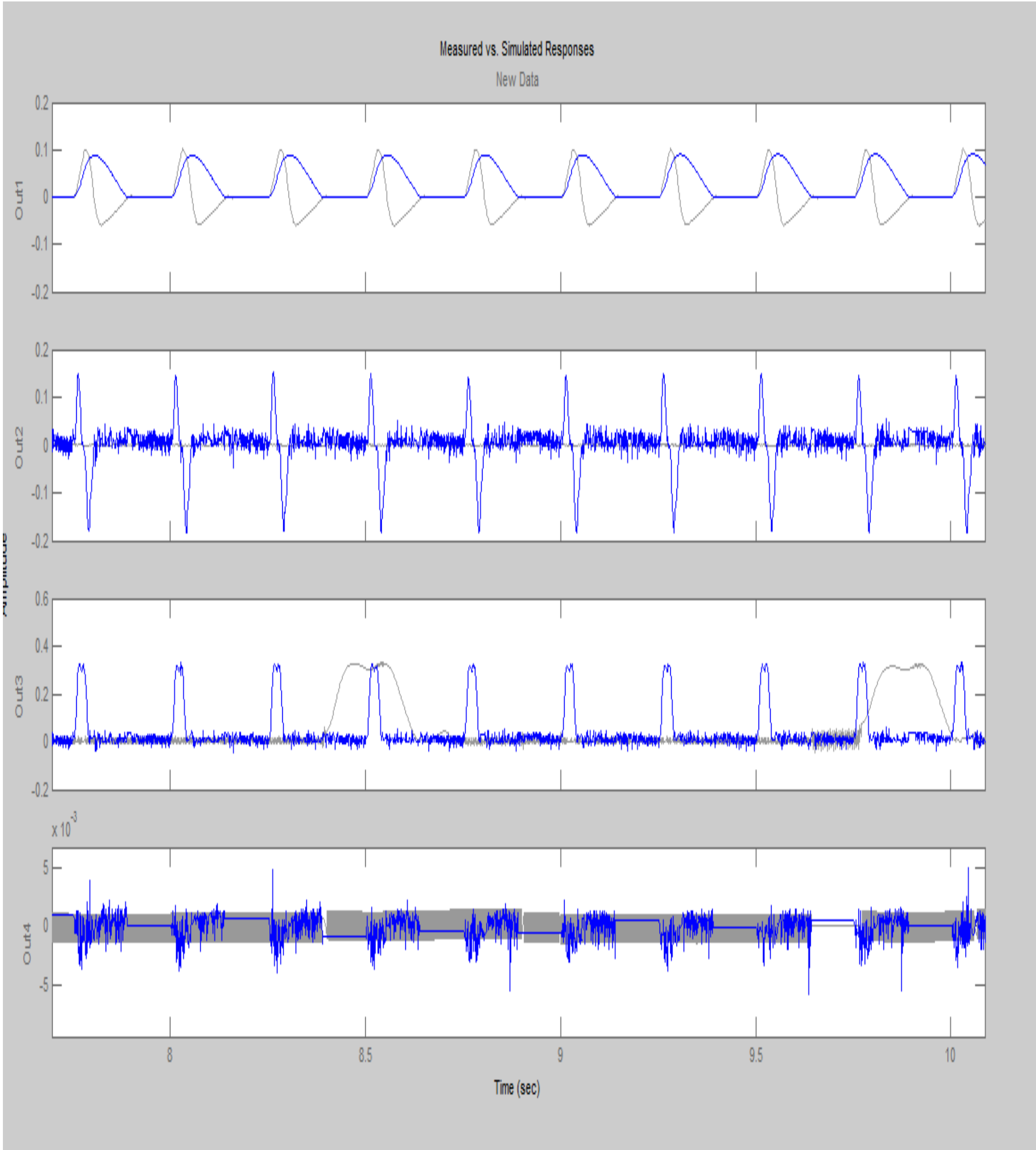

Figure 3.1: The Simulation Outputs (Blue) and Logged Data from the Real System (Gray)

3.1.1 Outer Azimuth Parameters

The mass of the outer azimuth gimbal is identified as 6.0746 kg. The coordinates of the center of gravity of the gimbal is [106.638 -0.0293 -0.293] in milimeters. The diagonal parameters of the moments of inertia tensor matrix are 977490, 497910 and 1053100 kg*mm^2, respectively. Products of inertia vector components are 0.1613, 0,098 and -537,0095 kg*mm^2, respectively.

3.1.2 Outer Elevation Parameters

The mass of the outer elevation gimbal is identified as 3.0676 kg. The coordinates of the center of gravity of the gimbal is [-0.6527 -0.844 -2.5581] in milimeters. The diagonal parameters of the moments of inertia tensor matrix are 19368, 18733 and 19113 kg*mm^2, respectively. Products of inertia vector components are 118,6182, 47,1553 and -16,9277 kg*mm^2, respectively.

3.1.3 Inner Elevation Parameters

The mass of the inner elevation gimbal is identified as 2.3726 kg. The coordinates of the center of gravity of the gimbal is [-6.4687 -5.2779 40.2476] in milimeters. The diagonal parameters of the moments of inertia tensor matrix is 40139.2, 35324.2 and 72346.3 kg*mm^2, respectively. Products of inertia vector components are -20.402, -68.373 and 365.02 kg*mm^2, respectively.

3.1.4 Inner Azimuth Parameters

The mass of the inner azimuth gimbal is identified as 5.7257 kg. The coordinates of the center of gravity of the gimbal is [0 0.182 100] in milimeters. The diagonal parameters of the moments of inertia tensor matrix are 71043.8, 64755.3 and 87031 kg*mm^2, respectively. Products of inertia vector components are zero kg*mm^2.

3.1.5 Karnopp Friction Parameters

The friction between outer azimuth and outer elevation gimbals are 0.4690 for Coulomb friction coefficient, 3.2309 for viscous friction coefficient, 8.8244 for Stiction coefficient and 2.8397 for Stribeck effect coefficient. The friction between outer elevation and inner elevation gimbals are 3.4845 for Coulomb friction coefficient, 0.2951 for viscous friction coefficient, 8.3661 for Stiction coefficient and 2.8364 for Stribeck effect coefficient. The friction between outer elevation and inner elevation gimbals are 1.0805 for Coulomb friction coefficient, 2.6733 for viscous friction coefficient, 2.6231 for Stiction coefficient and 2.9048 for Stribeck effect coefficient. The friction parameters are tabulated in Table 3.2.

Table 3.1: Output Error Parametric System Identification Values

Parameter	CAD Import Value	Identified Value	Unit
m_oa	5,012	6,0746	kg
r_oa1	-106,638	-106,9867	mm
r_oa2	0	-82,3952	mm
r_oa3	0	37,2439	mm
J_oa1	977487	977490	kg*mm^2
J_oa2	497908	497910	kg*mm^2
J_oa3	1053090	1053100	kg*mm^2
P_oa1	0	-32,6177	kg*mm^2
P_oa2	0	-37,5059	kg*mm^2
P_oa3	-537,008	-536,967	kg*mm^2
m_oe	0,699618	3,0676	kg
r_oe1	-0,28	85,2266	mm
r_oe2	-0,844	-0,29124	mm
r_oe3	-3,44	-7,3656	mm
J_oe1	19368	19368	kg*mm^2
J_oe2	18732,6	18733	kg*mm^2
J_oe3	19113,09	19113	kg*mm^2
P_oe1	118,61	118,6182	kg*mm^2
P_oe2	47,15	47,1553	kg*mm^2
P_oe3	-17,2	-16,9277	kg*mm^2

Table 3.1: Output Error Parametric System Identification Values (Continued)

m_ie	2,24084	2,3726	kg
r_ie1	-6,4687	-1,5509	mm
r_ie2	-5,2779	6,3448	mm
r_ie3	40,2746	4,6835	mm
J_ie1	40139,2	40139,2000	kg*mm^2
J_ie2	35324,2	35324,2000	kg*mm^2
J_ie3	72346,3	72346,3000	kg*mm^2
P_ie1	-20,402	-25,1181	kg*mm^2
P_ie2	-68,373	-64,6992	kg*mm^2
P_ie3	365,02	364,9260	kg*mm^2
m_ia	7,3589	5,7257	kg
r_ia1	0	37,2439	mm
r_ia2	0,1819	26,9604	mm
r_ia3	100	98,6244	mm
J_ia1	71043,8	71043,8000	kg*mm^2
J_ia2	64755,3	64755,3000	kg*mm^2
J_ia3	87031	87031,0000	kg*mm^2
P_ia1	0	-10,2966	kg*mm^2
P_ia2	0	-44,3454	kg*mm^2
P_ia3	0	-55,7843	kg*mm^2

Table 3.2: Friction Parameters

	Between OA and OE	Between OE and IE	Between IE and IA
CoulombFriction	0,469	3,4845	1,0805
ViscousFriction	3,2309	0,2951	2,6733
StaticFriction	8,8244	8,3661	2,6231
wStribeck	2,8397	2,8364	2,9048

3.2 Identification of the Fiber-Optic Gyroscope Transfer Function

Inertial sensors (gyroscopes) have distinct error characteristics such as bias, scale factor, random walk, etc. Calibration and characterization tests are done with 2 or 3 axes rate tables in order to identify these errors [40]. For stabilization and control of the 4-DOF platform, fiber-optic gyroscopes are used. Since fiber-optic gyroscope parameters are not easy to define [18], we will construct a transfer function from input and output time-domain data of the gyroscope. The data acquisition is carried out with the aid of a rate table, an xPC target box (a hardware-in-loop simulation tool for MATLAB) and a digital signal analyzer. Rate table gives the movement to the gyroscope to be measured. The gyroscope and xPC target box transceive RS-422 data. The digital signal analyzer takes the velocity information of the physical movement of the rate table as an input of the gyroscope, and the analog velocity information coming from xPC target box as an output of the gyroscope. With that information, the system identification according to the ARMAX model can be carried out.

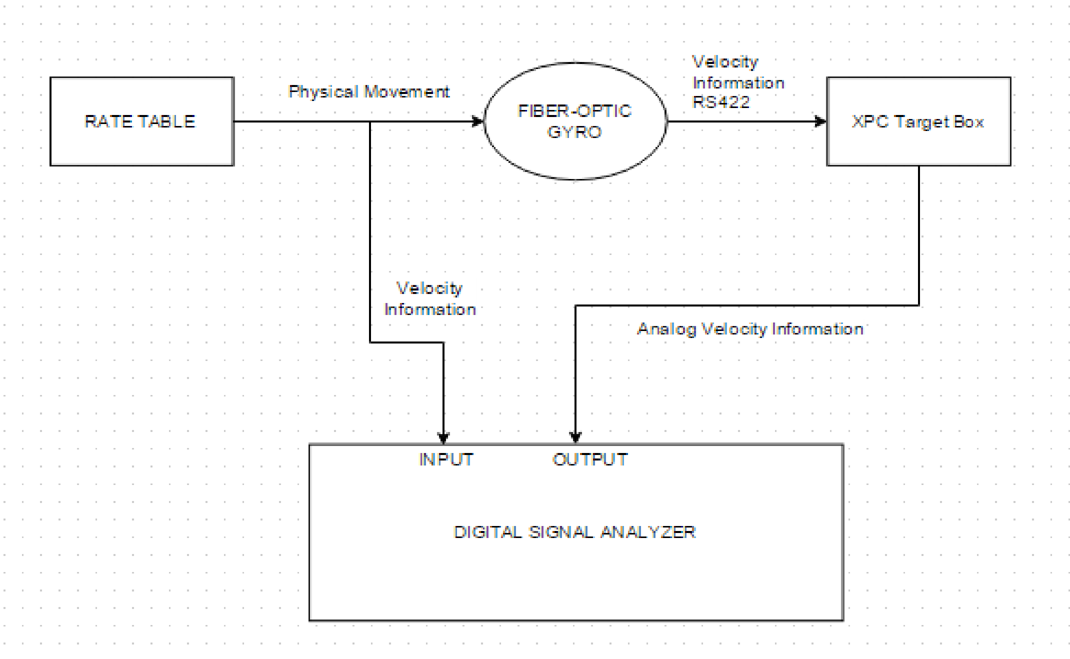

Figure 3.2: Gyroscope Test Setup Block Diagram

The gain and phase relating the input and output data of the fiber-optic gyroscope is shown in Figure 3.2.

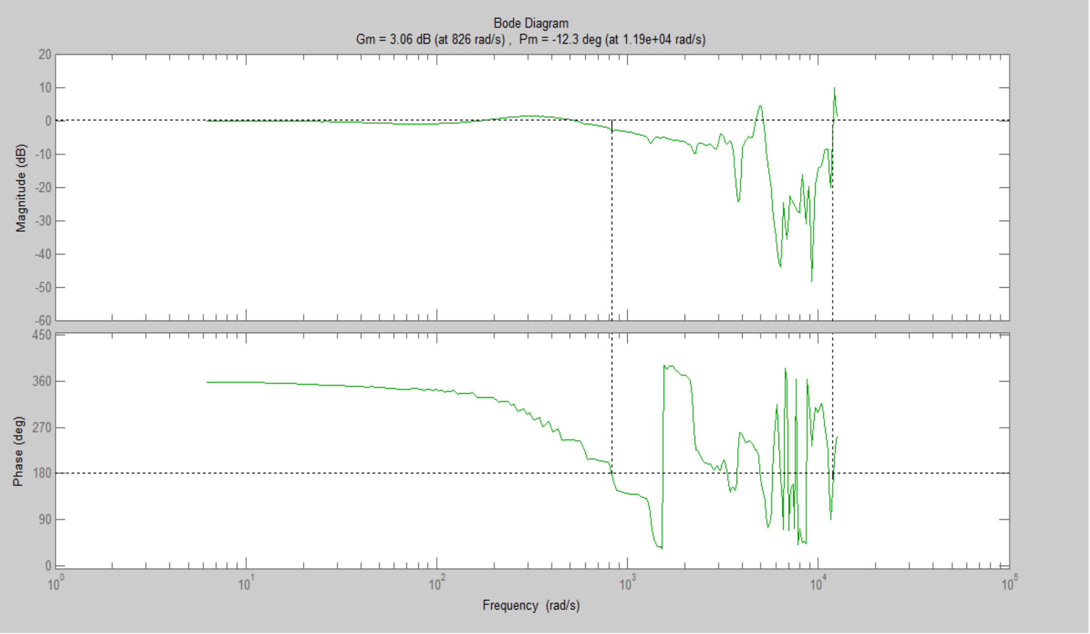

Figure 3.3: Gyroscope Frequency Domain Data

Before jumping into the results, we will have a look at the ARMAX model. Suppose we have an input-output time domain data sequence which will be utilized for identification of the transfer function of the system

$$y(k) = G(q)\, u(k) + H(q)\, e(k) \tag{3.3}$$

where e(k) is the zero-mean white noise sequence, which is independent from the sequence u(k). G(s) is the deterministic part where H(s) is the stochastic part of the system [16]. The ARMAX (Auto-Regressive Moving Average with eXogenous input) model structure is the following specific case of general input–output description [16]:

$$y(k) = \frac{b_1 q^{-1} + \ldots + b_n q^{-n}}{1 + a_1 q^{-1} + \ldots + a_n q^{-n}}\, u(k) + \frac{1 + c_1 q^{-1} + \ldots + c_n q^{-n}}{1 + a_1 q^{-1} + \ldots + a_n q^{-n}}\, e(k) \tag{3.4}$$

Since ARMAX model is a time-domain model, the response to the chirp signal from 1 Hz to 1 kHz in time interval of 50 seconds is given in Figure 3.4. Since the Bode-plot in Figure 3.3 has distortions beyond 1 kHz, the upper frequency limit is chosen as 1 kHz.

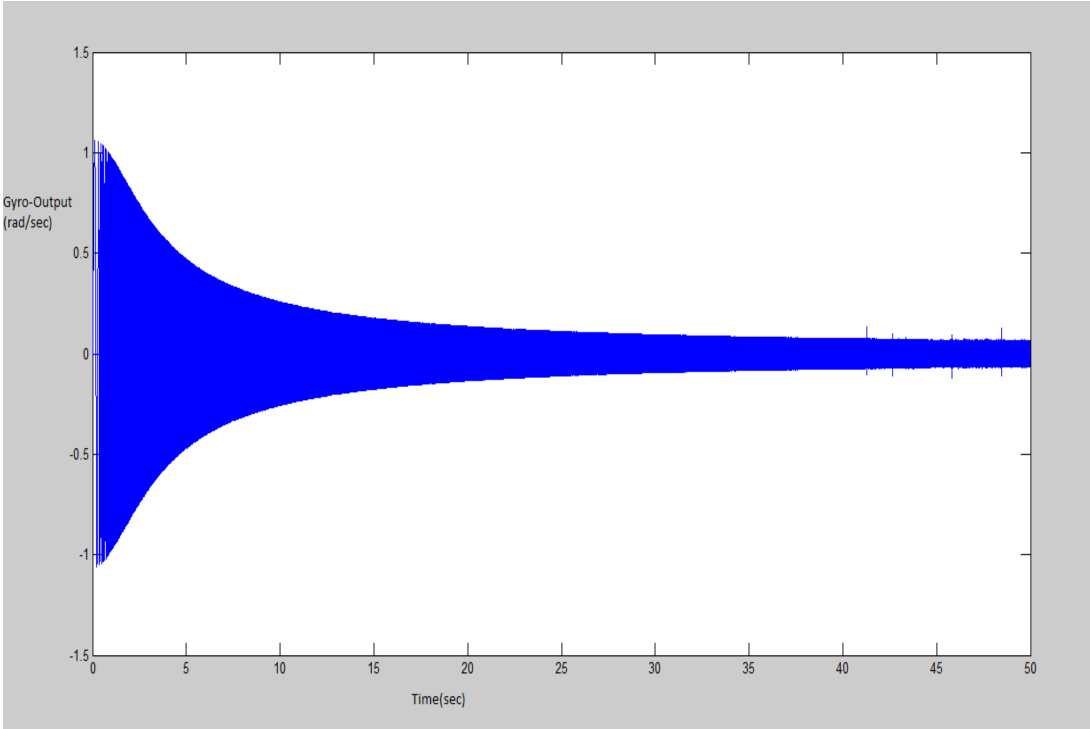

Figure 3.4: Gyro Output Data with 1Hz-to-1kHz Chirp Input

Using the ARMAX model system identification, the gyroscope has a transfer function

$$y(k)=\frac{-0.001659z^{-1}+0.001355z^{-2}}{1-0.8292z^{-1}-0.1708z^{-2}}\,u(k)+\frac{1+0.00142z^{-1}-0.989z^{-2}}{1-0.8292z^{-1}-0.1708z^{-2}}\,e(k) \tag{3.5}$$

The broadband excitation signal is used since the dynamic behaviour of a mechanical system is obtained from input and output signals, strictly speaking, nonparametric measurements [19]. The measurement errors of the gyroscope data will be corrected, together with the encoder data. This is carried out using a Kalman filter, which is presented in Section 2.4.

CHAPTER 4

CONSTRUCTION OF THE SIMULATION MODEL

For the purpose of designing and testing different control algorithms, an accurate simulation model of the 4-DOF platform is necessary, since simulation provides the opportunity to see the system response without running it physically. With Matlab SimMechanics, mechanical systems can be simulated on 3-D models besides being connected to other Simulink blocks through sensor and actuator blocks, which enables us to implement several controllers. Moreover, CAD models can be imported on Matlab SimMechanics which provides accuracy to the SimMechanics blocks [20]. In our simulation, the 4-DOF platform's SimMechanics model is imported from SolidWorks CAD model and the parameters of the model is corrected with the aid of parametric system identification on data collected from the real system, as explained in Section 3.1. In the third section, simulation model construction is explained on the SimMechanics blocksets. Mechanical bodies belonging to each of the gimbals of the platform, friction model, motor and driver dynamics, the 6-DOF motion simulator (Stewart platform) which gives the base motion are presented in detail. To summarize, simulation model is explained through the parts, which are mechanical bodies, friction, motor and driver dynamics, 6-DOF motion simulator (Stewart Platform), and sensor noise and delay.

4.1 Mechanical Bodies

In this simulation work, the SimMechanics model is imported from the real mechanical CAD model composed in SolidWorks environment. The SimMechanics model excluding frictions is shown in Figure 4.1. With the mechanism configuration block, the gravity is specified in the model. The world block specifies the inertial frame. With the transform blocks, frame transformations, explained in the Section 2.1 can be carried out. Using revolute joint blocks, we can establish the rotational relationships between two rigid bodies. Also, torque and motion inputs can be applied to the gimbals through revolute joint blocks, and the position, velocity, and acceleration measurement can be obtained in a similar manner. Inside each of the gimbal blocks, there exists a reference frame block, a solid block and transform blocks as shown in the Figure 4.2.

Each rigid body requires a reference frame, which are defined in Section 2.1. The solid block, in the Figure 4.3 includes mass, moments of inertia, products of inertia, center of mass information in addition to the shape information coming from the imported CAD model and the visual properties for the 3-D graphical simulation. Transform blocks perform the rigid transformation duty.

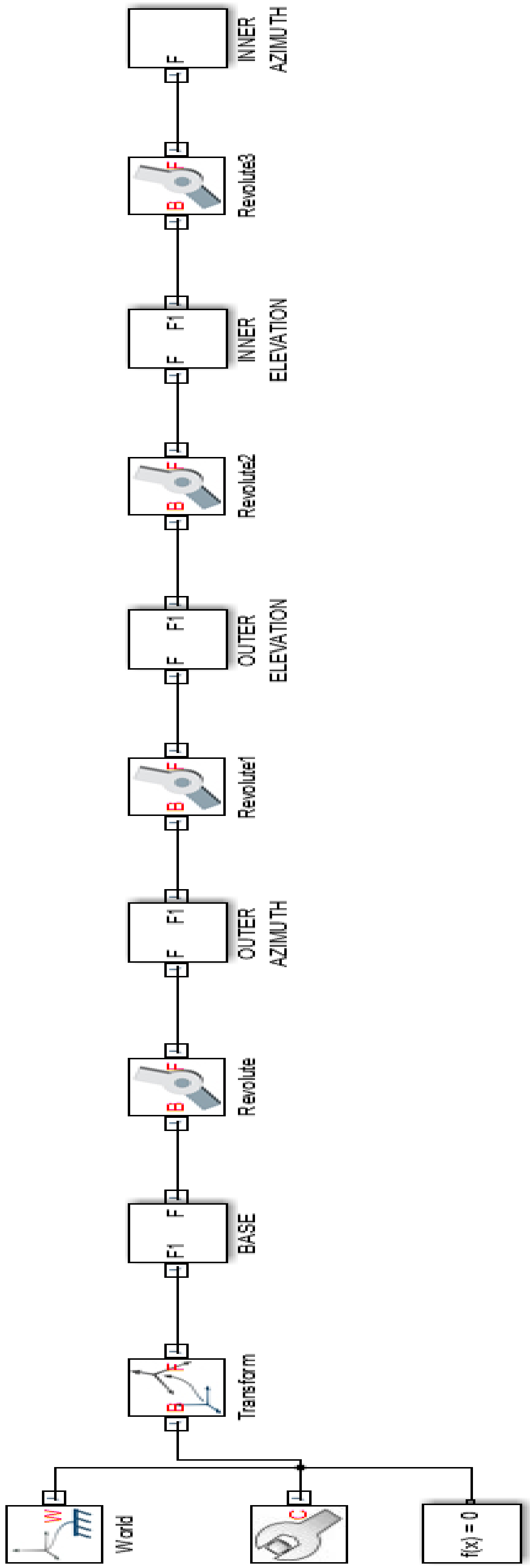
World
f(x) = 0
Transform
BASE
Revolute
OUTER
AZIMUTH
Revolute1
OUTER
ELEVATION
Revolute2
INNER
ELEVATION
Revolute3
INNER
AZIMUTH

Figure 4.1: Simulation Model of the 4-DOF platform on SimMechanics

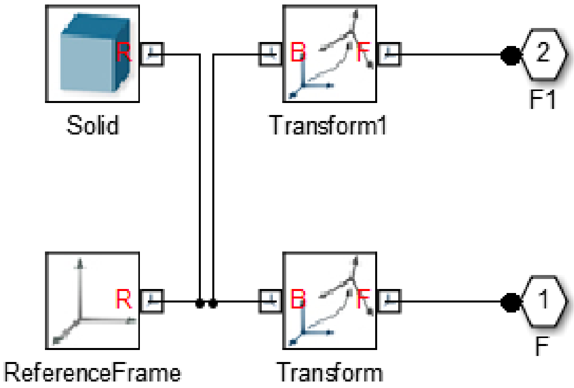

Figure 4.2: A Rigid Body Simulation Block

By running this simulation, we obtain a 3-D vision of the 4-DOF platform. The movements of all the axes can be observed physically by adjusting the opacity of the solid blocks. Moreover, with the utilization of scope and 'to workspace' blocks, we can obtain the measurements of velocity, position, angular acceleration and other desired measurements.

4.2 Friction

The Karnopp friction model, which is explained in Section 2.3, is implemented on Simulink as in Figure 4.3.

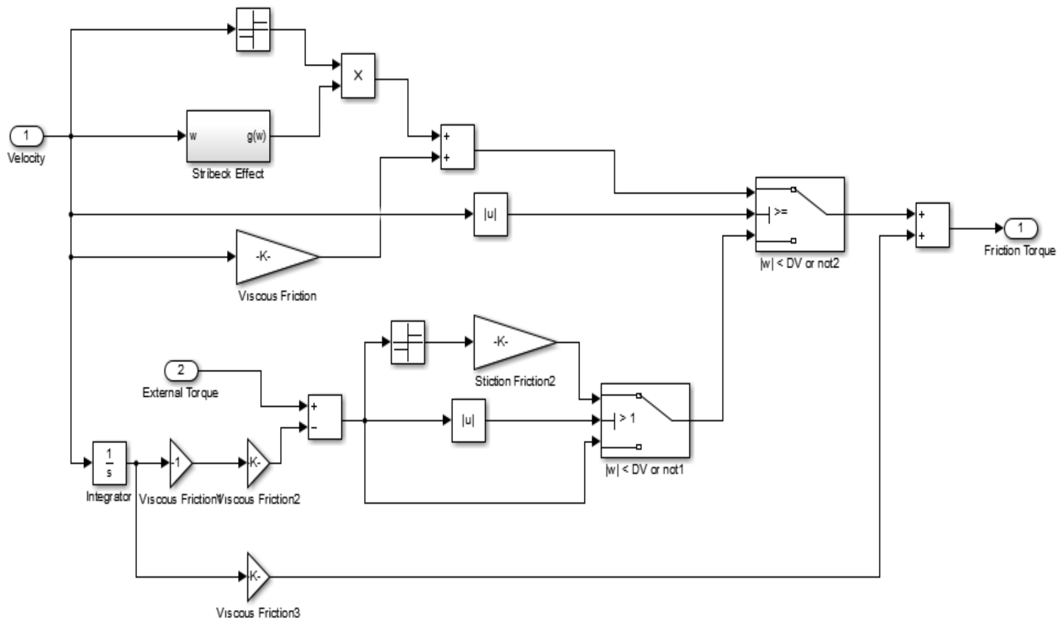

Figure 4.3: Karnopp Friction Simulation Model

Friction exists between gimbal base and the outer azimuth, the outer azimuth and the outer elevation, the outer elevation and the inner elevation, the inner elevation and the inner azimuth gimbal bearings. The Karnopp friction model is inserted into the SimMechanics model through the revolute joint blocks, as shown in the Figure 4.4. Revolute joint blocks can be configured to have torque inputs and velocity outputs. By using the velocity output of the revolute joint block, the velocity of the gimbal can be used as the velocity input of the friction model. The friction torque output of the Karnopp friction block is inserted into the simulation by subtracting it from the torque input of the gimbal.

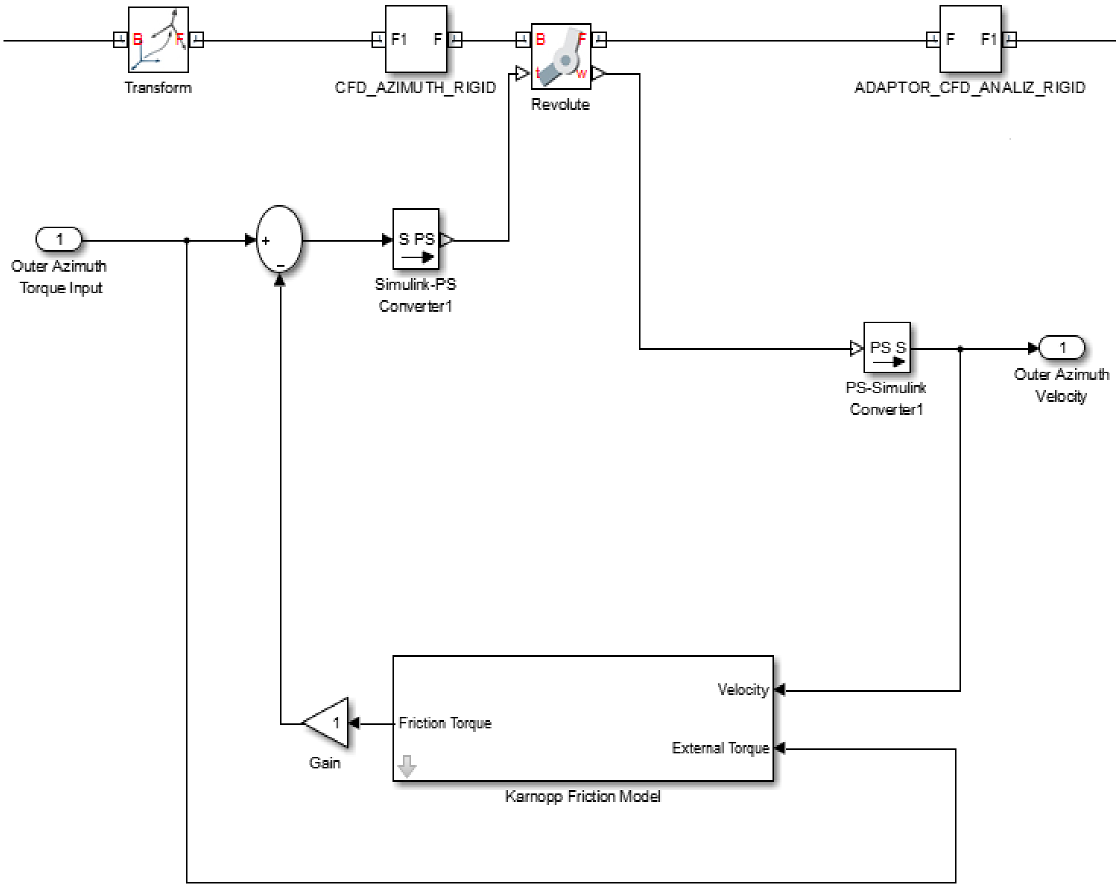

Figure 4.4: Friction Model Inserted into the Simulation Model

Friction affects the stabilization in a negative manner. Therefore it requires to be eliminated through several friction compensation methods.

4.3 6-DOF Motion Simulator

Figure 4.5: A Real Stewart Platform [21]

Stewart platform has an important role on the system since it has the capability to physically simulate different kinds of motion and disturbances on the gimbal base. Based on the disturbances coming from the Stewart platform, one can test the disturbance rejection and target tracking performance of any designed control algorithm. Stewart platform has a shape as in the Figure 4.5. The size of it can be redefined on MATLAB SimMechanics according to the requirements. With the use of Stewart platform, the 3 rotational degrees of freedom, ψ, θ and φ which are explained in Section 2.1, can be created besides 3 translational degrees of freedom.

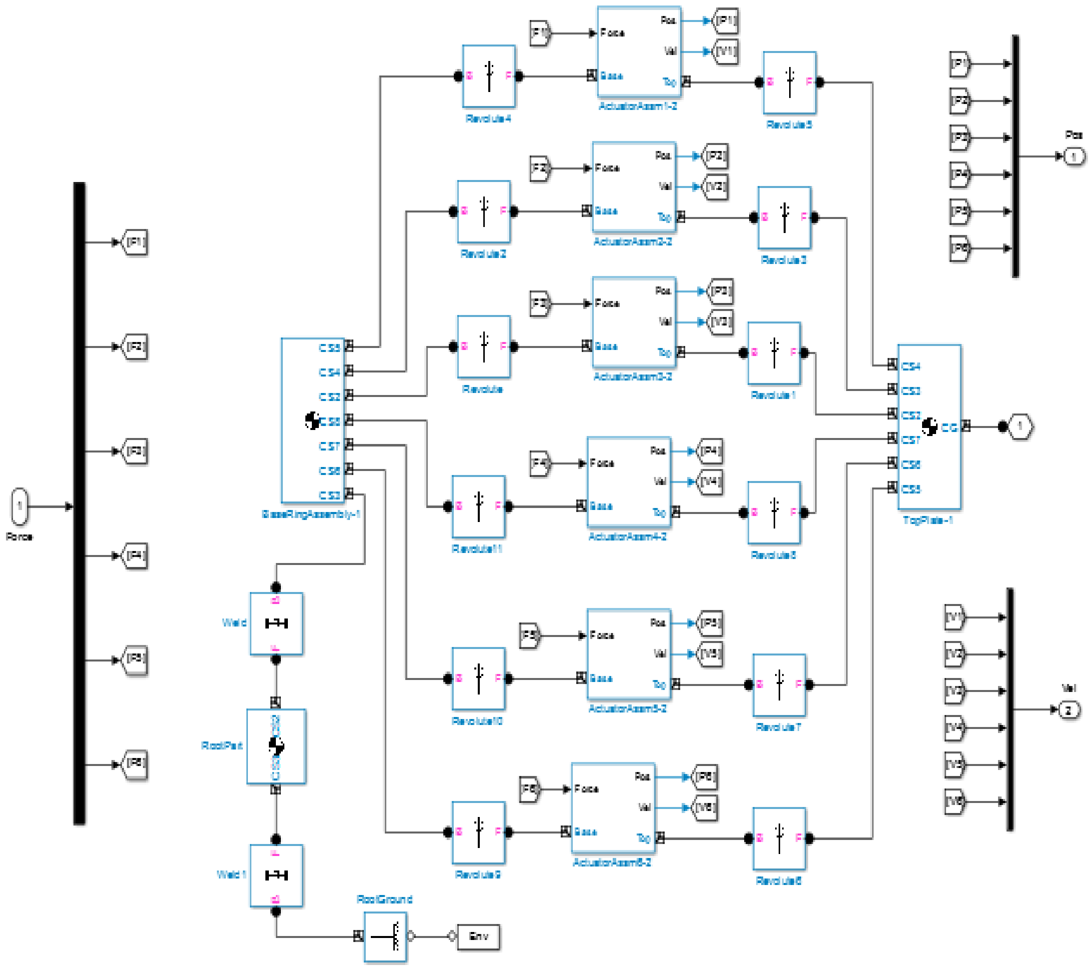

Figure 4.6: Simulation Blocks for the Stewart Platform

MATLAB SimMechanics model of Stewart platform is shown in Figure 4.6. Body blocks are defined for each 6 legs of the platform and upper and lower plates. Each leg is connected to the upper and lower plates through revolute joint blocks, which provide each body a freedom to move with respect to each other. Force input is applied to each of the legs and position and velocity of each leg can be obtained as an output. A predefined leg trajectory can be given to the simulation model as an input and the Stewart platform can make the desired movements via a PID controller.

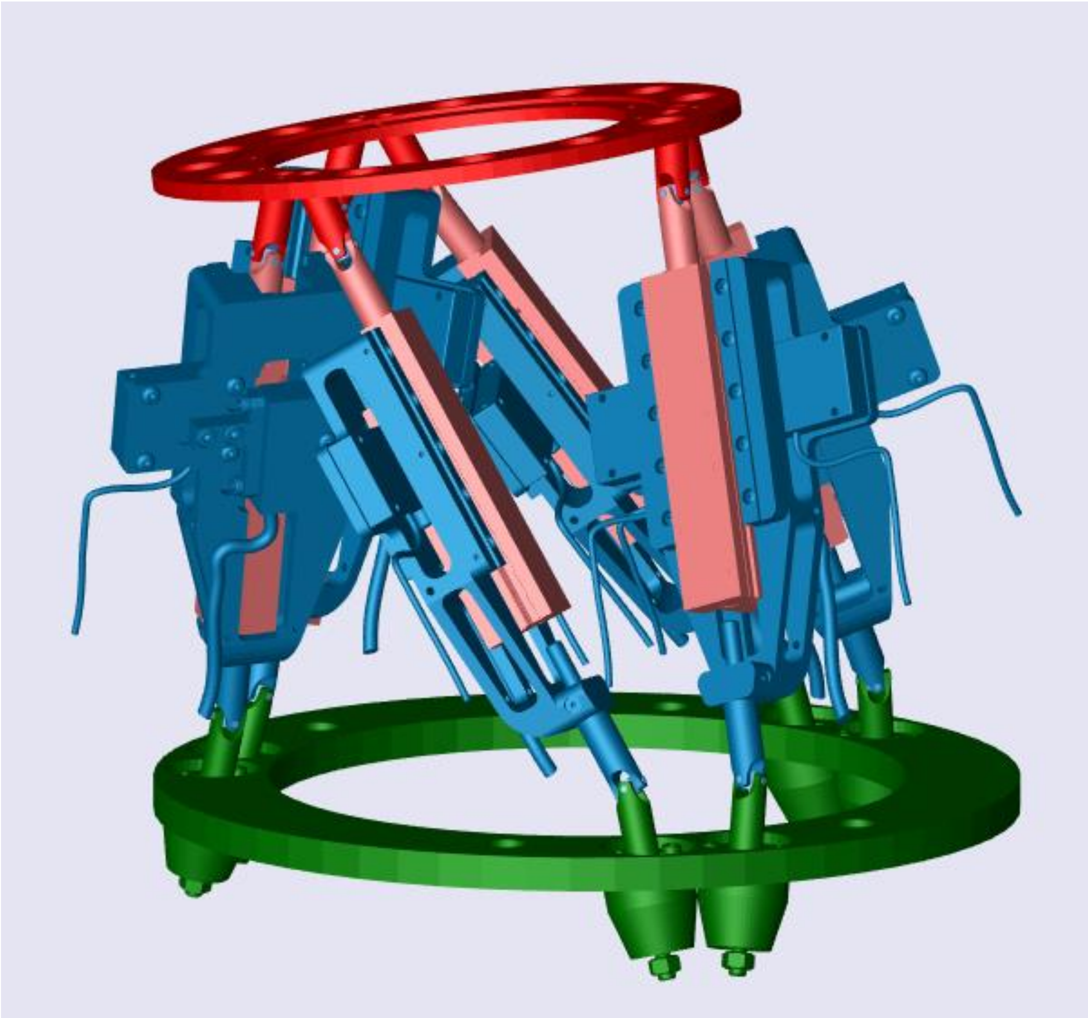

Figure 4.7: 3-D Simulation View of Stewart Platform

The gimbal base of the simulation model presented in Section 4.1 is connected to the top plate of the Stewart platform in SimMechanics. Therefore, gimbal base motion and disturbances can be simulated through this model. The controller and leg trajectory blocks of the Stewart platform model are shown in Figure 4.8. PID controller is utilized as the controller of the Stewart platform motion. Leg trajectory can be adjusted in positional and angular terms.

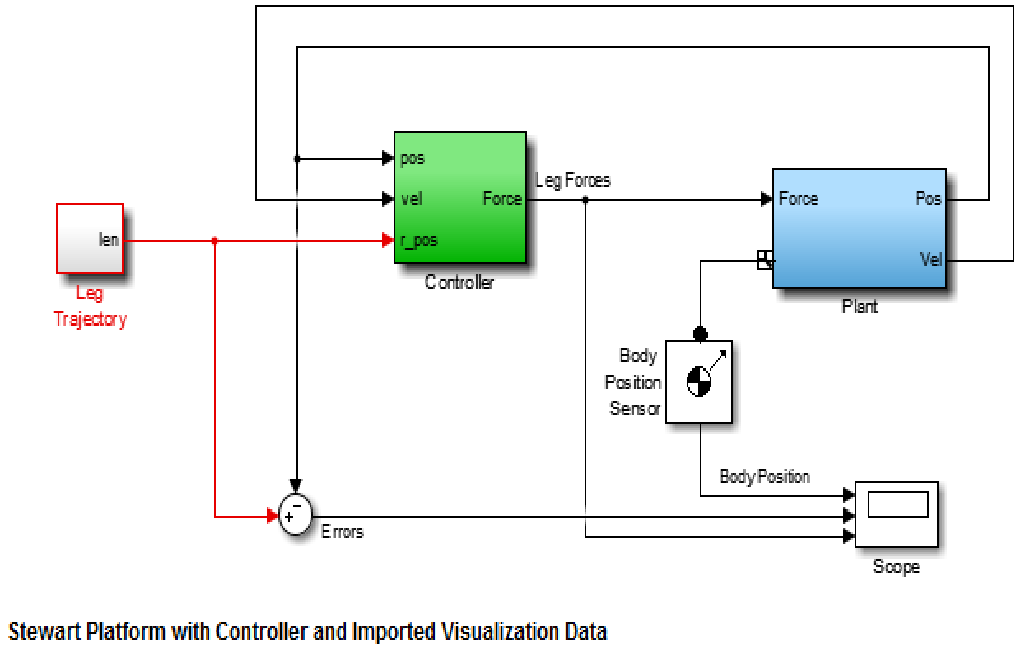

Figure 4.8: The Controller and Leg Trajectory Blocks of Stewart Platform

The 3-D simulation model of the 4-DOF gimbal placed on the Stewart platform is shown in Figure 4.9.

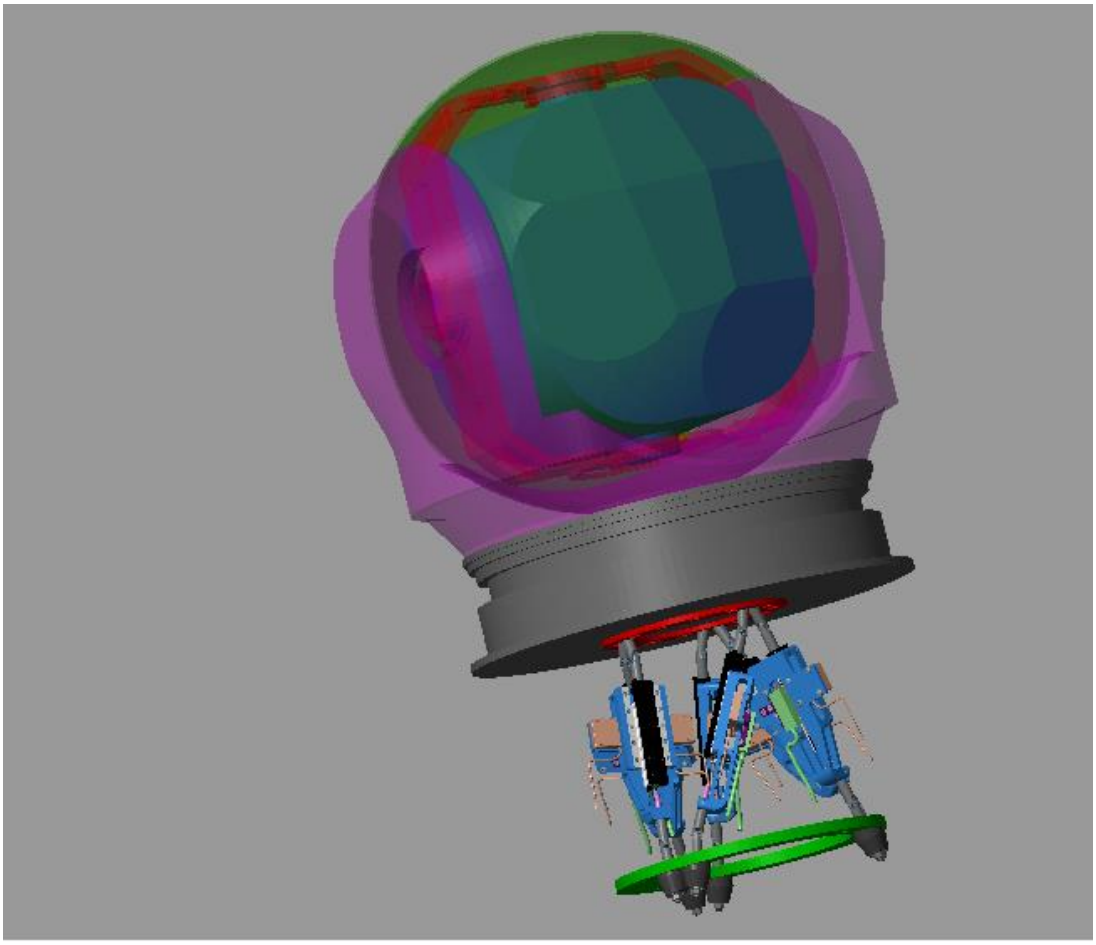

Figure 4.9: 4-DOF Platform Placed on the Stewart Platform

Since the Stewart Platform is imported from its CAD model (on Solidworks), the sizes cannot be changed in the 3-D picture. However, the mass, moments of inertia, products of inertia, leg lengths can be changed in MATLAB.

CHAPTER 5

STABILIZATION AND CONTROL OF THE TRACKING SYSTEM

5.1 Introduction

In this chapter, the controllers for the target tracking and stabilization purposes are investigated. Theory and implementations of the PID (Proportional, Integral and Derivative) Controller and the Sliding Mode Controller are explained. Disturbance rejection performances of these controllers are compared and evaluated. As explained in the Chapter 2, there are 4 gimbal axes and therefore, 4 actuators to be controlled. These gimbal axes will compensate the yaw and pitch disturbances coming from the Stewart platform, on which the 4-DOF platform is placed. However, the roll disturbances coming from the Stewart platform are not compensated since there is no actuator in roll axes on the 4-DOF platform. This situation does not constitute a handicap for the target-tracking system since the roll disturbances does not cause the target which is being tracked to escape out of the center of the image obtained from the camera. The cross-couplings between the gimbal axes are analyzed in [39]. In this study, without calculating the cross couplings, the stabilization is evaluated.

In accomplishing the stabilization task, the most important disturbance source is the friction. The controller performances can be evaluated according to friction compensation performances. Sensor noise also causes performance degrading in stabilization, but it can be corrected using a Kalman filter, which is explained in Section 2.4.

5.2 PID Control

In this section, for each gimbal axis, continuous time PID controllers are tuned with the aim of achieving the desired transient response, stability and robustness conditions. The desired conditions for PID control are: settling time is less than or equal to 0.1 sec for 5% settling limit and maximum overshoot for step response should be below 10% [22]. The PID controller is used for position control on the 4-DOF gimbal system. The PID controller has the transfer function in (5.1).

$$G_c(s)= K_p+ K_d s+ \frac{K_i}{s} \tag{5.1}$$

A continuous-time PID controller is tuned for the system, since a discrete-time PID controller can be converted into a continuous-time one by using a zero-order-hold (ZOH). Then, the PID tuner of the MATLAB is utilized ([23]) in order to compare whether the manual tuning produces sufficiently good responses as manual tuning and the sliding mode controller.

5.2.1 Manually Tuned PID Control

The manually tuned PID parameters tuned for each axis is given in Table 5.1.

Table 5.1: PID Position Controller Parameters Tuned Manually

Axis	K_p	K_i	K_d
Outer Azimuth	25	30	15
Outer Elevation	30	20	5
Inner Elevation	70	50	15
Inner Azimuth	50	40	15

The step responses to 0.5 rad step input belonging to each axis are given in Figures 5.1, 5.2, 5.3, and 5.4. The step responses to 0.3 rad step input belonging to each axis are given in Figures 5.5, 5.6, 5.7, and 5.8.

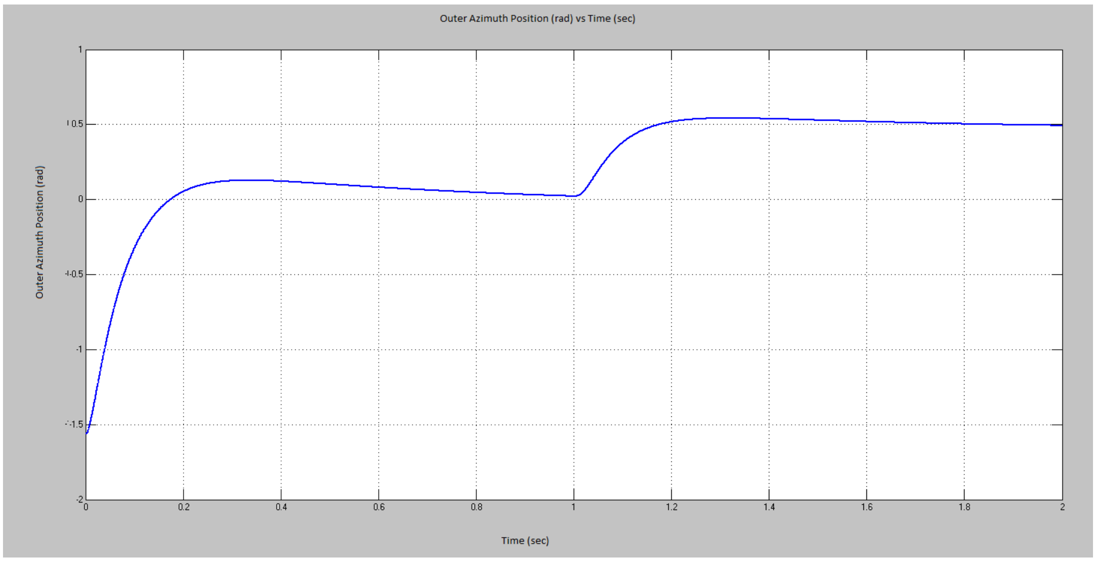

Figure 5.1: Outer Azimuth Step Response with PID Controller to 0.5 rad Step Input

The step response of the outer azimuth axis to the PID controller, which can be seen from Figure 5.1, has a maximum overshoot of 9% and settling time about 0.8 sec. It has an offset error.

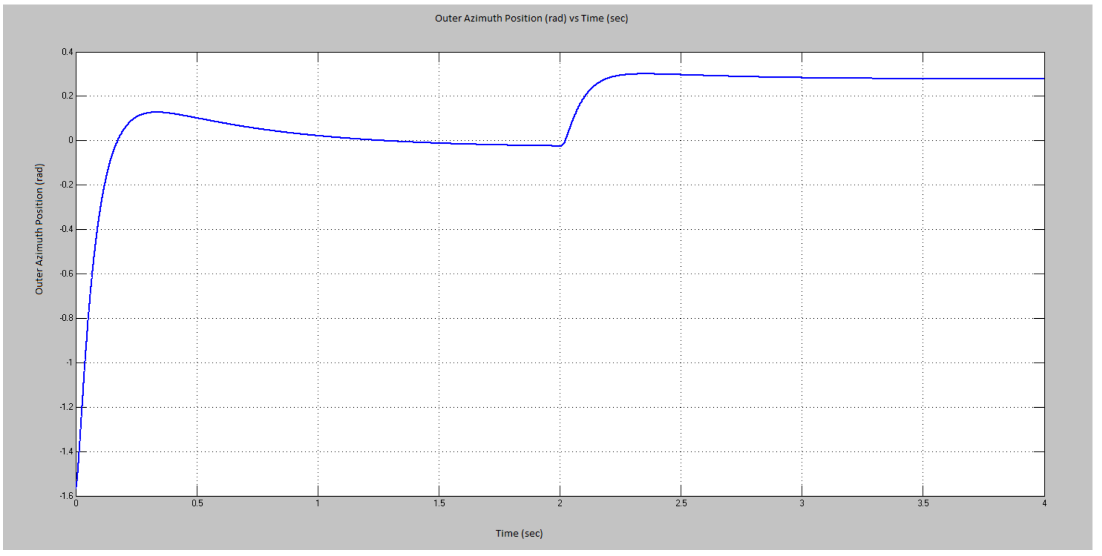

Figure 5.2: Outer Azimuth Step Response with PID Controller to 0.3 rad Step Input

The step response of the outer azimuth axis to the PID controller, which can be seen from Figure 5.2, has a maximum overshoot of 8% and settling time about 0.7 sec. The response has an offset error about 2%.

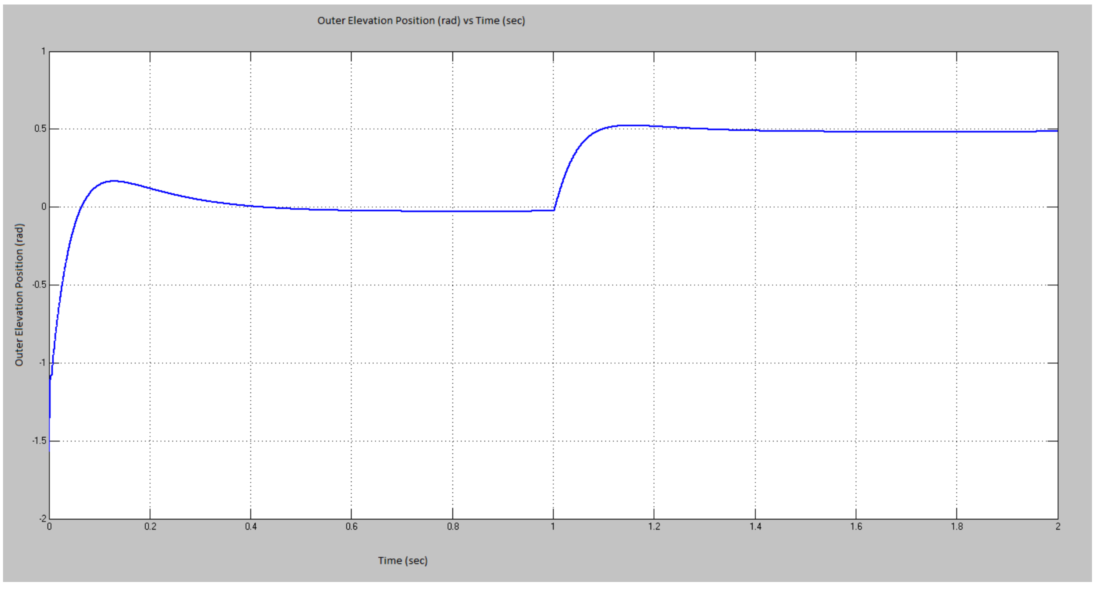

Figure 5.3: Outer Elevation Step Response with PID Controller to 0.5 rad Step Input

The step response of the outer elevation axis to the PID controller, which can be seen from Figure 5.3, has a maximum overshoot of 6% and settling time about 0.32 sec. It has an offset error about 1%.

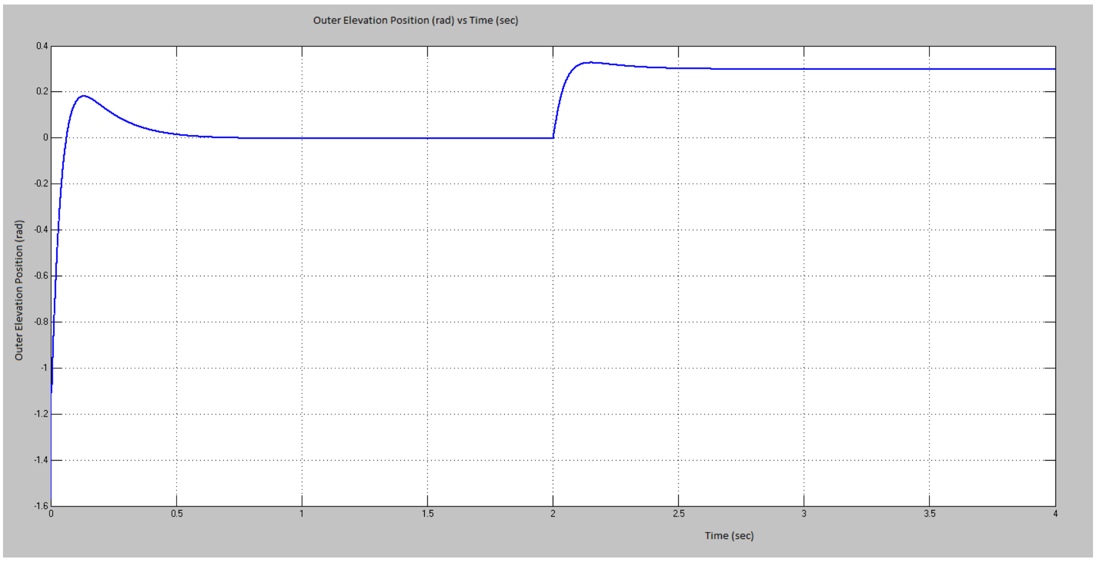

Figure 5.4: Outer Elevation Step Response with PID Controller to 0.3 rad Step Input

The step response of the outer elevation axis to the PID controller, which can be seen from Figure 5.4, has a maximum overshoot of 5% and settling time about 0.3 sec. The response has an offset error about 1%.

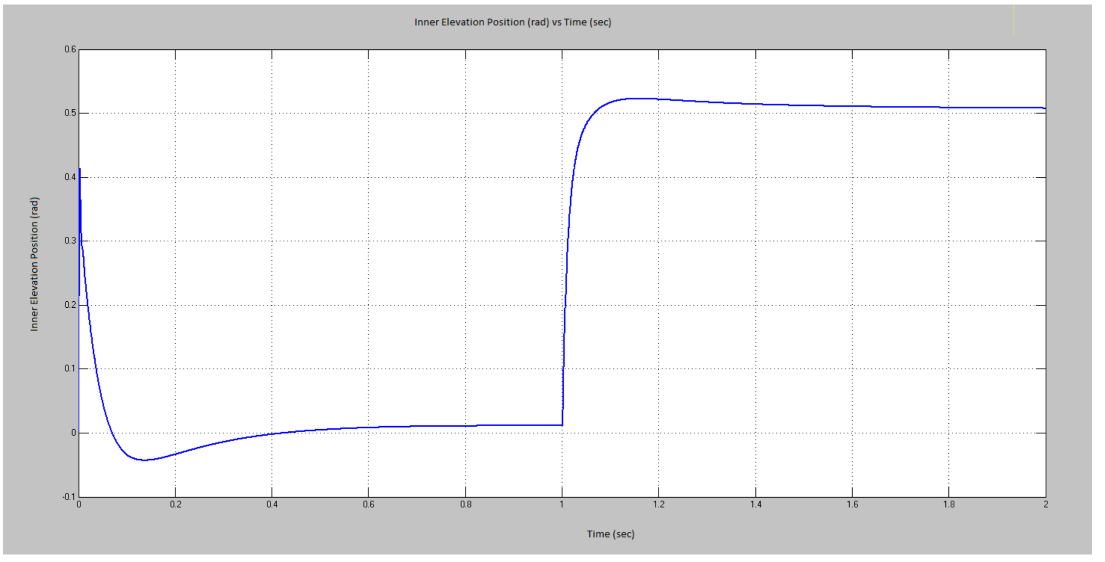

Figure 5.5: Inner Elevation Step Response with PID Controller to 0.5 rad Step Input

The step response of the inner elevation axis to the PID controller, which can be seen from Figure 5.5, has a maximum overshoot of 5% and settling time about 0.4 sec. The response has an offset error about 1%.

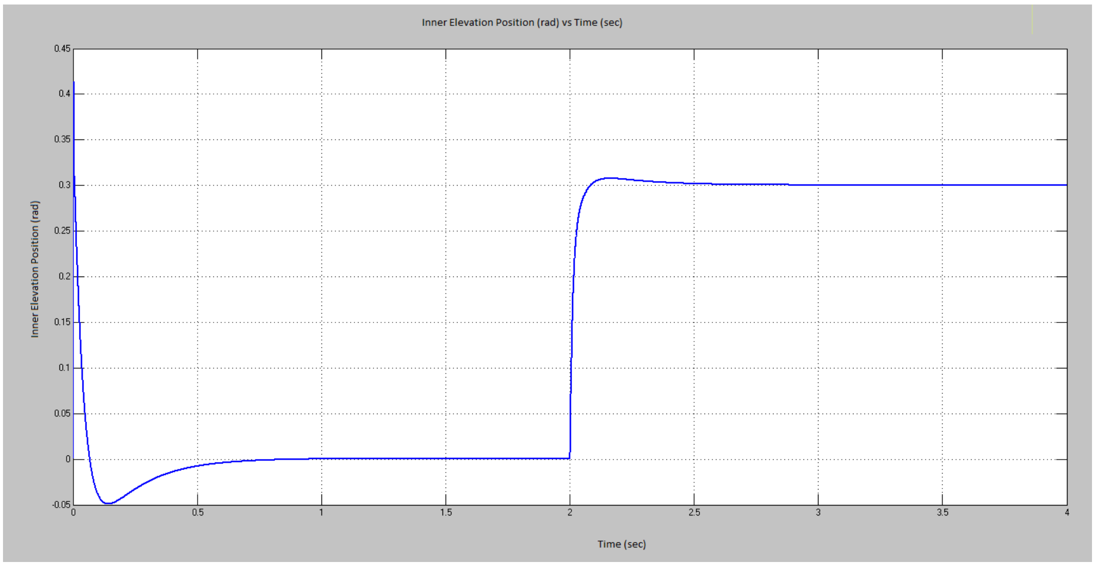

Figure 5.6: Inner Elevation Step Response with PID Controller to 0.3 rad Step Input

The step response of the inner elevation axis to the PID controller, which can be seen from Figure 5.6, has a maximum overshoot of 5% and settling time about 0.35 sec. The response has an offset error about 1.5%.

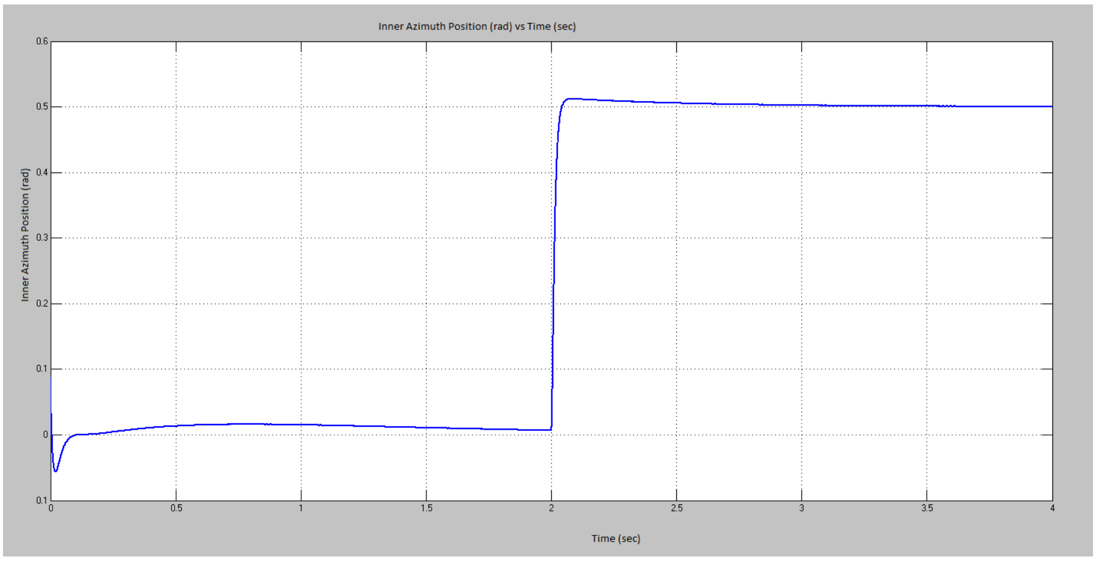

Figure 5.7: Inner Azimuth Step Response with PID Controller to 0.5 rad Step Input

The step response of the inner azimuth axis to the PID controller, which can be seen from Figure 5.7, has a maximum overshoot of 2% and settling time about 0.2 sec. The response has an offset error about 8%.

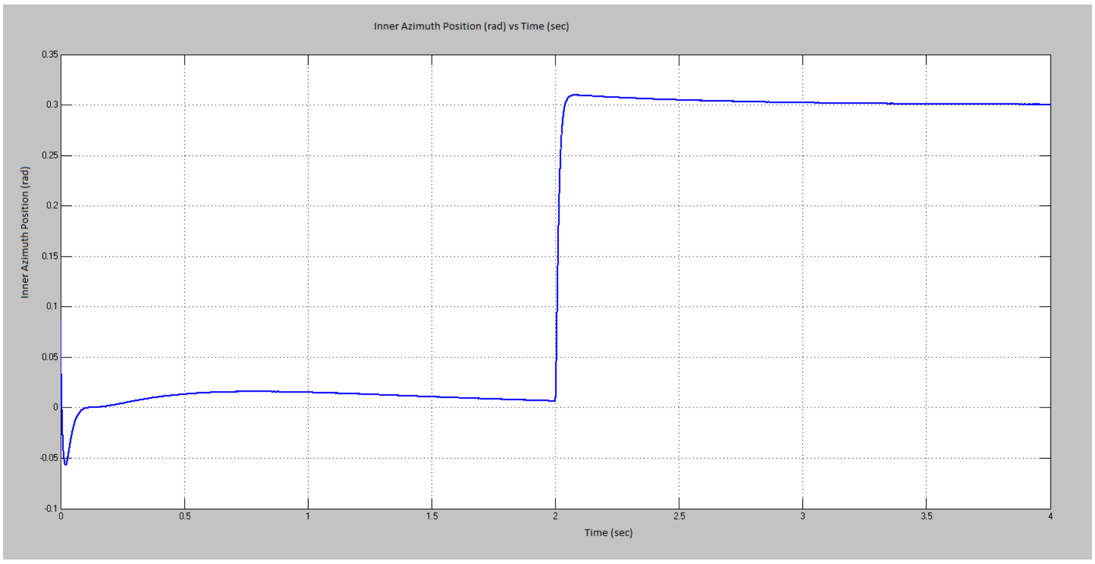

Figure 5.8: Inner Azimuth Step Response with PID Controller to 0.3 rad Step Input

The step response of the inner azimuth axis to the PID controller, which can be seen from Figure 5.8, has a maximum overshoot of 3% and settling time about 0.2 sec. The response has an offset error about 7%.

The bigger step responses are chosen with magnitude 0.5 since the unit is rad. 0.5 rad is about 55 degrees step. In the SimMechanics model of the 4-DOF platform, the initial conditions are not adjusted to 0 rad. Therefore, the step responses in Figure 5.1, Figure 5.2, Figure 5.3,Figure 5.4, Figure 5.5, Figure 5.6, Figure 5.7 and Figure 5.8 have some overshoots while coming to zero radian position from non-zero initial condition.

5.2.2 Automatically Tuned PID Control

The automatically tuned PID parameters tuned for each axis is given in Table 5.2.

Table 5.2: PID Position Controller Parameters Tuned by MATLAB

Axis	K_p	K_i	K_d
Outer Azimuth	490428.067465887	11927143.6111644	4480.58950278374
Outer Elevation	211178.45946078	18117068.3360075	222.243172194709
Inner Elevation	10539.3154589856	79531.1018858048	141.236461941122
Inner Azimuth	60504.5509840086	2171141.27078009	374.635538705721

The step responses belonging to each axis are given in Figures 5.9, 5.10, 5.11, 5.12, 5.13, 5.14, 5.15, 5.16 .

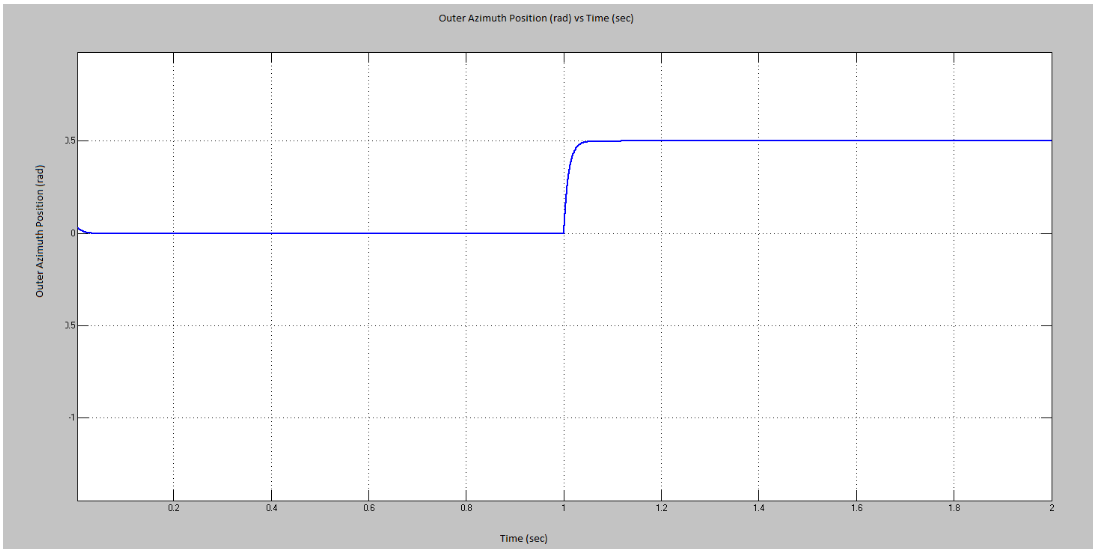

Figure 5.9: Outer Azimuth Step Response with Automatically Tuned PID Controller to 0.5 rad Step Input

The step response of the outer azimuth axis to the automatically tuned PID controller, which can be seen from Figure 5.9, has a maximum overshoot of 0% and settling time about 0.038 sec. The response has no offset error.

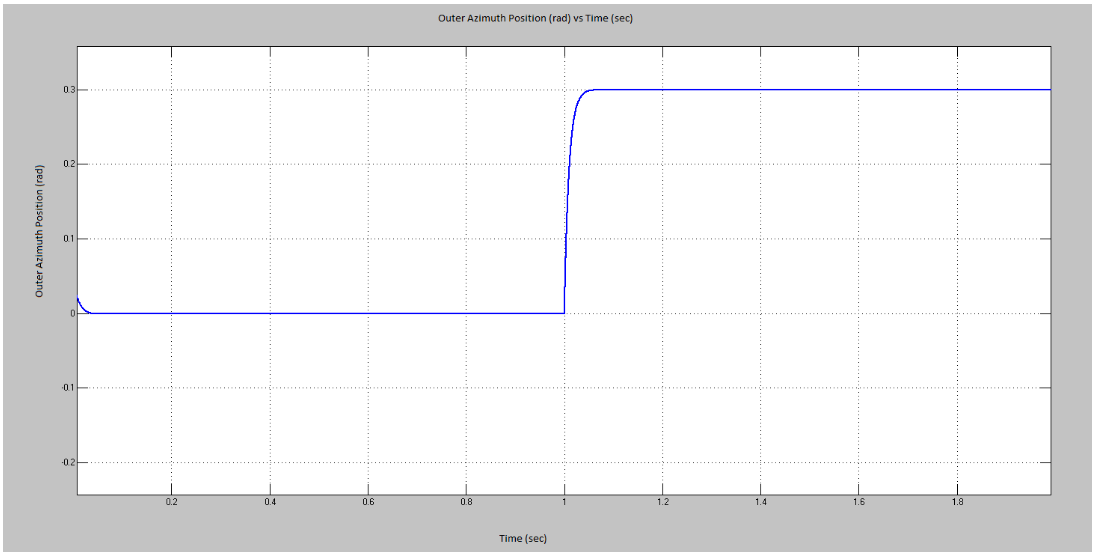

Figure 5.10: Outer Azimuth Step Response with Automatically Tuned PID Controller to 0.3 rad Step Input

The step response of the outer azimuth axis to the automatically tuned PID controller, which can be seen from Figure 5.10, has a maximum overshoot of 0% and settling time about 0.035 sec. The response has no offset error.

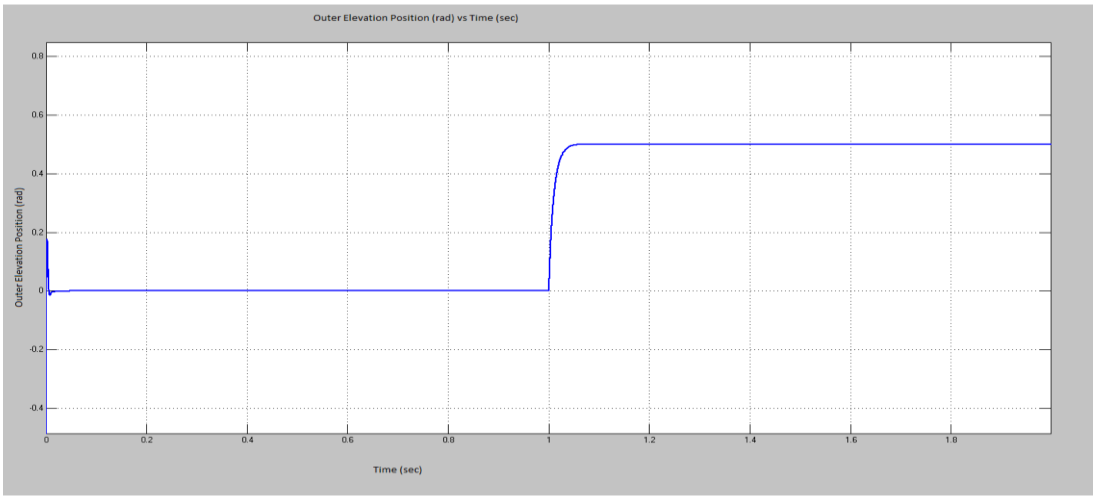

Figure 5.11: Outer Elevation Step Response with Automatically Tuned PID Controller to 0.5 rad Step Input

The step response of the outer elevation axis to the automatically tuned PID controller, which can be seen from Figure 5.11, has a maximum overshoot of 0% and settling time about 0.038 sec. The response has no offset error.

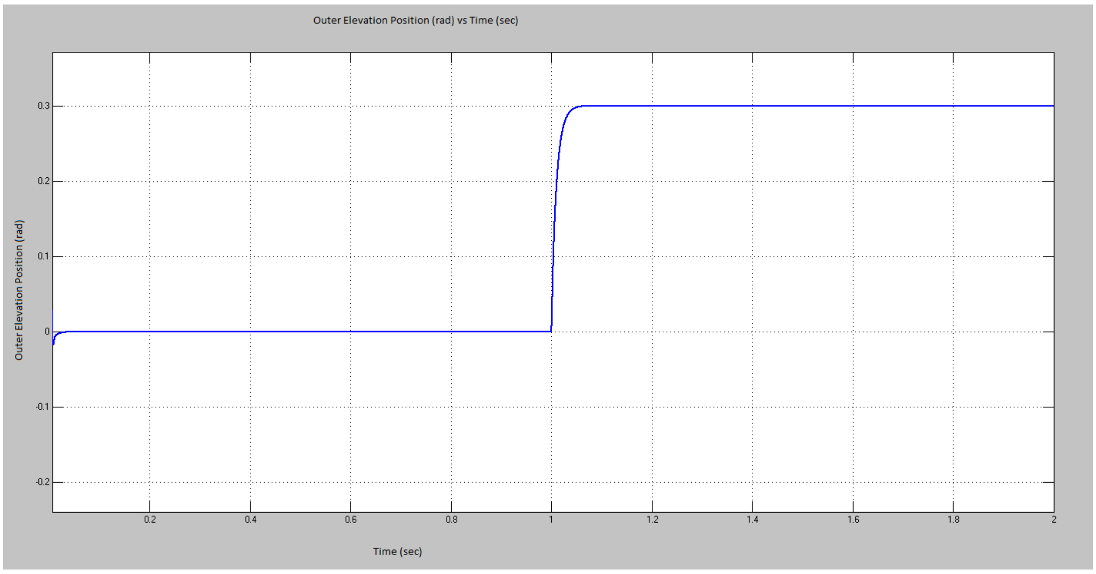

Figure 5.12: Outer Elevation Step Response with Automatically Tuned PID Controller to 0.3 rad Step Input

The step response of the outer elevation axis to the automatically tuned PID controller, which can be seen from Figure 5.12, has a maximum overshoot of 0% and settling time about 0.034 sec. The response has no offset error.

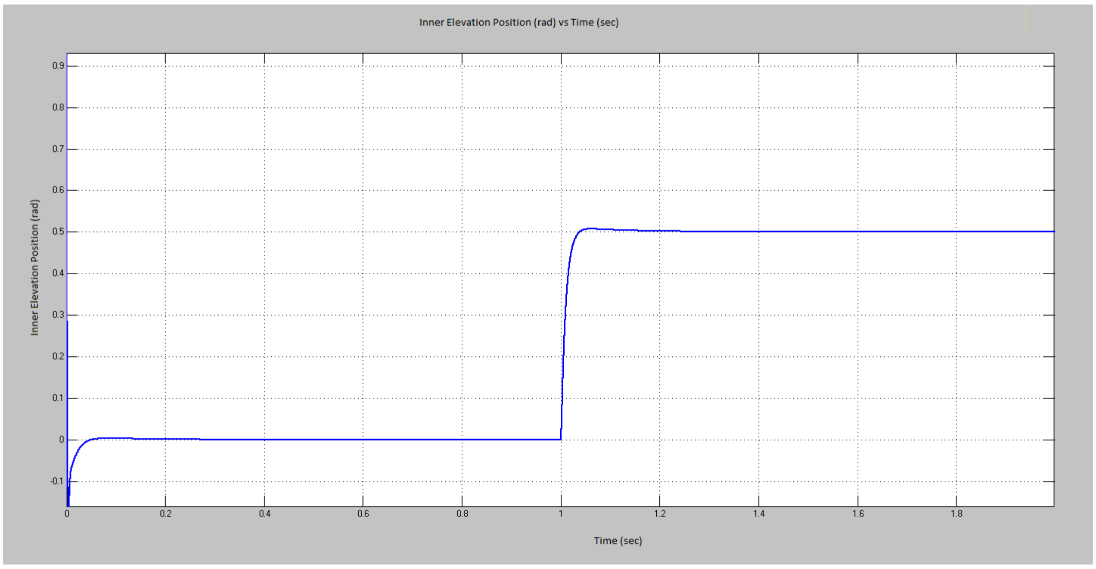

Figure 5.13: Inner Elevation Step Response with Automatically Tuned PID Controller to 0.5 rad Step Input

The step response of the outer elevation axis to the automatically tuned PID controller, which can be seen from Figure 5.13, has a maximum overshoot of 1.6% and settling time about 0.034 sec. The response has no offset error.

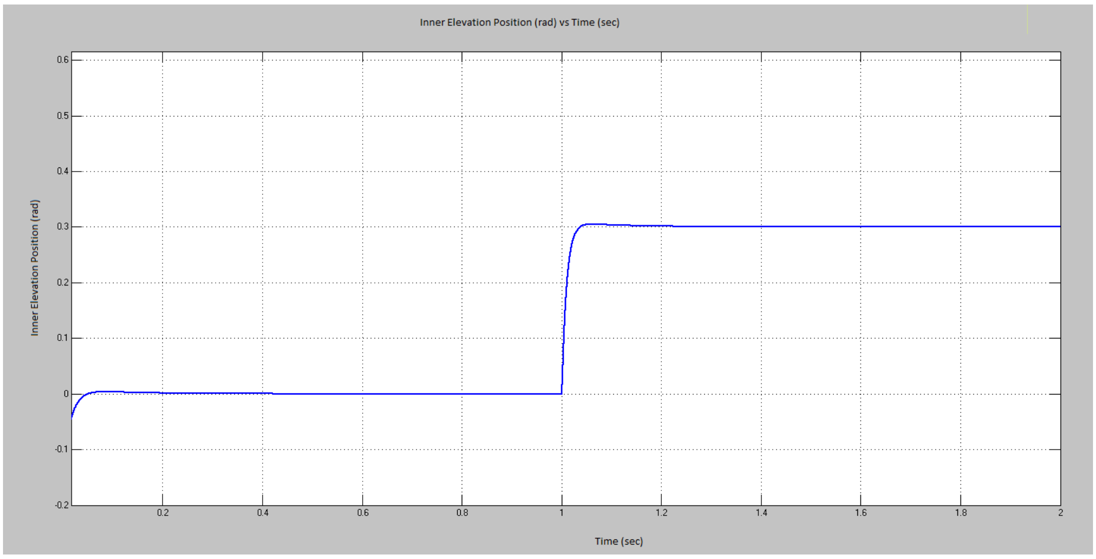

Figure 5.14: Inner Elevation Step Response with Automatically Tuned PID Controller to 0.3 rad Step Input

The step response of the inner elevation axis to the automatically tuned PID controller, which can be seen from Figure 5.14, has a maximum overshoot of 1,6% and settling time about 0.032 sec. The response has no offset error.

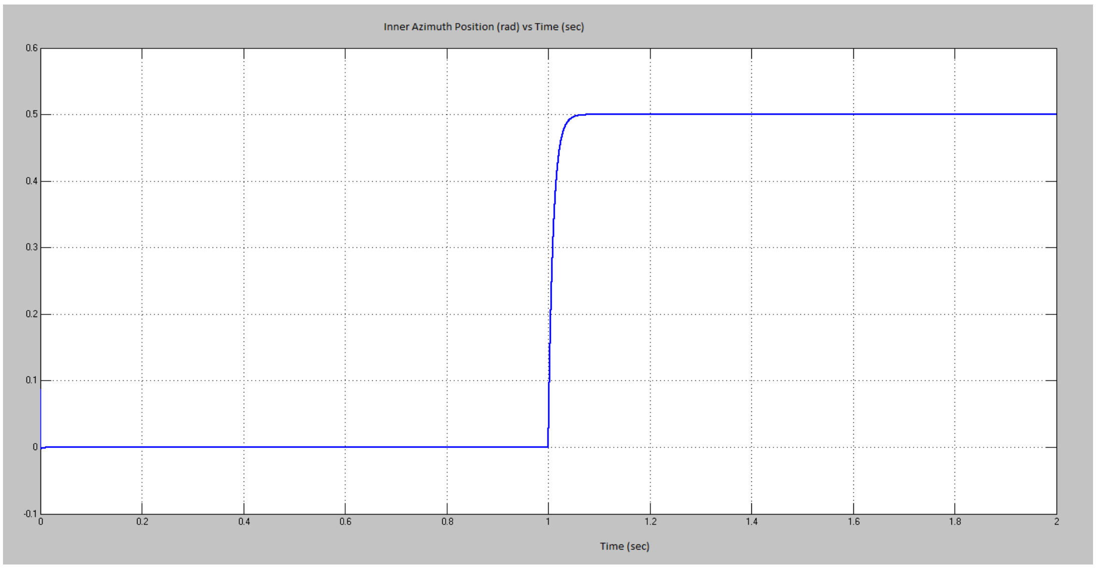

Figure 5.15: Inner Azimuth Step Response with Automatically Tuned PID Controller to 0.5 rad Step Input

The step response of the inner azimuth axis to the automatically tuned PID controller, which can be seen from Figure 5.15, has a maximum overshoot of 0% and settling time about 0.039 sec. The response has no offset error.

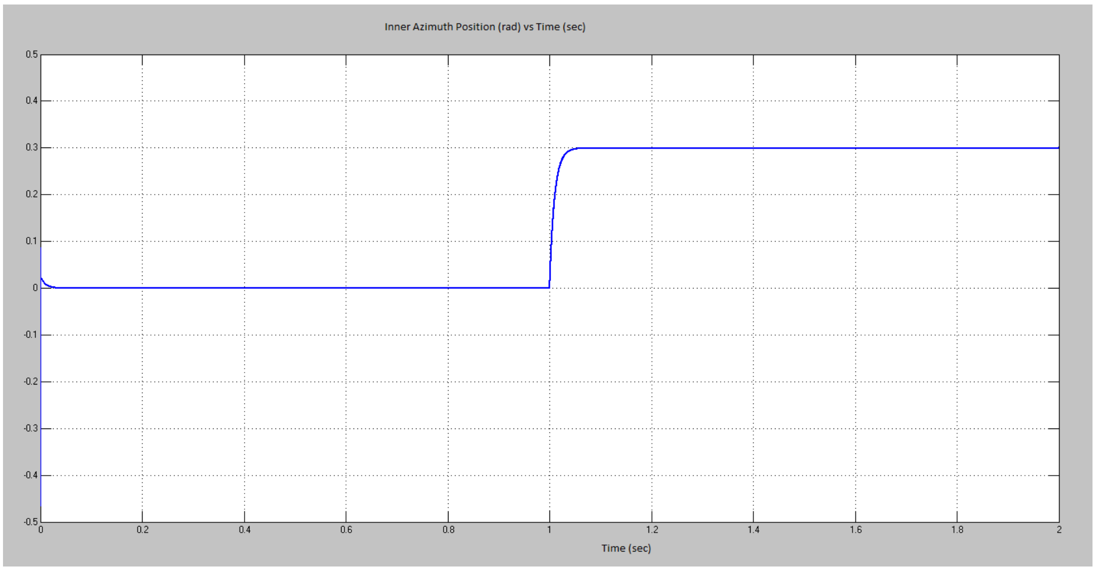

Figure 5.16: Inner Azimuth Step Response with Automatically Tuned PID Controller to 0.3 rad Step Input

The step response of the inner azimuth axis to the automatically tuned PID controller, which can be seen from Figure 5.16, has a maximum overshoot of 0% and settling time about 0.036 sec. The response has no offset error.

The comparison of the step responses of the manually tuned PID and automatically tuned PID controllers are given in Table 5.3.

Table 5.3: Comparison of the Step Responses of Manually and Automatically Tuned PID Controllers

	PID Controller			Automatically Tuned PID Controller		
	Settling Time (sec)	Overshoot	Offset Error	Settling Time (sec)	Overshoot	Offset Error
Outer Azimuth 0.5 rad step	0.8	9%	Yes	0.038	0%	No
Outer Azimuth 0.3 rad step	0.7	8%	Yes	0.035	0%	No
Outer Elevation 0.5 rad step	0.32	6%	Yes	0.038	0%	No
Outer Elevation 0.3 rad step	0.3	5%	Yes	0.034	0%	No
Inner Elevation 0.5 rad step	0.4	5%	Yes	0.034	1.6%	No
Inner Elevation 0.3 rad step	0.35	5%	Yes	0.032	1.6%	No
Inner Azimuth 0.5 rad step	0.2	2%	Yes	0.039	0%	No
Inner Azimuth 0.3 rad step	0.2	2%	Yes	0.039	0%	No

In order to compare the performances of the PID controllers on small and big disturbances, 0.5 rad and 0.3 rad step inputs are given to the system. The overshoots are nearly the same, whereas the settling times are slightly smaller for the smaller step sizes. This result is reasonable since settling of the system must be quicker for smaller commands.

5.3 Sliding Mode Control

Sliding Mode Control (SMC) is a robust control method which compensates the changes in the plant and external disturbances without change in the performance [22]. A sliding mode control design consists of 2 steps. The first step is to choose the switching surface which is in the state space on which the closed loop system motion shows the desired behavior regardless of plant uncertainties and disturbances. The second step is to design a control function which makes the selected surface attractive [25], [26]. As regards to the structure of the controller, it consists of a nominal (switching) part that provides main control action and an additional term for dealing with the disturbances and unmodeled dynamics [22], [30]. The control input coming from the SMC has the switching and the equivalent parts as in (5.2).

$$u_{SM} = u_{sw} + u_{eq} \tag{5.2}$$

The switching part of the controller, u_{sw}, compensates the deviations from the sliding surface. The equivalent part of the controller, u_{eq}, makes the derivative part of the sliding mode controller equivalent to zero in order to stay on the sliding surface.

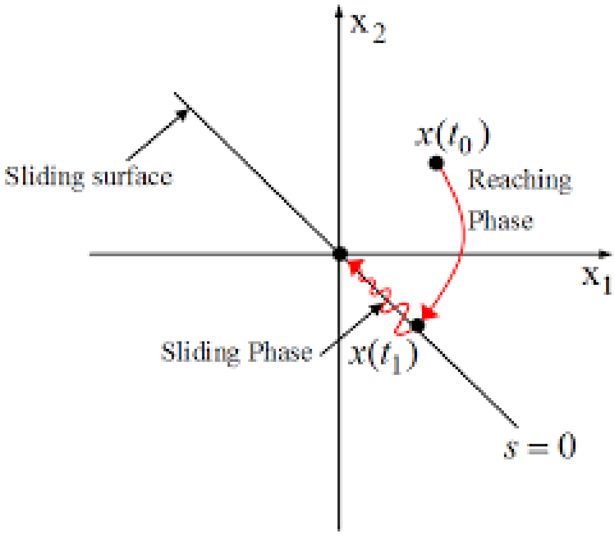

Figure 5.17: Sliding Surface and the State Trajectory [27]

As in Figure 5.17, the sliding mode control has 2 phases. The non-zero initial condition reaches the sliding surface during the reaching phase. In the sliding phase, the trajectory which has reached the sliding surface, stays there and evolves according to the dynamics specified by the sliding surface [25], [28], [29].

5.3.1 Sliding Surface Design

The sliding surface $\sigma(\hat{x})$ is a function of tracking error $\hat{x} = (x_d - x)$, where x_d is the desired state. It is chosen in compliance with Lyapunov's Global Stability Theorem [31]. If a scalar function $V(\sigma)$ has continuous first order derivatives and it satisfies the following conditions

- $V(\sigma)$ is positive definite for all σ,
- $\dot{V}(\sigma)$ is negative definite for all σ,
- When $V(\sigma)$ goes to infinity, $\|\sigma\|$ should go to infinity.

Then the equilibrium at the origin of this function is globally asymptotically stable. [22]. The Lyapunov function satisfying these conditions is (5.3).

$$V(\sigma) = \frac{1}{2}\sigma^T \sigma \qquad (5.3)$$

$$\dot{V}(\sigma) = \sigma\dot{\sigma} < 0 \qquad (5.4)$$

The chosen sliding surface is in the form of (5.5)

$$\sigma(\hat{x}) = h^T(x_d - x) \qquad (5.5)$$

where x is the vector of the actual states and x_d is the vector of desired states, h is the right eigenvector (corresponds to zero eigenvalue) of the desired closed loop system matrix A. [21].

The sliding surfaces chosen for the 4 gimbal axes are shown in the equations (5.6), (5.7), (5.8) and (5.9).

$$\sigma_{OA} = \begin{bmatrix} 5000 \\ 100 \end{bmatrix} \left(\begin{bmatrix} \theta_d \\ \dot{\theta}_d \end{bmatrix} - \begin{bmatrix} \theta \\ \dot{\theta} \end{bmatrix} \right) \qquad (5.6)$$

$$\sigma_{OE} = \begin{bmatrix} 10000 \\ 10 \end{bmatrix} \left(\begin{bmatrix} \theta_d \\ \dot{\theta}_d \end{bmatrix} - \begin{bmatrix} \theta \\ \dot{\theta} \end{bmatrix} \right) \qquad (5.7)$$

$$\sigma_{IE} = \begin{bmatrix} 1000 \\ 10 \end{bmatrix} \left(\begin{bmatrix} \theta_d \\ \dot{\theta}_d \end{bmatrix} - \begin{bmatrix} \theta \\ \dot{\theta} \end{bmatrix} \right) \qquad (5.8)$$

$$\sigma_{IA} = \begin{bmatrix} 10000 \\ 100 \end{bmatrix} \left(\begin{bmatrix} \theta_d \\ \dot{\theta}_d \end{bmatrix} - \begin{bmatrix} \theta \\ \dot{\theta} \end{bmatrix} \right) \qquad (5.9)$$

5.3.2 Sliding Mode Controller Design

The control law is designed using a Lyapunov-based approach [32]. The dynamics of σ is derived in (5.10).

$$\dot{\sigma} = c\dot{e} + \ddot{e} = 0 \qquad (5.10)$$

where $e = (y_d - y)$ is the position error.

A system described in [32] is give in (5.11), (5.12), (5.13):

$$\dot{x}_1 = x_2 \tag{5.11}$$

$$\dot{x}_2 = \varphi(x_1, x_2) + b(x_1, x_2)U \tag{5.12}$$

$$y = x_1 \tag{5.13}$$

Then (5.10) becomes

$$\dot{\sigma} = \ddot{y} - \varphi + c\dot{e} - bU \tag{5.14}$$

The Lyapunov function becomes

$$\dot{V}(\sigma) = b^{-1}\sigma[\ddot{y} - \varphi + c\dot{e} - bU - 0.5b^{-1}\dot{b}\sigma] \tag{5.15}$$

In order for the Lyapunov function to be positive definite, the condition (5.16) must be satisfied.

$$\dot{V}(\sigma) = -\rho\,|\sigma| < 0 \tag{5.16}$$

The SMC law becomes

$$u_{SM} = u_{eq} + \rho \text{ sign}(\sigma) \tag{5.17}$$

where

$$u_{eq} = b^{-1}[\ddot{y} - \varphi + c\dot{e} - bU - 0.5b^{-1}\dot{b}\sigma] \tag{5.18}$$

where b is the feedback gain coming from robust Pole Placement Theory, [36]. In our case, the control inputs are

$$u_{SM,OA} = \text{sign}(\sigma) + \sigma \tag{5.19}$$

$$u_{SM,OE} = \text{sign}(\sigma) + 0.5\,\sigma + 0.0001(\ddot{\theta}_d - \ddot{\theta}) + (\dot{\theta}_d - \dot{\theta}) \tag{5.20}$$

$$u_{SM,IE} = \text{sign}(\sigma) + 0.5\,\sigma + 0.0001(\ddot{\theta}_d - \ddot{\theta}) + (\dot{\theta}_d - \dot{\theta}) \quad (5.21)$$

$$u_{SM,IA} = \text{sign}(\sigma) + \sigma \quad (5.22)$$

5.3.3 Chattering Phenomena

Large switching gains may improve robustness and stability. However, they can cause a phenomenon called as “chattering”. Although trajectories slide along the sliding surface theoretically, it is a high frequency switching in practice, due to inclusion of sign function in the switching term. When this phenomenon occurs, control input starts to oscillating around the zero sliding surface. The oscillating control input may result in unwanted and harmful tear, vibration, sound etc. [22], [30]. Hence the performance may degrade in time.

To solve the chattering problem, “soft switching” method is implemented. Other smooth functions around the switching zone are utilized in soft switching, instead of the sign function. In [37] and [38], sat function is utilized for soft switching. In this study, hyperbolic tangent function is chosen. Tangent function has the same asymptotes as the sign function. There is a continuous transition area around the zero value of the sliding surface. This area is known as “boundary layer”. By changing the boundary layer thickness parameter, φ, the thickness of the boundary layer can also be adjusted, as in [22]. In Figure 5.18, different sliding surfaces created using different switching functions are exhibited.

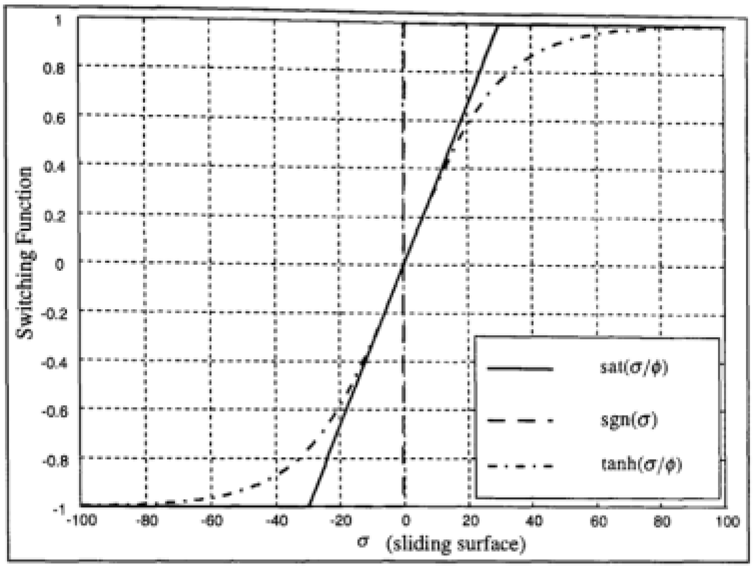

Figure 5.18: Switching Function vs. Sliding Surface [31]

The use of hyperbolic tangent function with boundary layer thickness parameter $\varphi = 10$ resulted in a significant decrease in chattering. Since the Karnopp friction model has a hysteresis loop, the chattering phenomena have caused numerical difficulties during simulations.

The step responses measure the controller performance. The SMC with soft switching step responses of 4 gimbals to a step with magnitude 0.5 rad is given in Figures 5.7, 5.8, 5.9 and 5.10.

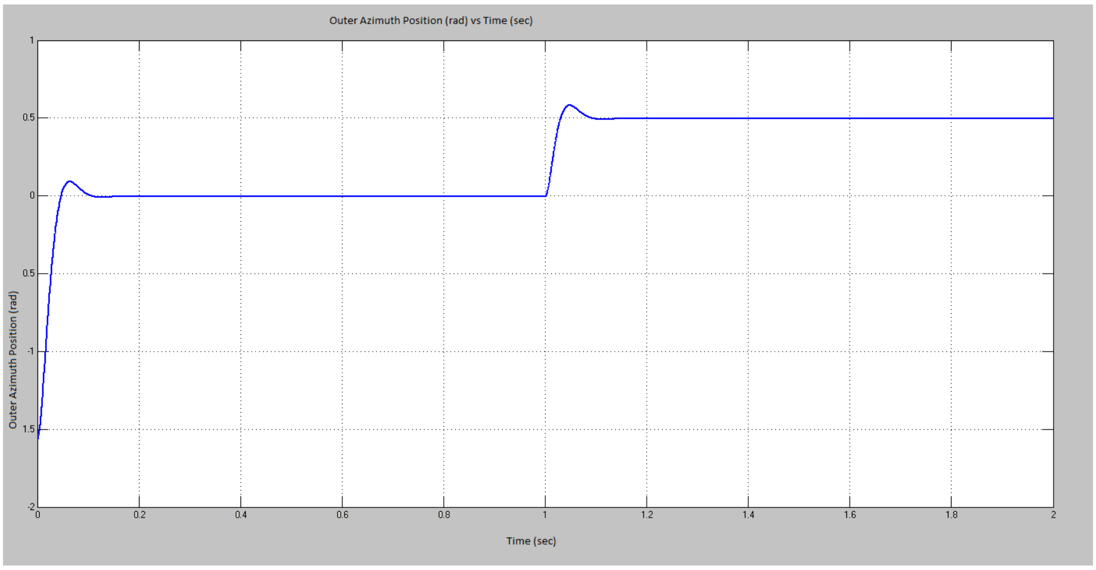

Figure 5.19: Outer Azimuth Position Step Response with SMC

The step response of the outer azimuth axis to the SMC, which can be seen from Figure 5.19, has a maximum overshoot of 5.7% and settling time about 0.05 sec. The response has no offset error.

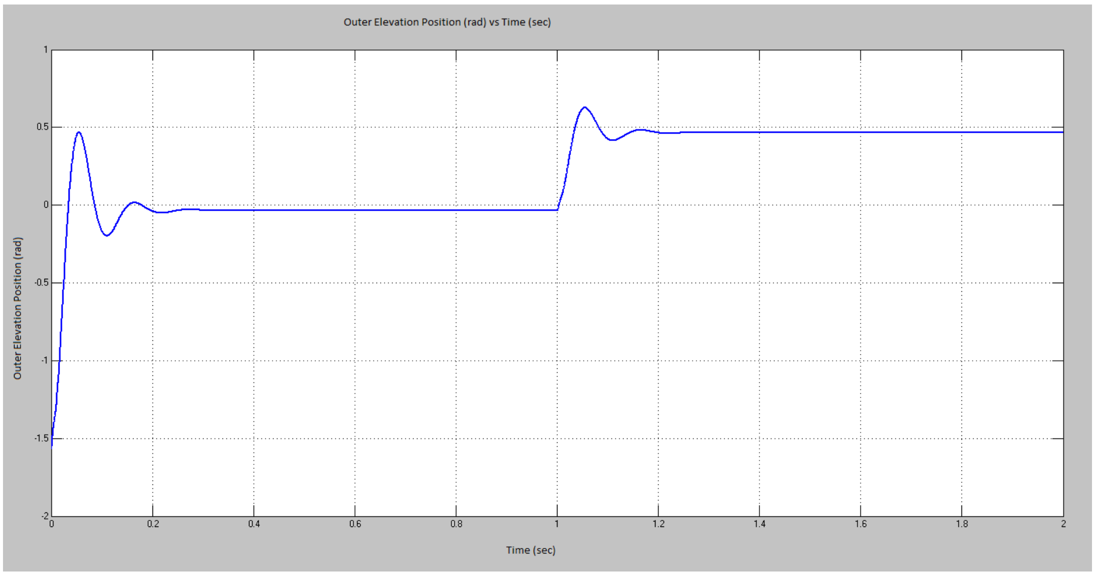

Figure 5.20: Outer Elevation Position Step Response with SMC

The step response of the outer elevation axis to the SMC, which can be seen from Figure 5.20, has a maximum overshoot of 30% and settling time about 0.2 sec. The response has an offset error of 4%.

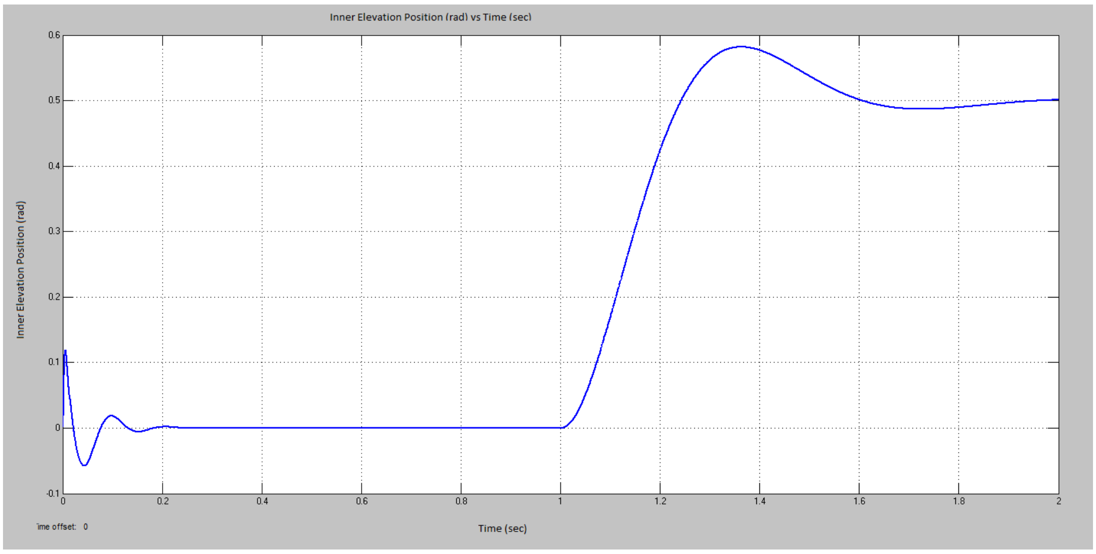

Figure 5.21: Inner Elevation Position Step Response with SMC

The step response of the inner elevation axis to the SMC, which can be seen from Figure 5.21, has a maximum overshoot of 16% and settling time about 0.2 sec. The response has no offset error. There exists a glitch in the response which results from the resonance of the plant.

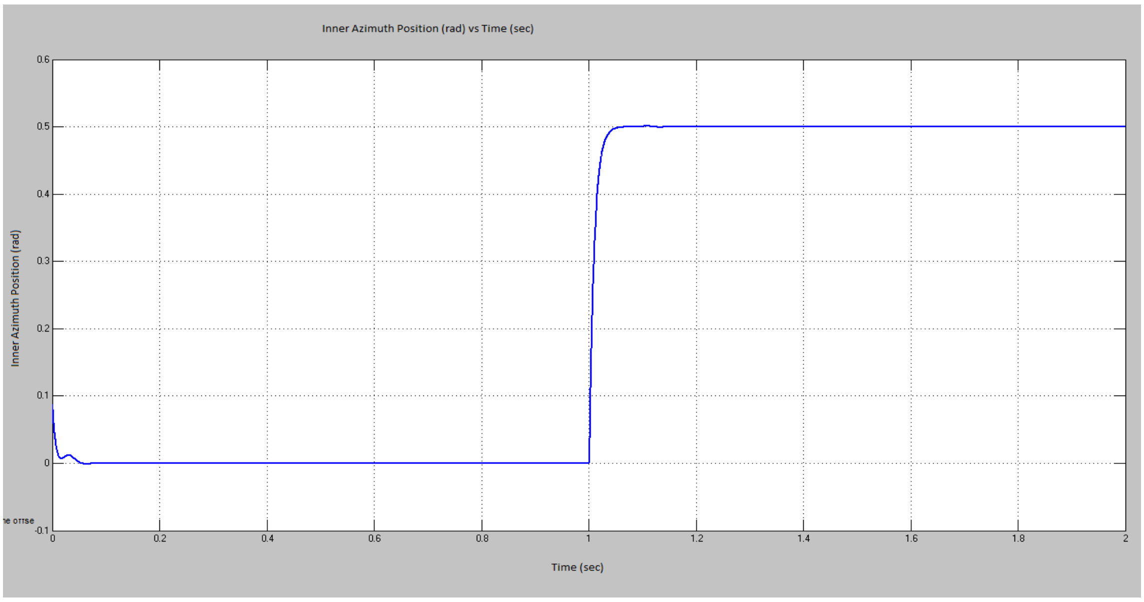

Figure 5.22: Inner Azimuth Position Step Response with SMC

The step response of the inner azimuth axis to the SMC, which can be seen from Figure 5.22, has a maximum overshoot of 0% and settling time about 0.03 sec. The response has no offset error.

Table 5.4: Comparison of the Step Responses

	PID Controller			Sliding Mode Controller			Automatically Tuned PID Controller		
	Settling Time (sec)	Over-shoot	Offset Error	Settling Time (sec)	Over-shoot	Offset Error	Settling Time (sec)	Over-shoot	Offset Error
Outer Azimuth	0.8	9%	Yes	0.1	5%	No	0.038	0%	No
Outer Elevation	0.32	6%	Yes	0.25	26%	Yes	0.038	0%	No
Inner Elevation	0.4	5%	Yes	0.7	16%	No	0.034	1.6%	No
Inner Azimuth	0.2	2%	Yes	0.03	0%	No	0.039	0%	No

Looking at the results given in Table 5.4, although the sliding mode controller is a robust control methodology, automatically tuned PID controller gives the best responses in terms of overshoot, settling time and offset error criteria. If the sliding mode controller is tuned better, it may give better responses. In the next section, stabilization performances of these controllers are compared and evaluated.

5.4 The Impact of Controller Implementation on Stability

With the aim of doing a further analysis on controller implementation, phase margins and gain margins of each of the 4 gimbals are compared through Bode plot analysis. The frequency response of the closed-loop system gives a good insight to measure marginal stability in terms of gain margin and phase margin. Thanks to Bode analysis, one can observe to where the gain and bandwidth of a controller can be adjusted. Phase margin is a more important performance measure than gain margin, since the aim of the control systems is to eliminate the unnecessary phase lag [33]. Phase lag mostly comes from the sensor delay and friction. Gain and phase margin evaluation methods are explained in [34], [35].

5.5 Stabilization

Stabilizing the image-based target tracking system means that getting rid of the disturbances on the tracking motion. In other words, it means zeroing the position of the inner azimuth gimbal, on which the camera is placed, relative to the inertial frame. To achieve this, the frame transformations, explained in Chapter 2, are exploited. The performances of the control methods which are mentioned in Section 5.2 and 5.3 will be compared according to stabilization performances. The position commands for the controllers of the 4 axes are generated through a code which calculates the angular positions of the gimbals relative to gimbal reference frames that make the inner azimuth (camera) position zero relative to the inertial frame, which is the world.

5.5.1 Disturbance Coming from Stewart Platform

In order to test the stabilization, first we need to generate a disturbance simulation. This task is carried out by the 6-DOF Stewart platform, which gives the base motion to the 4-DOF platform with the aim of simulating the vibrations coming from the vehicle on which the gimbal platform is placed.

The Stewart top plate position with respect to inertial frame in x, y and z axes (i.e., roll, pitch and yaw respectively) is shown in Figure 5.23, Figure 5.24, Figure 5.25, Figure 5.26 and Figure 5.27. The blue lines are the roll (x-axis) disturbances, the red ones are the pitch (y-axis) disturbances and the green ones are the yaw (z-axis) disturbances.

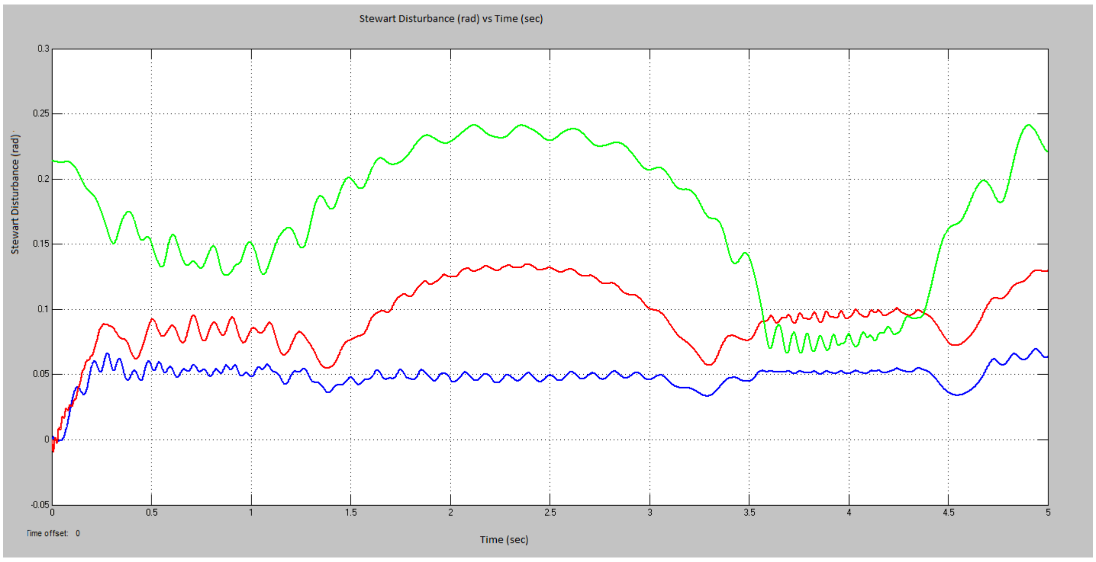

Figure 5.23: Stewart Platform Disturbance 1 (0.5 rad/sec Translational and 2 rad/sec Rotational DOF)

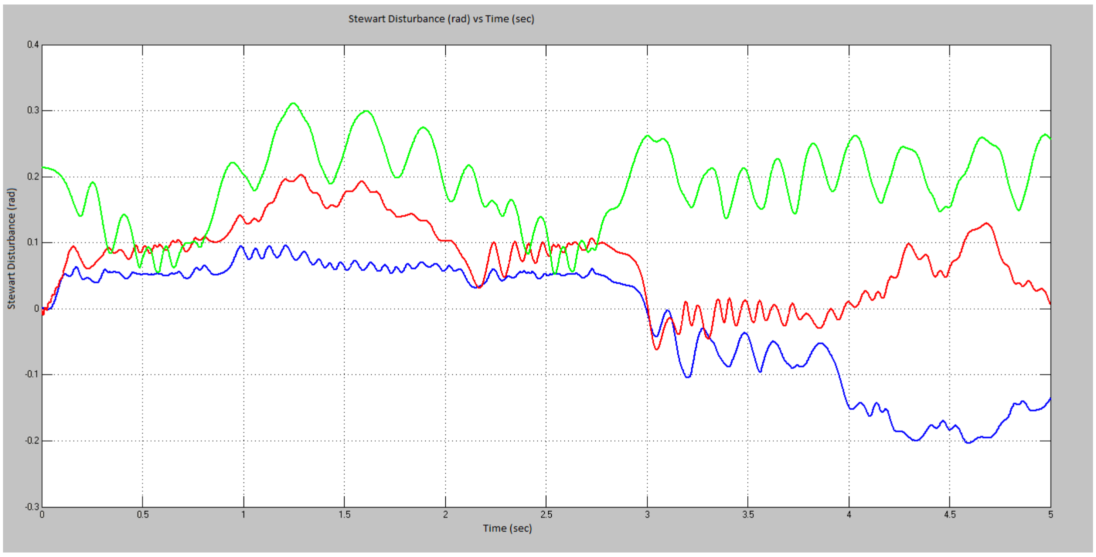

Figure 5.24: Stewart Platform Disturbance 2 (0.5 Hz Translational and 0.5 Hz Rotational DOF)

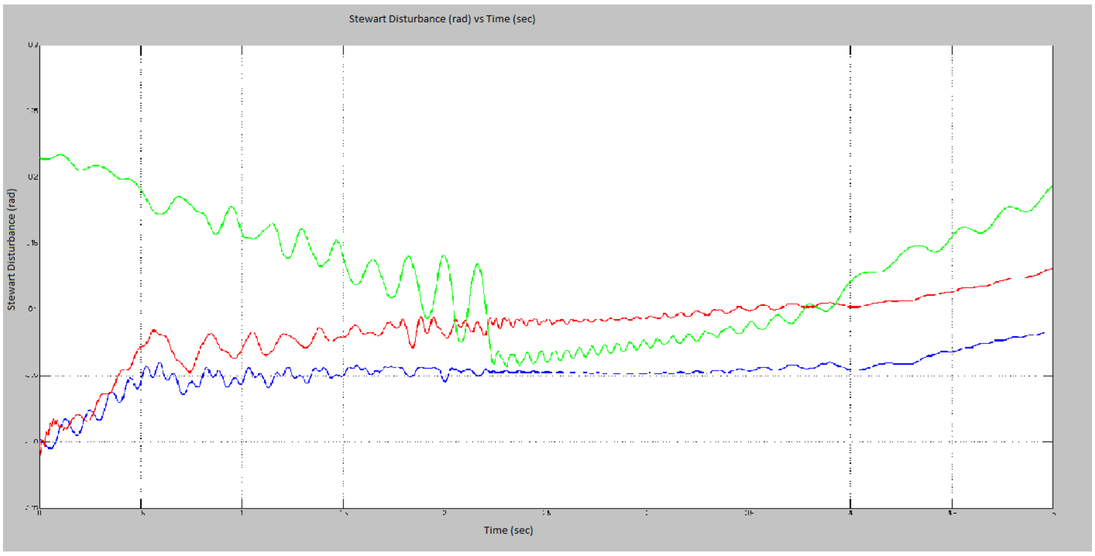

Figure 5.25: Stewart Platform Disturbance 3 (0.2 Hz Translational and 0.2 Hz Rotational DOF)

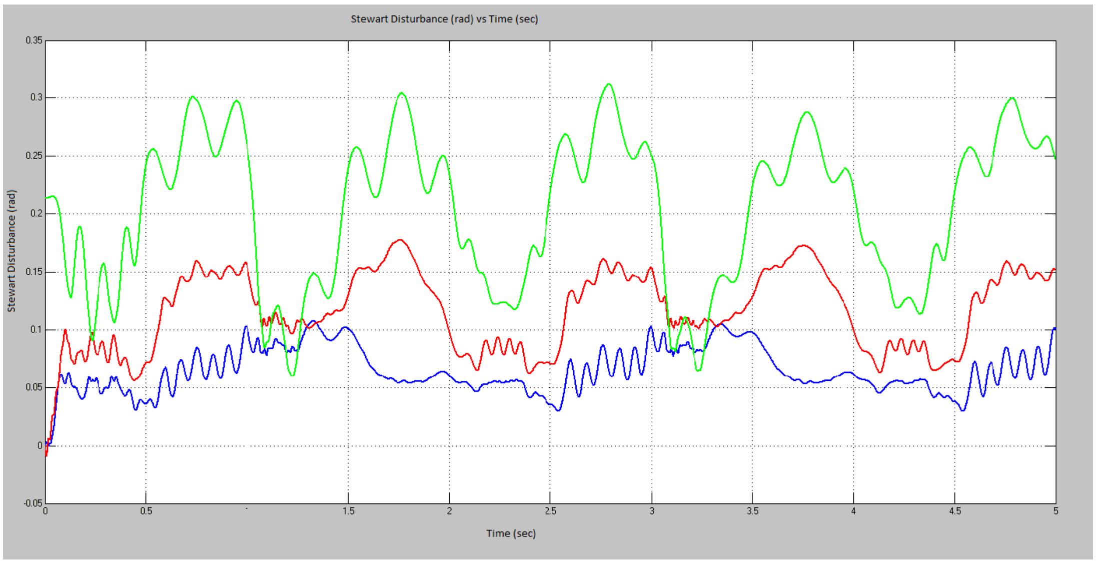

Figure 5.26: Stewart Platform Disturbance 4 (0.5 Hz Translational and 1 Hz Rotational DOF)

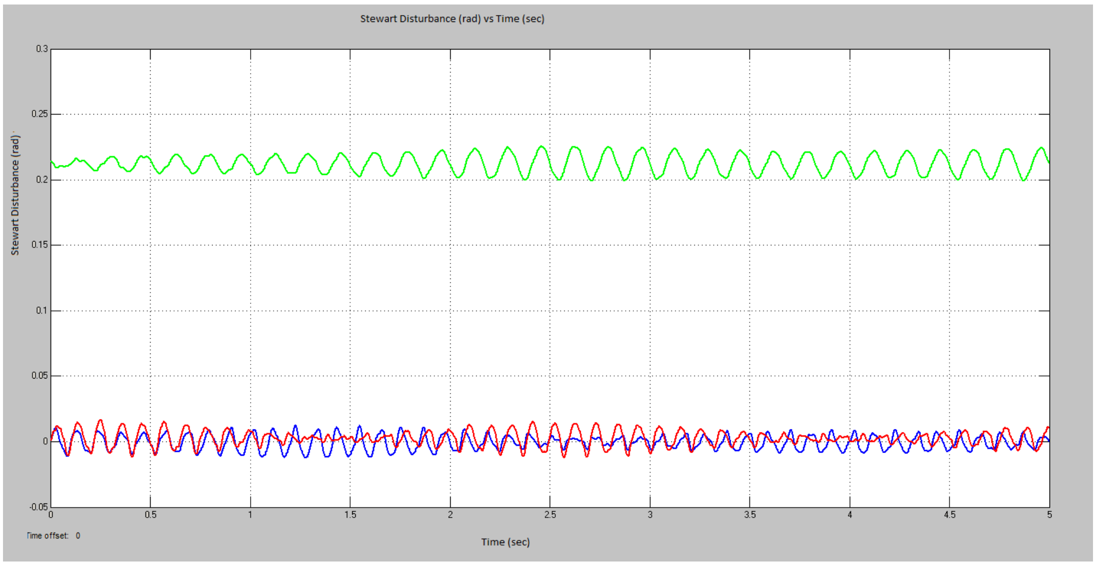

Figure 5.27: Stewart Platform Disturbance 5 (25 Hz Rotational DOF)

5.5.2 Stabilization Using the Manually Tuned PID Controller

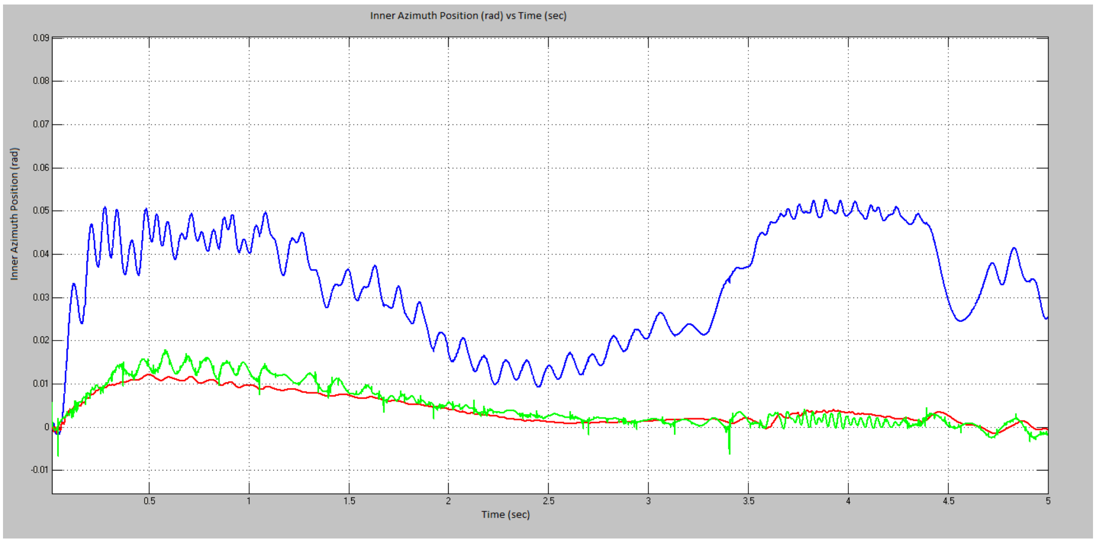

Figure 5.28: Stabilization with PID on Disturbance 1

Integral error of a 5-second stabilization error data is obtained by integrating the inner azimuth angular position signal with respect to the world frame. The integral error of the elevation axis is 5.4 mrad and the integral error of the azimuth axis is 4.4 mrad. The peak-to peak value of the elevation axis deviation of the position from zero is 0.03 and the peak-to peak value of the azimuth axis deviation of the position from zero is 0.024.

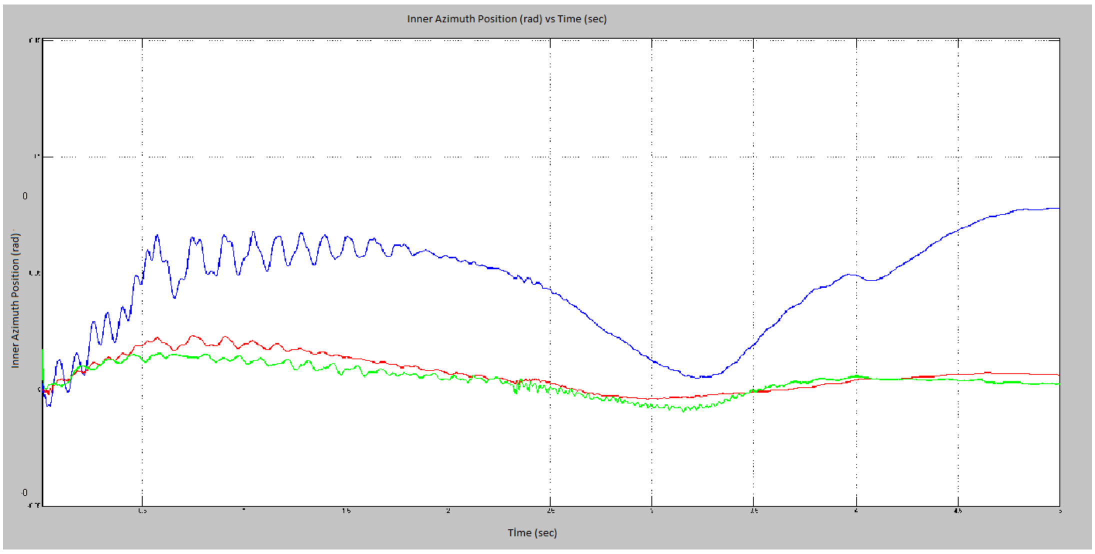

Figure 5.29: Stabilization with PID on Disturbance 2

Integral error of a 5-second stabilization error data is obtained by integrating the inner azimuth angular position signal with respect to the world frame. The integral error of the elevation axis is 0.9 mrad and the integral error of the azimuth axis is 1.2 mrad. The peak-to peak value of the elevation axis deviation of the position from zero is 0.027 and the peak-to peak value of the azimuth axis deviation of the position from zero is 0.016.

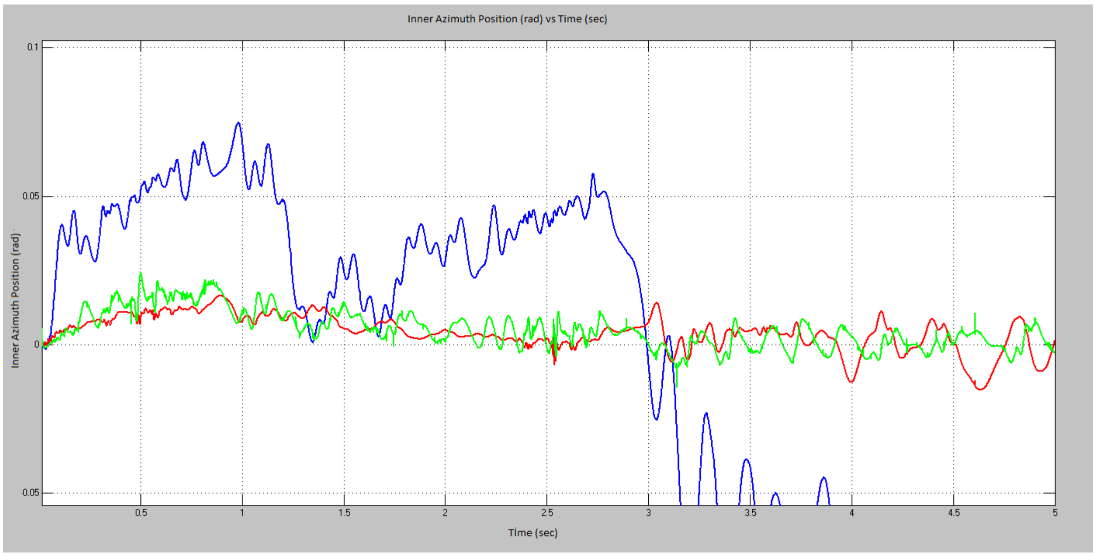

Figure 5.30: Stabilization with PID on Disturbance 3

Integral error of a 5-second stabilization error data is obtained by integrating the inner azimuth angular position signal with respect to the world frame. The integral error of the elevation axis is 82.8 mrad and the integral error of the azimuth axis is 22.9 mrad. The peak-to peak value of the elevation axis deviation of the position from zero is 0.03 and the peak-to peak value of the azimuth axis deviation of the position from zero is 0.024.

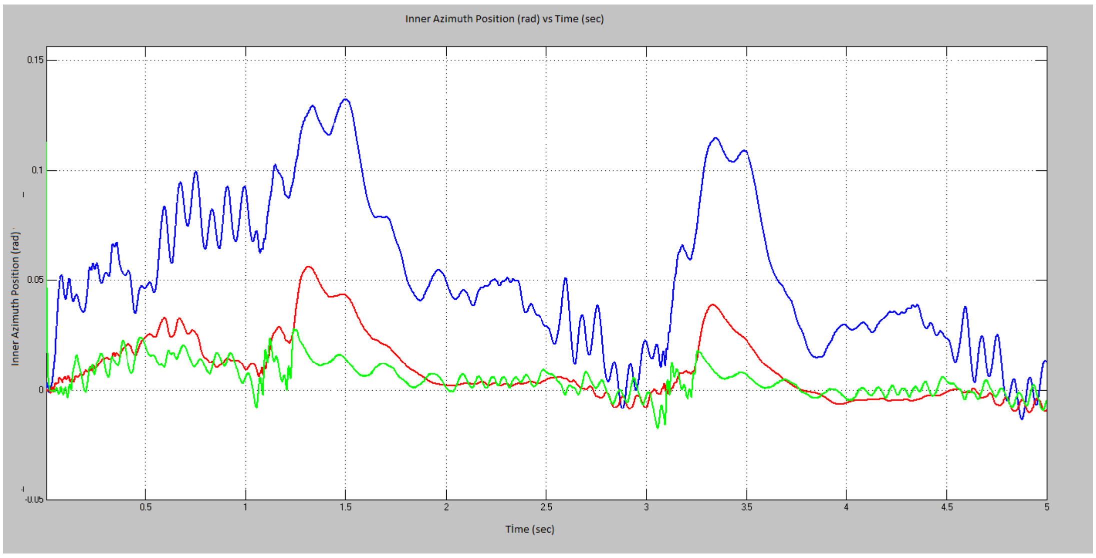

Figure 5.31: Stabilization with PID on Disturbance 4

Integral error of a 5-second stabilization error data is obtained by integrating the inner azimuth angular position signal with respect to the world frame. The integral error of the elevation axis is 114 mrad and the integral error of the azimuth axis is 73 mrad. The peak-to peak value of the elevation axis deviation of the position from zero is 0.07 and the peak-to peak value of the azimuth axis deviation of the position from zero is 0.05.

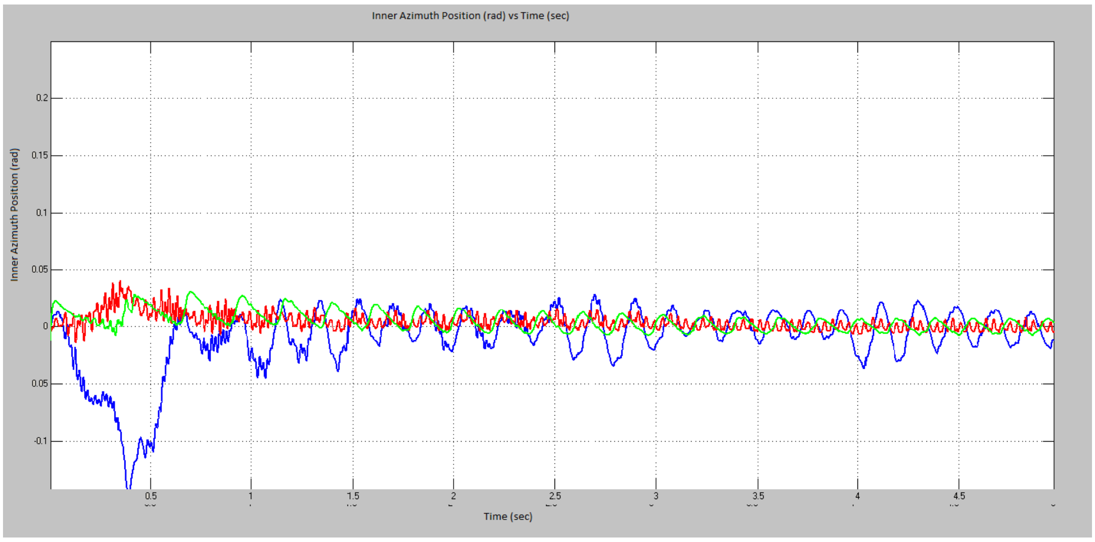

Figure 5.32: Stabilization with PID on Disturbance 5

Integral error of a 5-second stabilization error data is obtained by integrating the inner azimuth angular position signal with respect to the world frame. The integral error of the elevation axis is 2.5 mrad and the integral error of the azimuth axis is 1.8 mrad. The peak-to peak value of the elevation axis deviation of the position from zero is 0.05 and the peak-to peak value of the azimuth axis deviation of the position from zero is 0.03.

5.5.3 Stabilization Using the Automatically Tuned PID Controller

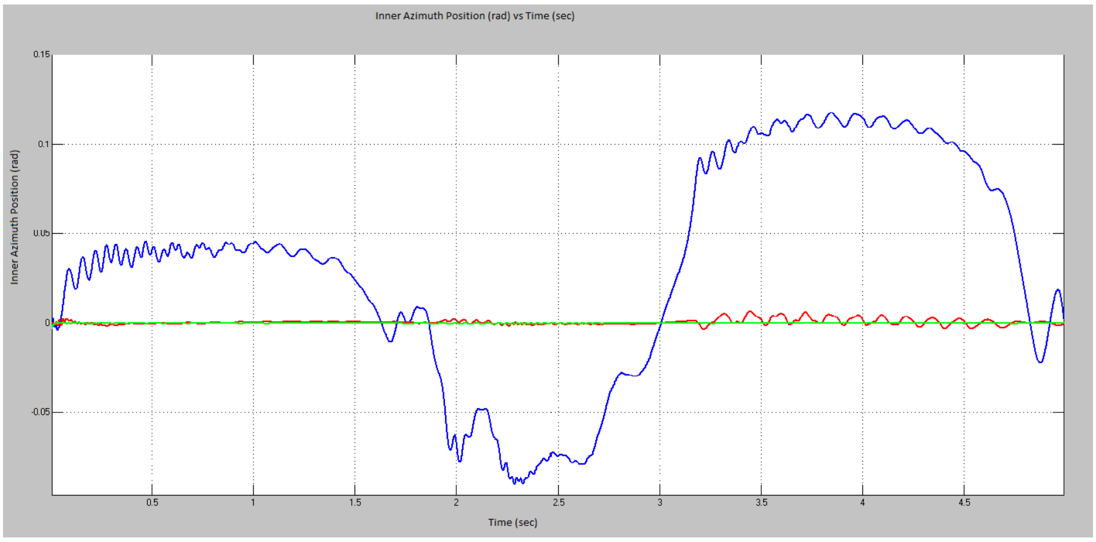

Figure 5.33: Stabilization with Automatically Tuned PID on Disturbance 1

Integral error of a 5-second stabilization error data is obtained by integrating the inner azimuth angular position signal with respect to the world frame. The integral error of the elevation axis is 0.59 mrad and the integral error of the azimuth axis is 0.093 mrad. The peak-to peak value of the elevation axis deviation of the position from zero is 0.007 and the peak-to peak value of the azimuth axis deviation of the position from zero is 0.0003 rad.

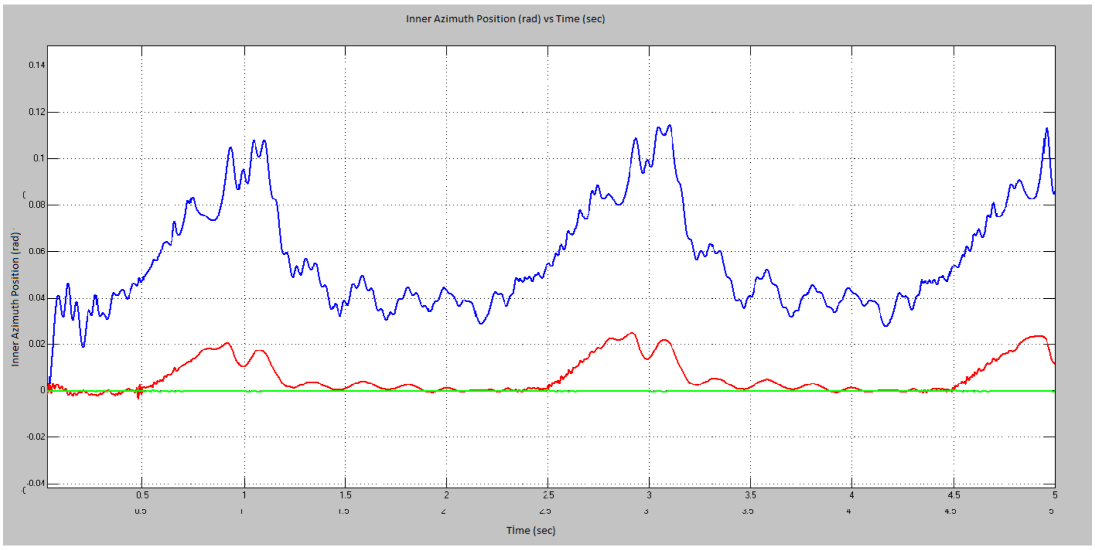

Figure 5.34: Stabilization with Automatically Tuned PID on Disturbance 2

Integral error of a 5-second stabilization error data is obtained by integrating the inner azimuth angular position signal with respect to the world frame. The integral error of the elevation axis is 20 mrad and the integral error of the azimuth axis is 0.137 mrad. The peak-to peak value of the elevation axis deviation of the position from zero is 0.023 and the peak-to peak value of the azimuth axis deviation of the position from zero is 0.0002 rad.

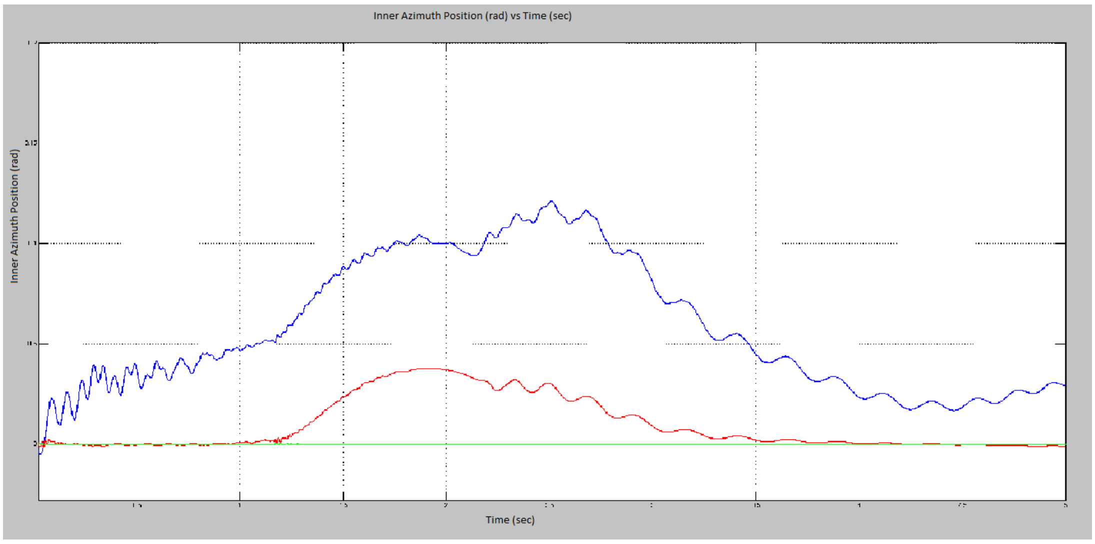

Figure 5.35: Stabilization with Automatically Tuned PID on Disturbance 3

Integral error of a 5-second stabilization error data is obtained by integrating the inner azimuth angular position signal with respect to the world frame. The integral error of the elevation axis is 1.2 mrad and the integral error of the azimuth axis is 0.109 mrad. The peak-to peak value of the elevation axis deviation of the position from zero is 0.038 and the peak-to peak value of the azimuth axis deviation of the position from zero is 0.0002 rad.

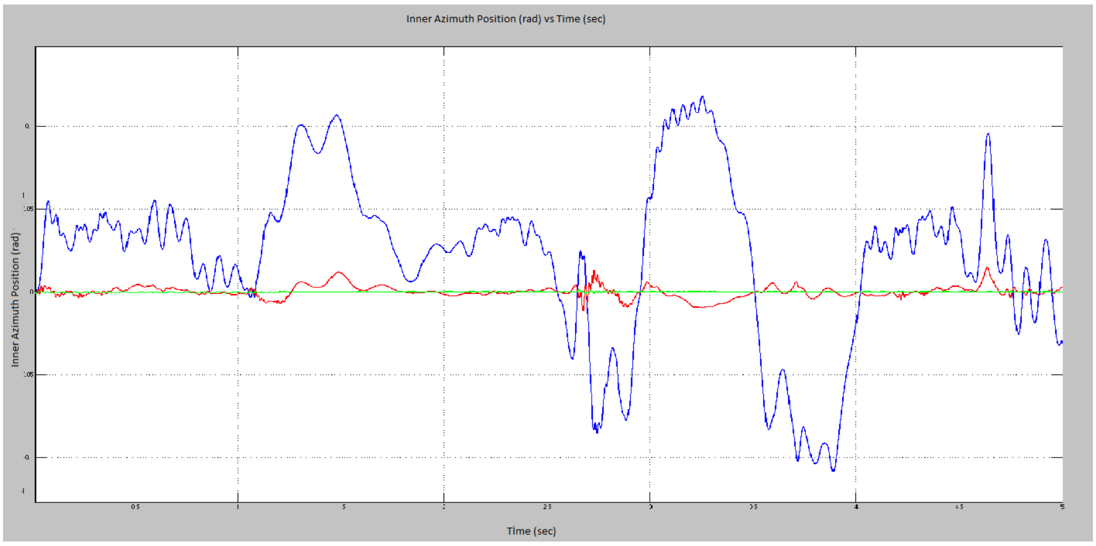

Figure 5.36: Stabilization with Automatically Tuned PID on Disturbance 4

Integral error of a 5-second stabilization error data is obtained by integrating the inner azimuth angular position signal with respect to the world frame. The integral error of the elevation axis is 0.53 mrad and the integral error of the azimuth axis is 0.106 mrad. The peak-to peak value of the elevation axis deviation of the position from zero is 0.025 and the peak-to peak value of the azimuth axis deviation of the position from zero is 0.001 rad.

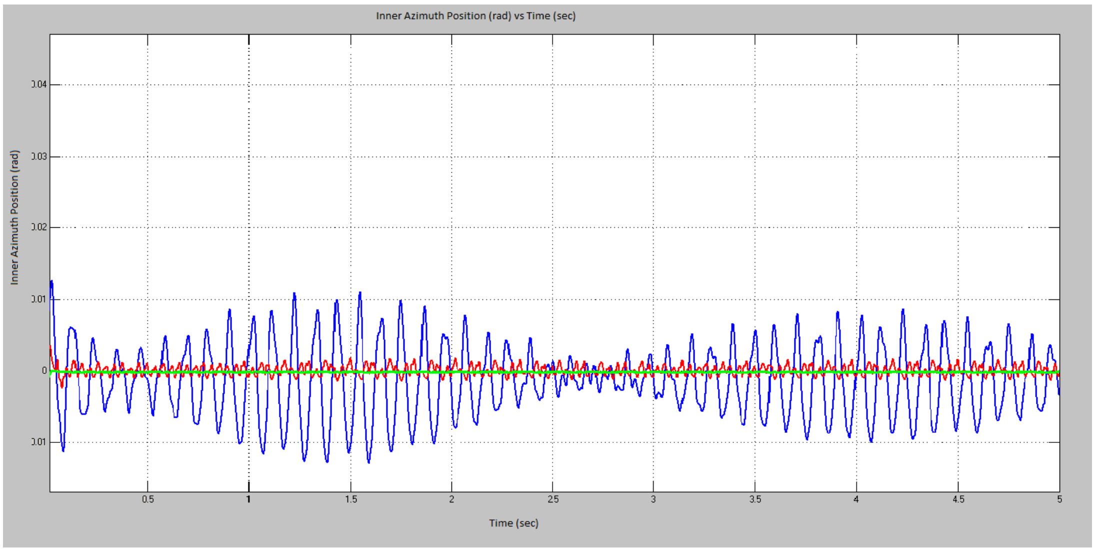

Figure 5.37: Stabilization with Automatically Tuned PID on Disturbance 5

Integral error of a 5-second stabilization error data is obtained by integrating the inner azimuth angular position signal with respect to the world frame. The integral error of the elevation axis is 0.028 mrad and the integral error of the azimuth axis is 0.113 mrad. The peak-to peak value of the elevation axis deviation of the position from zero is 0.002 and the peak-to peak value of the azimuth axis deviation of the position from zero is 0.0002 rad.

5.5.4 Stabilization Using the Sliding Mode Controller

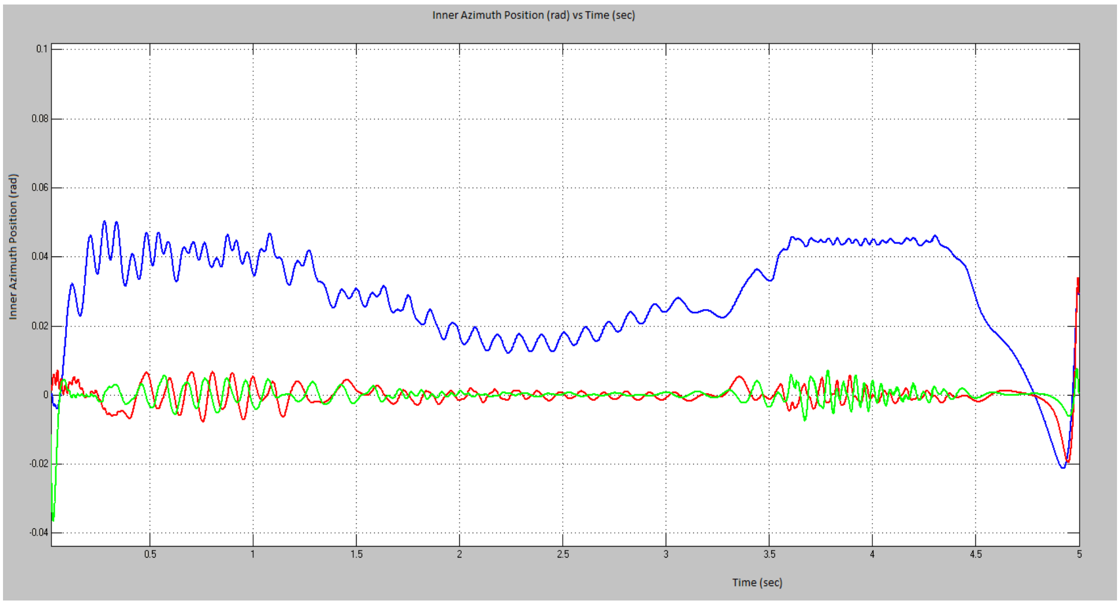

Figure 5.38: Stabilization with SMC on Disturbance 1

Integral error of a 5-second stabilization error data is obtained by integrating the inner azimuth angular position signal with respect to the world frame. The integral error of the elevation axis is 63.5 mrad and the integral error of the azimuth axis is 2.5 mrad. The peak-to peak value of the elevation axis deviation of the position from zero is 0.02 and the peak-to peak value of the azimuth axis deviation of the position from zero is 0.032.

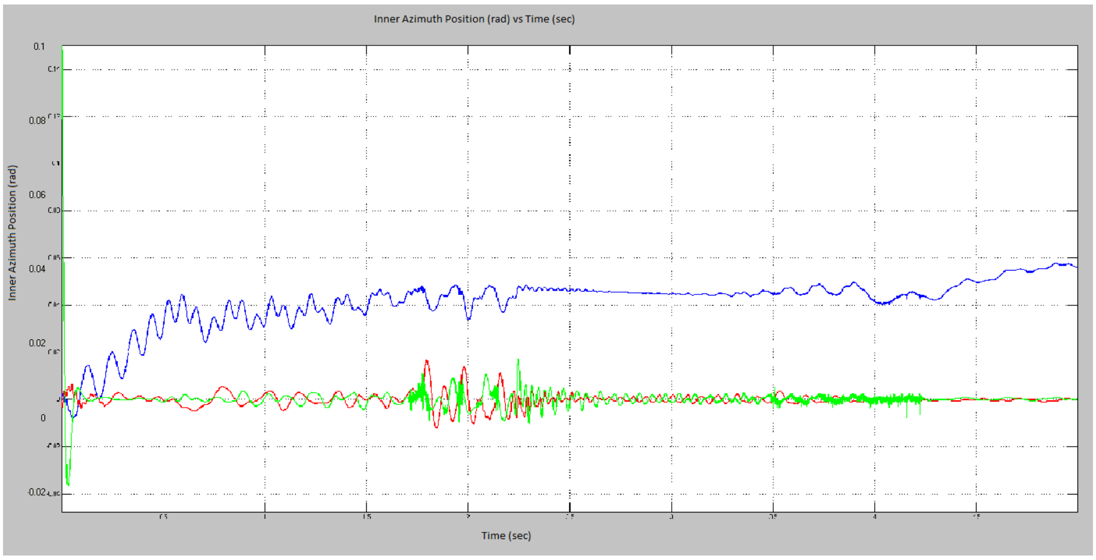

Figure 5.39: Stabilization with SMC on Disturbance 2

Integral error of a 5-second stabilization error data is obtained by integrating the inner azimuth angular position signal with respect to the world frame. The integral error of the elevation axis is 0.38 mrad and the integral error of the azimuth axis is 0.32 mrad. The peak-to-peak value of the elevation axis deviation of the position from zero is 0.017 and the peak-to peak value of the azimuth axis deviation of the position from zero is 0.015.

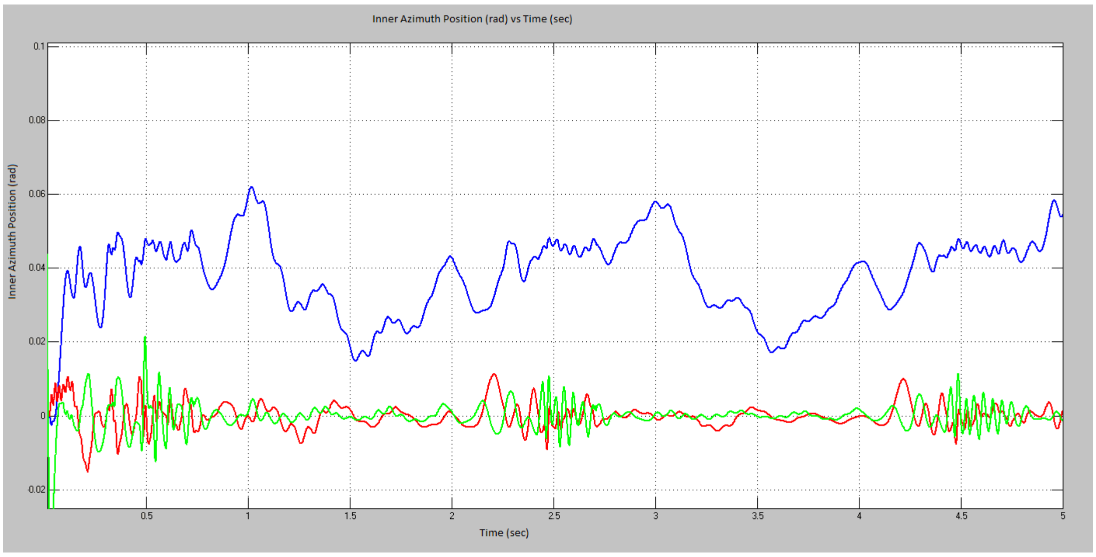

Figure 5.40: Stabilization with SMC on Disturbance 3

Integral error of a 5-second stabilization error data is obtained by integrating the inner azimuth angular position signal with respect to the world frame. The integral error of the elevation axis is 20 mrad and the integral error of the azimuth axis is 18 mrad. The peak-to peak value of the elevation axis deviation of the position from zero is 0.02 and the peak-to peak value of the azimuth axis deviation of the position from zero is 0.032.

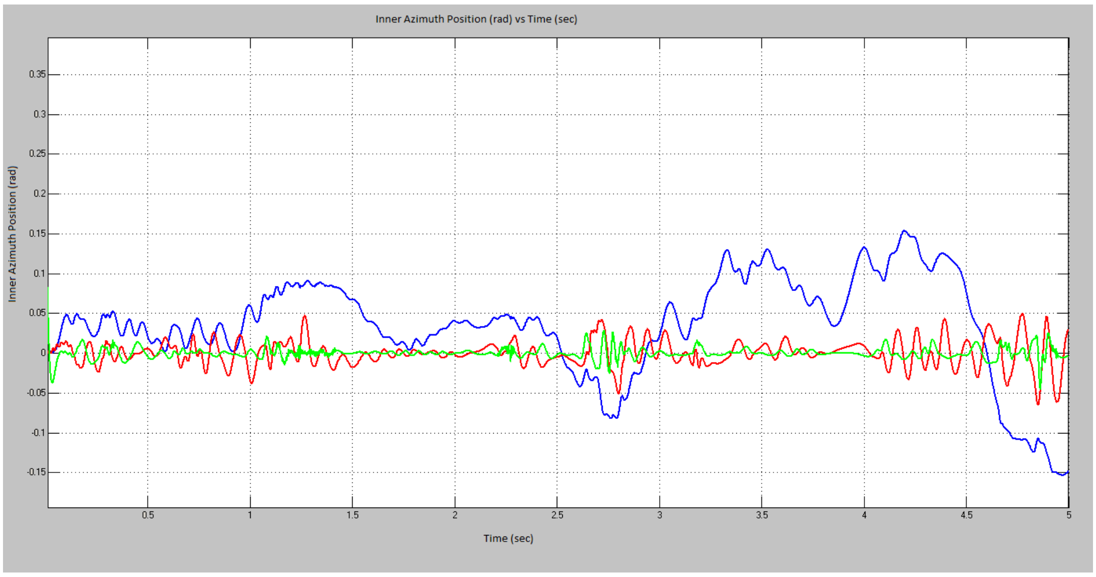

Figure 5.41: Stabilization with SMC on Disturbance 4

Integral error of a 5-second stabilization error data is obtained by integrating the inner azimuth angular position signal with respect to the world frame. The integral error of the elevation axis is 21 mrad and the integral error of the azimuth axis is 9.3 mrad. The peak-to peak value of the elevation axis deviation of the position from zero is 0.04 and the peak-to peak value of the azimuth axis deviation of the position from zero is 0.03.

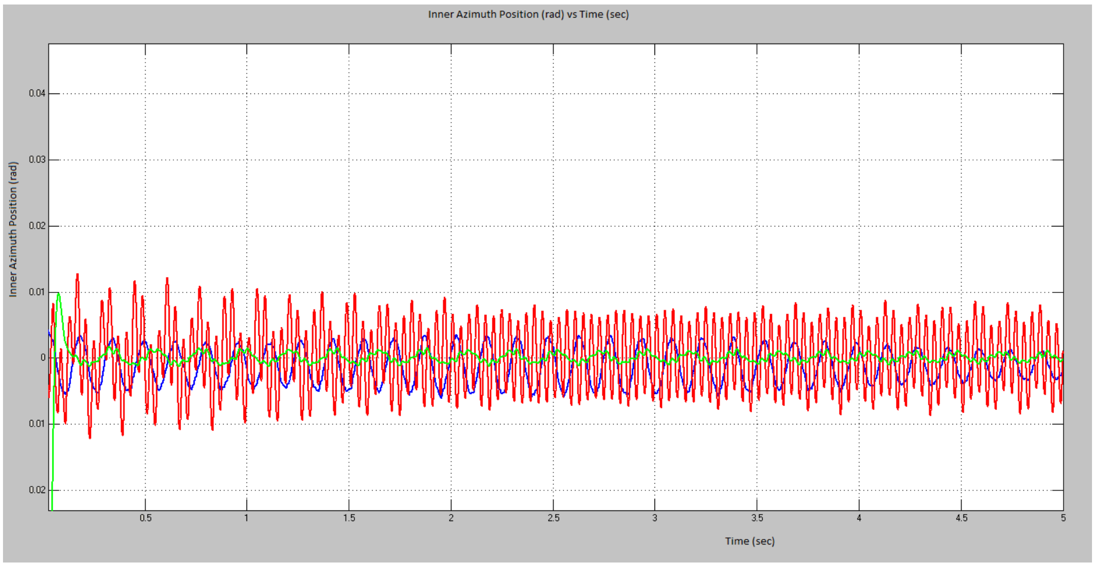

Figure 5.42: Stabilization with SMC on Disturbance 5

Integral error of a 5-second stabilization error data is obtained by integrating the inner azimuth angular position signal with respect to the world frame. The integral error of the elevation axis is 0.61 mrad and the integral error of the azimuth axis is 83 mrad. The peak-to peak value of the elevation axis deviation of the position from zero is 0.03 and the peak-to peak value of the azimuth axis deviation of the position from zero is 0.02.

5.5.5 Comparison and Evaluation of the Results

The inner azimuth (target tracking camera) position with respect to the inertial frame plots are given in Section 5.5.2 and Section 5.5.3. The 4-DOF gimbal is commanded to look at the zero position. Examining the peak-to-peak values of the elevation and azimuth axes under different disturbance frequencies, which is shown in Table 5.5, and the integral errors of the position errors in the azimuth and elevation axes, which is in the Table 5.6, can give a good performance comparison between the sliding mode controller and the PID controller.

Table 5.5: Peak-to-Peak Error Amplitudes for Disturbances at Different Frequencies

Disturbance Frequency	Stewart Disturbance Amplitude (rad)		PID Control Amplitude (rad)		Sliding Mode Control Amplitude (rad)		Automatically Tuned PID Control Amplitude (rad)	
	Pitch	Yaw	Pitch	Yaw	Pitch	Yaw	Pitch	Yaw
2 rad/sec	0.14	0.18	0.013	0.018	0.0025	0.0023	0.007	0.0003
0.2 Hz	0.14	0.16	0.027	0.016	0.017	0.015	0.038	0.0002
0.5 Hz	0.27	0.27	0.03	0.024	0.02	0.032	0.023	0.0002
1 Hz	0.17	0.25	0.07	0.05	0.04	0.03	0.025	0.001
25 Hz	0.08	0.0225	0.05	0.03	0.02	0.022	0.002	0.0002

Table 5.6: Integral Errors for Disturbances at Different Frequencies

Disturbance Frequency	PID Control Integral Error (mrad)		Sliding Mode Integral Error (mrad)		Automatically Tuned PID Control Integral Error (mrad)	
	Pitch	Yaw	Pitch	Yaw	Pitch	Yaw
2 rad/sec	5.4	4.4	63.5	2.5	0.59	0.093
0.2 Hz	0.9	1.2	0.38	0.32	1.2	0.109
0.5 Hz	82.8	22.9	20	18	20	0.137
1 Hz	114	73	21	9.3	0.53	0.106
25 Hz	2.5	1.8	0.61	83	0.028	0.113

Generally speaking, the peak-to-peak values in the Table 5.5 have shown a slight difference in manually tuned PID and SMC. However, the automatically tuned PID controller has shown much smaller errors. Furthermore, by investigating the figures in Section 5.5.2 and 5.5.3 it can be observed that the sliding mode controller has a faster response and a better performance in eliminating the disturbances than the manually tuned PID controller. However, the automatically tuned PID controller has given the fastest response with greatest accuracy. The manually tuned PID controller has an offset error in stabilization. Moreover, by investigating the integral error values in Table 5.6, it can be observed that there is a great difference between the automatically tuned PID controller and sliding mode controller and PID controller. As the disturbance frequency increases, the integral error of the PID controller becomes larger, the sliding mode controller's integral error has a slower increase, whereas the integral error of the automatically tuned PID controller stays almost the same. A better-tuned SMC may have a great stabilization performance. It has been left as a future work.

CHAPTER 6

CONCLUSION AND FUTURE WORK

In Chapter 1, the objective of this thesis work is stated as carrying out the LOS stabilization of the target tracking system which is on the 4-DOF platform. Doing this requires handling the two control problems, namely the regulator problem and the servo problem. The main focus is the regulator problem, which is the task of stabilization. Several disturbance rejection algorithms are aimed to minimize the effects of disturbances, such as friction, the unbalanced mass center resulted from inhomogeneity of mass, external torques and forces. An accurate stabilization requires to approach with an accurate model. To achieve this, mathematical model of the physical system is required. Newton-Euler approach is utilized so as to obtain the mathematical model of the system as close to physical one as possible. Transformations between coordinate frames are used in these equations, especially in Euler equations due to the fact that the forces act on the center of rotations of each gimbal. These transformations are useful in the later sections, which are about explaining the subjects of simulation modeling and the stabilization. The friction is needed to be modeled since it is the main disturbance to the platform. Karnopp friction model is selected since it contains a hysteresis loop preventing the numerical difficulties around the zero-velocity region. The correction of the sensor data is important since an accurate stabilization depends on it. The sensor which is used to measure the velocity information is a fiber-optic gyroscope. The correction of the data coming from the gyroscope is executed by a Kalman filter, which is an algorithm filtering out the noise in the measurement and estimates the future states with the aid of sensor fusion with an encoder.

The parameters of the simulation model of the 4-DOF platform and the gyroscope must be accurate. To achieve this, the real system's data must be collected and the outputs of the real system and the system model must be compared. Parameters must be selected such that the two output data are as close as possible. This is a system identification process which requires a minimization of the model output error by comparing it with the real system data. Also, the real system data comes from the gyroscope, which also has errors. Therefore it needs to be identified also. The ARMAX model is exploited to achieve this task. All these processes result in an accurate simulation model in MATLAB SimMechanics/Simulink environment. In Chapter 3, the system identification procedures for the 4-DOF platform and the gyroscope are carried out in order to have an accurate model of the system. Now, the model has become ready to be controlled and stabilized. Different control procedures such as PID control and sliding mode control are tested on the simulation model. The algorithms generated in this thesis will be implemented on the real system as a future work.

The stabilization process requires a great theoretical background including mathematical modeling for physical systems, system identification procedures chosen appropriately for each part of the system, the dynamics of the 6-DOF base motion platform which is about simulating the base disturbances physically, and the selection of the appropriate control method for stabilization. The frame transformation concepts, which are developed in the Chapter 2 is used for determining the stabilization set point. In other words, stabilization process is carried out with respect to the world frame. The bandwidth of the position and rate loops are determined by the component in the loop with the slowest bandwidth. The accuracy of the stabilization directly affects the quality of the high resolution image which centralizes the target to be tracked. Stabilization performances are compared in terms of step responses of the gimbal axes (overshoot and settling time are the performance criteria), the frequency responses of the closed loop systems which give the marginal stability and bandwidth evaluation, the peak-to-peak position error and the integral position error of the camera with respect to the world frame.

Different disturbance frequencies are tested with the aim of comparing the performances of the controllers. A classical control method, PID controller has achieved the stabilization task. Manually tuned and automatically tuned (by MATLAB PID tuner) PID controllers are implemented. Moreover, a robust control method, sliding mode controller has shown a great performance while achieving this task. The 2 control methods are compared and evaluated. When tuned correctly, both controller methods achieve this task with minimal error.

In conclusion, a high performance stabilization depends on a realistic system model and considering the system dynamics in detail. 4-DOF stabilization rejects the disturbances more than 2-DOF since while inner axes are tracking the target, outer gimbal axes filters out the main disturbances. Solving a control problem requires a strong theoretical background on physical concepts and control theory. Realization of the theoretical background via implementation on a system is an engineering challenge. Since the CATS system which is developed and manufactured by ASELSAN has not been completed yet, the implementation of the stabilization algorithms is left as a future work. Also different control methods, such as LQR will be tested after this study.

REFERENCES

[1] I.E. Şener, and K. Leblebicioğlu, "Görüntü Tabanlı Hedef Takip Sisteminin Gimbal Yapısının Modellenmesi", 17th National Conference of Turkish National Committee of Automatic Control (TOK), September 2015.

[2] J.M. Hilkert, "Stabilization, Pointing and Tracking System Technology Handbook", Texas Instruments Incorporated, May 1991.

[3] T. Öztürk, "Angular Acceleration Assisted Stabilization of a 2-DOF Gimbal Platform", M.Sc. Thesis, METU, September 2010.

[4] http://www.defenceturk.com/, last accessed on 25.12.2015.

[5] J.M. Hilkert, "Inertially Stabilized Platform Technology: Concepts and Principles", IEEE Control Systems Magazine, vol 28, pp. 26-45, February 2008.

[6] R.T. Rudin, "Strapdown Stabilization for Imaging Seekers", AIAA SDIO Interceptor Technology Conference, June 1993.

[7] D.R. Otlowski, K. Wiener, B.A. Rathbun "Mass Properties Factors in Achieving Stable Imagery from a Gimbal Mounted Camera", SPIE, vol. 6946, 2008.

[8] D.S. Bayard, "A Simple Analytic Method for Computing Instrument Pointing Jitter", Internal Document for California Institute of Technology, November 2000.

[9] R.J. Bauer "Kinematics and Dynamics of a Double-Gimbaled Control Moment Gyroscope", Mechanism and Machine Theory, vol. 37, pp. 1513-1529, February 2002.

[10] C. Batur, T. Sreeramreddy, Q. Khasawneh, “Sliding mode control of a simulated MEMS gyroscope”, American Control Conference, vol. 6, pp. 4160 – 4165, June 2005.

[11] J.L. Boiffier, “The Dynamics of Flight: The Equations” John Wiley&Sons, 1998.

[12] V. van Geffen, “A study of friction models and friction compensation”, Traineeship Report, Eindhoven Technical University Department Mechanical Engineering, Dynamics and Control Technology Group, December 2009.

[13] J. Deus, J. Asgari, D. Hravat and P. Kovac, “Modeling and Analysis of Automatic Transmission Engagement Dynamics-Linear Case”, J. Dyn. Sys. Meas. Control, vol. 128, part 2, pp. 263-277, May 2005.

[14] R.A. Romano ve C. Garcia, “Karnopp Friction Model Identification for a Real Control Valve”, The International Federation of Automatic Control, pp. 1, July 2008.

[15] G. Gök, “Dynamic Quantization for Track Fusion Under Communication Constraints”, M.Sc. Thesis, Metu, June 2015.

[16] V. Verdult, and M. Verhaegen, “Filtering and System Identification: A Least Squares Approach”, Cambridge University Press, 2007.

[17] L. Ljung, “System Identification, Theory for the User”, Prentice Hall, 1987.

[18] H.D. Gavcar, J.K., “Compensation Methods for Quasi-Static Acceleration Sensitivity of MEMS Gyroscopes”, M.Sc. Thesis, METU, November 2014.

[19] G. Özdoğan, “System Identification and Modeling of Gyro-Stabilized IR/EO Gimbal System in Frequency Domain”, M.Sc. Thesis, METU, July 2014.

[20] The MathWorks, Inc., “SimMechanics™ User’s Guide R2013a”, www.mathworks.com, 2013, last accessed on 25.12.2015.

[21] http://www.ilkaymeseli.com/2011/04/kinematik-analiz/, last accessed on 25.12.2015.

[22] İ.K. Erünsal, “System Identification and Control of a Sea Surface Vehicle”, M.Sc. Thesis, METU, September 2015.

[23] “Matlab 2011b Documentation, PIDtune” 2015, last accessed on 25.12.2015.

[24] “Discretizing a pid controller.” https://www.researchgate.net. Accessed: August 2015.

[25] M.S. Fadali, “Sliding Mode Control”, Lecture Notes at University of Nevada.

[26] E.W. McGookin, “Optimization of sliding mode controllers for marine applications: a study of methods and implementation issues”, Ph.D thesis, University of Glasgow, UK, September 1997

[27] http://scholarworks.rit.edu/cgi/viewcontent.cgi?article=8838&context=theses last accessed on 25.12.2015.

[28] H. Khalil, Nonlinear Systems, Prentice Hall, Upper Saddle River, NJ, 2003.

[29] E. Çandır, “A Proxy-Based Sliding Mode Control Enhanced with Disturbance Observer for the Stabilization and Control of a Gun-Turret Platform”, M.Sc. Thesis, METU, July 2014.

[30] E. Alfaro-Cid et al., “A Comparative Study of Genetic Operators for Controller Parameter Optimization,” Control Engineering Practice, vol 17, pp. 185-197, January 2009.

[31] E.W. McGookin, Optimization of sliding mode controllers for marine applications: a study of methods and implementation issues, Ph.D. thesis, University of Glasgow, UK, September 1997.

[32] J. Brian, J. William, “Sliding Mode Control in a Two Axis Gimbal System”, Aerospace Conference, vol. 5, pp. 457-470, March 1999.

[33] G. Ellis., “Observers in Control Systems: A Practical Guide,” Academic Press, 2002.

[34] K. Ogata, “Modern Control Engineering”, Fourth Edition, Prentice-Hall Inc., New Jersey, 2002.

[35] K. Ogata, “Discrete Time Control Systems”, Fourth Edition, Prentice-Hall Inc., New Jersey, 1987.

[36] J. Kaustky et al., “Robust Pole Assignment in Linear State Feedback,” International Journal of Control, vol 41, pp. 1129-1155, July 1985.

[37] V. Sangveraphunsiri and K. Malithong, “Control of Inertial Stabilization Systems Using Robust Inverse Dynamics Control and Sliding Mode Control”, The 23rd Conference of the Mechanical Engineering Network of Thailand, November 2009.

[38] S. Dharmveer, P. Kurode, B. Parkhi, B. Tamhane, “Robust Control for Seeker Scan Loop using Sliding Modes”, Control, Automation and Systems (ICCAS), October 2012.

[39] M. Abdo, A.R. Vali, A.R. Toloei, M.R. Arvan, “Stabilization Loop of a Two Axes Gimbal System Using Self-tuning PID Type Fuzzy Controller”, ISA Transactions, vol. 53, pp. 591-602, 2014.

[40] B. Altınöz, “Identification of Inertial Sensor Parameters”, M.Sc. Thesis, METU, September 2015.